0.13 μm SiGe BiCMOS W&D-Band Receivers for Passive Millimeter-Wave Imaging Applications

by

Berktug Ustundag

Submitted to the Graduate School of Engineering and Natural Sciences
in partial fulfillment of
the requirements for the degree of
Master of Science

Sabancı University

Summer, 2016

0.13 μm SiGe BiCMOS W&D-Band Receivers for
Passive Millimeter-Wave Imaging Applications

APPROVED BY

Prof. Dr. Yaşar GÜRBÜZ
(Thesis Supervisor) .....

Assoc. Prof. Dr. Meriç ÖZCAN .....

Asst. Prof. Erdinç ÖZTÜRK .....

DATE OF APPROVAL: 10.08.2016

© Berktug Ustundag 2016

All Rights Reserved

Acknowledgements

As my long journey at Sabanci University has come to an end, I would like to express my sincere gratitude and appreciation to all who made this work possible.

First of all, I am grateful to Prof. Yaşar Gürbüz for his exceptional support and motivation as an instructor and supervisor over the past three years. His confidence in me has greatly influenced me to become a worthy student and a researcher.

I also would like to thank Prof. Meriç Özcan and Prof. Erdinç Öztürk for taking their precious time to serve in my thesis committee and for their valuable comments and feedback. Also, my thanks to Dr. Mehmet Kaynak of IHP who helped us along the way immensely, with his guidance and support.

Former and present SU Microsystems group members, Dr. Hüseyin Kayahan, Melik Yazıcı, Ömer Ceylan, Emre Özeren, Can Çalışkan, İlker Kalyoncu, Murat Davulcu, Atia Shafique, Elif Gül Özkan, Arman Galioğlu, deserve a lot of credit for creating such a wonderful environment and I owe them a thank you for all the guidance they have provided as well as the friends they have become. I am grateful for all the support and the endless discussions with my friends, Umut Kodak and Umut Çelik. Without my fellow designer, Barbaros Çetindoğan who deserves a special thanks, this work would not be possible. I would also like to thank Sabanci staff, Ali Kasal and Mehmet Doğan for their assistance and experience and the IHP staff for helping with our measurements. In addition, thanks to Bilgesu and Başak for their friendship during my years in Sabancı.

Finally, and most importantly, I would like to thank my parents İncilay and Arif, and my sister İrem for all the love, support and understanding. They have been the major source of influence on the person I have become and I can not thank them enough for the sacrifices they made. I thank them for their patience and showing me how to achieve my goals and I am proud to be their son and brother.

0.13 μm SiGe BiCMOS W&D-Band Receivers for Passive Millimeter-Wave Imaging Applications

Berktug Ustundag
EE, Master's Thesis, 2016
Thesis Supervisor: Prof. Dr. Yaşar GÜRBÜZ

Keywords: W-Band Radiometer, D-Band Radiometer, mm-wave Integrated Circuits, Dicke Switching.

Abstract

Design of millimeter-wave (30-300 GHz) integrated circuits for various applications such as RADAR, wireless communication systems and imaging systems has become an active area of research in recent years. Passive type of imaging systems have the potential to impact several areas including security scanning, concealed weapon detection and topography imaging. Therefore, high performance MMICs capable of operating 100 GHz and beyond will be the key for next generation imaging systems. Process technologies such as CMOS and SiGe BiCMOS have advanced tremendously over the past decades. Especially the SiGe BiCMOS process with HBTs that have f_t/f_{max} values above several hundred GHz, is an excellent option for high performance mm-wave applications due to its comparable performance to III-V technologies while having relatively lower costs.

In this thesis, we present W-Band (75-110 GHz) and D-Band (110-170 GHz) radiometer sub-blocks as well as single and dual channel implementations with on-chip antennas using IHP's 0.13 μm SiGe BiCMOS technology. In order to keep the Noise Equivalent Temperature Difference (NETD) of the radiometers below 1 K, low insertion loss SPDT switches, high bandwidth low noise amplifiers (LNA) and high responsivity power detectors have been designed and measured. Dicke Switched and Total Power Radiometer front end receivers have been implemented. For complete integration, on-chip mm-wave antennas that make use of LBE (Local Backside Etching) process are included in the receivers. Also, a single antenna dual channel receiver is proposed and designed that would increase the sensitivity of the radiometer by $\sqrt{2}$ without increasing the overall die area.

Milimetre Dalga Pasif Görüntüleme Sistemleri için 0.13 μm SiGe BiCMOS W&D-Band Alıcılar

Berktug Ustundag
EE, Yüksek Lisans Tezi, 2016
Tez Danışmanı: Prof. Dr. Yaşar GÜRBÜZ

Anahtar Kelimeler: W-Band Radyometre, D-Band Radyometre, mm-dalga Entegre Devre, Dicke Anahtarlama.

Özet

Son yıllarda, otomotiv RADAR'ları, yüksek veri hızlı kablosuz iletişim ve görüntüleme sistemleri için geliştirilen milimetre dalga (30-300 GHz) tümleşik devre tasarımları aktif bir araştırma alanı haline gelmiştir. Pasif görüntüleme sistemlerinin potansiyel etkisi; güvenlik taramaları, silah algılama ve topografi görüntüleme gibi uygulamalar üzerinde görülebilmektedir. Bu sebeple, 100 GHz ve üstünde çalışabilen yüksek performanslı MMIC'ler (Monolitik Mikrodalga Entegre Devre) yeni nesil görüntüleme sistemleri için anahtar rol oynamaktadır. CMOS ve SiGe BiCMOS gibi proses teknolojileri son yıllarda büyük bir gelişme göstermiştir. Özellikle SiGe BiCMOS prosesi, bir kaç yüz GHz f_t/f_{max} değerine ulaşabilen HBT'leri ile III-IV teknolojilerine yakın performansı daha düşük maliyetler ile gösterebilmekte, dolayısı ile yüksek performanslı mm-dalga uygulamaları için mükemmel bir opsiyon sunmaktadır.

Bu tezde; IHP'nin 0.13 μm SiGe BiCMOS teknolojisi kullanılarak gerçeklenen W-Band (75-110 GHz) ve D-Band (110-170 GHz) radyometre alt blokları ile yonga üstü antenlerin dahil edildiği tek ve çift kanallı alıcılar sunulmuştur. Radyometrelerin ısı eşlenik gürültü seviyelerini (NETD) 1 K'nın altında tutmak için, belirtilen bantlarda; düşük giriş kayıplı SPDT anahtlarlar, düşük gürültülü güçlendiriciler (LNA) ve yüksek cevap verme yetili güç detektörleri tasarlanmış ve ölçülmüştür. Dicke Anahtarlamalı ve Toplam Güç Radyometre ön blok alıcıları gerçeklenmiştir. Tüm sistemin entegrasyonu için LBE (yerel pul arkası aşındırma) prosesini kullanan yonga üstü antenler de alıcılara dahil edilmiştir. Ayrıca, alanı arttırmadan radyometre hassasiyetini $\sqrt{2}$ kat arttırabilecek, tek anten çift kanal alıcı topolojisi önerilmiş ve tasarlanmıştır.

Contents

Acknowledgements iv

Abstract v

List of Figures xi

List of Tables xii

List of Abbreviations xiv

1 Introduction 1
- 1.1 Imaging Systems . . . 1
- 1.2 mm-wave Radiometers . . . 3
- 1.3 MMIC Radiometers . . . 5
- 1.4 SiGe BiCMOS Technology . . . 7
- 1.5 Motivation . . . 10
- 1.6 Organization . . . 12

2 Radiometer Fundamentals 13
- 2.1 Detection Principles . . . 13
- 2.2 Theoretical Sensitivity . . . 17
- 2.3 Radiometer Architectures . . . 21
  - 2.3.1 Total Power Radiometer . . . 21
  - 2.3.2 Dicke Radiometer . . . 23
  - 2.3.3 Other Architectures . . . 24
- 2.4 Radiometric Imaging . . . 26

3 W-Band Radiometer Design in SiGe BiCMOS 29
- 3.1 Sub-Block Designs . . . 29
  - 3.1.1 Power Detector . . . 29
  - 3.1.2 Low Noise Amplifier . . . 34
  - 3.1.3 SPDT Switch . . . 37
  - 3.1.4 Antenna . . . 42
- 3.2 Simulation and Measurement Results of the Sub-Blocks . . . 43
  - 3.2.1 Power Detector . . . 43
  - 3.2.2 Low Noise Amplifier . . . 47
  - 3.2.3 SPDT Switch . . . 50
  - 3.2.4 Antenna . . . 58
- 3.3 TPR and Dicke Radiometer System Implementations . . . 60
- 3.4 Dual Channel Radiometer System Implementation . . . 63
  - 3.4.1 System Description . . . 63
  - 3.4.2 Switch Design . . . 65
  - 3.4.3 Dual Receiver Front-end System . . . 68
- 3.5 Summary of Performance and Comparison of the Implemented Systems 69

4 D-Band Radiometer Design in SiGe BiCMOS **71**
4.1 Sub-Block Designs . . . 71
4.1.1 Power Detector . . . 71
4.1.2 Low Noise Amplifier . . . 73
4.1.3 SPDT Switch . . . 74
4.1.4 Antenna . . . 76
4.2 Simulation and Measurement Results of the Sub-Blocks . . . 77
4.2.1 Power Detector . . . 77
4.2.2 Low Noise Amplifier . . . 80
4.2.3 SPDT Switch . . . 84
4.2.4 Antenna . . . 89
4.3 Radiometer System Implementations . . . 91

5 Conclusion & Future Work **94**
5.1 Summary of Work . . . 94
5.2 Future Work . . . 97

A Appendix **100**

References **106**

List of Figures

1 Global sea surface temperature derived from Metop AVHRR observations [1] . . . 2
2 (a) WINDSAT polarimeter [2] and (b) AN/TPS-59 RADAR [3] . . . 2
3 Atmospheric attenuation levels at various RH (Relative Humidity) and foggy weather conditions [4] . . . 4
4 Blackbody radiation intensity at different wavelengths [5] . . . 5
5 (a) 118 GHz IMAS Radiometer [6], (b) Fully integrated W-Band SoC for imaging applications [7] . . . 6
6 f_t and f_{max} values for various SiGe HBT technologies [8] . . . 7
7 Cross section of the IHP 0.13 μm SiGe HBT process (SG13G2) . . . 9
8 Cross section of the LBE process in IHP 0.13 μm SiGe HBT technology 9
9 (a) System block diagram of the proposed W-Band and D-Band Dicke radiometers (b) System block diagram of the W-Band dual receiver Dicke radiometer . . . 10
10 Basic operating principle of a radiometer . . . 13
11 (a) Spectral brightness of a blackbody [9] , (b) Approximation of Plank's law by Rayleigh Jeans law [10] . . . 14
12 Illustration of the power incident of the receiving aperture A_r, emitted from the surface A_t [11] . . . 15
13 Block diagram of the Total Power Radiometer . . . 18
14 Detailed block diagram of the direct detection Total Power Radiometer 21
15 Detailed block diagram of the heterodyne Total Power Radiometer . . 22
16 Detailed block diagram of the Dicke Radiometer . . . 23
17 Illustration of the periodically calibrated radiometer with mechanical scanning . . . 25
18 Block diagram of the noise injection radiometer . . . 25
19 Block diagram of the correlation radiometer . . . 26
20 Concealed weapon detection using a 90 GHz radiometer [12] . . . 28
21 Illustration of an FPA with additional optics and the corresponding image mapping . . . 28
22 Block diagram of the TPR and Dicke radiometers . . . 29
23 The schematic of the W-Band Power Detector . . . 30
24 NEP and Responsivity vs. R_{load} . . . 32
25 NEP of the Power detector vs. V_{bias} for different number of HBTs . . 33
26 EM simulation setup of W-Band Power Detector in ADS Momentum 34
27 Calculated NETD vs. LNA gain for different NF values . . . 35
28 The schematic of the W-Band LNA . . . 35
29 MAG vs. S21 curves for different loads for a CE stage . . . 36
30 EM simulation setup for W-Band LNA in ADS Momentum . . . 36
31 The schematic of the W-Band SPDT Switch (First version) . . . 38
32 (a) Microstrip transmission line (b) Slow-wave Coplanar transmission line . . . 39
33 Simulated (a) IL and (b) isolation of the microstrip and slow-wave SPDTs . . . 40
34 The schematic of the W-Band SPDT Switch (Second version) . . . 40

35 EM simulation setup for W-Band SPDT in ADS Momentum (Second version) . . . 41
36 EM simulation setup for W-Band antenna in HFSS . . . 43
37 Micrograph of the W-Band Power Detector . . . 44
38 Simulated and measured S11 of the W-Band Power Detector . . . 45
39 Simulated V_{OUT} difference vs P_{IN} of the W-Band Power Detector at 94 GHz . . . 45
40 Simulated output noise power spectrum of the W-Band Power Detector 46
41 Simulated responsivity and NEP vs frequency of the W-Band Power Detector . . . 46
42 Micrograph of the W-Band LNA . . . 48
43 Simulated and measured input and output return loss of the W-Band LNA . . . 48
44 Simulated and measured gain of the W-Band LNA . . . 49
45 Simulated noise figure of the W-Band LNA . . . 49
46 Micrograph of the first version (a) microstrip and (b) slow-wave W-Band SPDT switch . . . 51
47 The simulation and measurement results of input and output return loss of the first version W-Band SPDT switch . . . 52
48 The simulation and measurement results of insertion loss of the first version W-Band SPDT switch . . . 53
49 The simulation and measurement results of isolation of the first version W-Band SPDT switch . . . 53
50 The measurement results of insertion loss of the first version microstrip W-Band SPDT switch at different bias voltages . . . 54
51 The measurement results of isolation of the first version microstrip W-Band SPDT switch at different bias voltages . . . 54
52 The micrograph of the second version W-Band SPDT switch . . . 55
53 The simulation results of the input and output return loss of the second version W-Band SPDT switch . . . 56
54 The simulation results of the isolation of the second version W-Band SPDT switch . . . 56
55 The simulation results of the insertion loss of the second version W-Band SPDT switch with and without RF pads . . . 57
56 Micrograph of the W-Band LBE on-chip antenna . . . 58
57 Measured and simulated input return loss of the W-Band antenna . . 59
58 Simulated gain and efficiency of the W-Band antenna in ADS . . . 59
59 Micrograph of the W-Band TPR without the antenna . . . 60
60 Micrograph of the W-Band TPR with the antenna . . . 61
61 Micrograph of the W-Band Dicke radiometer without the antenna . . 61
62 Micrograph of the W-Band Dicke radiometer with the antenna . . . 61
63 Detailed block level diagram of the dual channel radiometer architecture 63
64 Output of the R_{X1} and R_{X2} in the presence of gain fluctuations . . . 64
65 The schematic of the designed switch tree for W-Band dual receiver radiometer . . . 66
66 The simulated input and output return loss of the W-Band switch tree 66
67 The simulated insertion loss of the W-Band switch tree . . . 67
68 The simulated isolation of the W-Band switch tree . . . 67

69 Layout of the W-Band dual channel radiometer without the antenna . 69
70 Layout of the W-Band dual channel radiometer with the antenna . . 69
71 The schematic of the D-Band Power Detector 72
72 The EM simulation setup of the D-Band Power Detector 72
73 The schematic of the D-Band LNA 73
74 The EM simulation setup of the D-Band LNA 74
75 The schematic of the D-Band SPDT switch 75
76 The EM simulation setup of the D-Band SPDT switch 75
77 The EM simulation setup of the D-Band Antenna 76
78 Micrograph of the designed D-Band power detector 77
79 Simulated and measured S11 of the D-Band power detector 78
80 Simulated V_{OUT} difference vs P_{IN} of the D-Band power Detector at 140 GHz 78
81 Simulated NEP and responsivity of the D-Band power detector 79
82 Layout of the designed D-Band LNA 81
83 Simulated and measured S11 of the D-Band LNA 82
84 Simulated and measured S22 of the D-Band LNA 82
85 Simulated and measured gain of the D-Band LNA 83
86 Simulated noise figure of the D-Band LNA 83
87 Micrograph of the designed D-Band SPDT switch 85
88 Simulated and measured S11 and S22 of the D-Band SPDT switch at IL state 85
89 Simulated and measured S11 and S22 of the D-Band SPDT switch at isolation state 86
90 Simulated and measured IL of the D-Band SPDT switch 87
91 Simulated and measured isolation of the D-Band SPDT switch 87
92 Measured IL of the thru fixture 88
93 Simulated and deembedded measurement IL of the D-Band SPDT switch 88
94 Layout of the designed D-Band antenna 90
95 Simulated S11 of the D-Band antenna 91
96 Simulated gain and efficiency of the D-Band antenna 91
97 Layout of the implemented D-Band TPR 92
98 Layout of the implemented D-Band Dicke radiometer 92
99 The block diagram of a possible digital baseband implementation . . 97
100 An example block diagram of the setup to obtain 2D image using a single receiver and antenna [13] 99

List of Tables

1 Relative performance comparison of various Silicon and III-IV technologies (Excellent: ++; Very Good: +; Good: 0; Fair: –; Poor: – –) [14] 8
2 Summary of performance parameters for IHP 0.13 μm HBTs (SG13G2) 9
3 The emissivity of various materials at 44, 94 and 140 GHz [5] 16
4 Summary of performance of the W-Band PD and comparison with the SoA SiGe PDs 47
5 Summary of performance of the W-Band LNA and comparison with the SoA SiGe LNAs 50
6 Summary of performance of the W-Band SPDT and comparison with the SoA SPDTs 57
7 Summary of performance of the implemented radiometer systems and comparison with SoA W-Band radiometers 70
8 Summary of performance of the D-Band PD and comparison with the SoA SiGe PDs 80
9 Summary of performance of the D-Band LNA and comparison with the SoA SiGe LNAs 84
10 Summary of performance of the D-Band SPDT and comparison with the SoA SPDT switches 89
11 Summary of performance of the implemented radiometer systems and comparison with SoA D-Band radiometers 93

List of Abbreviations

AC	Alternating Current
ADC	Analog Digital Converter
AVHRR	Advanced Very High Resolution Radiometer
BEOL	Back End of Line
BJT	Bipolar Junction Transistor
BV_{CEO}	Collector-Emitter Breakdown Voltage
BV_{CBO}	Collector-Base Breakdown Voltage
BW	Bandwidth
CB	Common-Base
CE	Common-Emitter
CLK	Clock
CMOS	Complementary Metal-Oxide-Semiconductor
CPW	Coplanar Waveguide
CR	Correlation Radiometer
DC	Direct Current
DRC	Design Rules Check
DSP	Digital Signal Processor
EM	Electromagnetic
ENB	Effective Noise Bandwidth
FE	Front-end
FEOL	Front End of Line
FET	Field Effect Transistor
FPA	Focal Plane Array
GaAs	Gallium-Arsenide
GND	Ground
GSG	Ground Signal Ground
GSGSG	Ground Signal Ground Signal Ground
HBT	Heterojunction Bipolar Transistor
HEMT	High Electron Mobility Transistor
IC	Integrated Circuit
IF	Intermediate Frequency
IL	Insertion Loss
IR	Infrared
InP	Indium phosphide
LBE	Local Backside Etching
LNA	Low Noise Amplifier
LO	Local Oscillator
MAG	Maximum Available Gain
MIM	Metal-Insulator-Metal
MMIC	Monolithic Microwave Integrated Circuits
mm-Wave	Millimeter-wave
MS	Microstrip
MSL	Microstrip Line
NEDT	Noise Equivalent Delta Temperature
NEP	Noise Equivalent Power
NETD	Noise Equivalent Temperature Difference

NF	Noise Figure
NIR	Noise Injection Radiometer
PD	Power Detector
PGA	Programmable Gain Amplifier
PSD	Power Spectral Density
RADAR	Radio Detecting And Ranging
RF	Radio Frequency
RH	Relative Humidity
RMS	Root Mean Square
RX	Receiver
Si	Silicon
SiGe	Silicon-Germanium
SNR	Signal to Noise Ratio
SoA	State-of-the-Art
SoC	System-on-Chip
SPDT	Single-Pole Double-Throw
SPI	Serial Peripheral Interface
SSPARS	Solid State Phased Array RADAR System
TL	Transmission Line
TPR	Total Power Radiometer

1 Introduction

1.1 Imaging Systems

Imaging systems rely on the sensing or detection of electromagnetic waves. This basic principle allows one to observe an object or a scene for a given period of time with a receiver or number of receivers and construct an image based on the output of the system. In general there are two types of detection techniques: passive and active. In broad terms, these type of systems can also be classified into two categories; radiometers (passive) and RADAR (active). Active imaging systems "illuminate" the target by either a pulse or a continuous electromagnetic wave and the reflected and scattered waves are detected by the system which in return can give information on the distance, direction and the speed of the target [15]. To be able to illuminate the target, these type of systems have transmitters which are capable of transmitting high power beams to the target. On the other hand, passive imaging systems only detect the naturally occurring EM waves. Any object that has a physical temperature emits radiation which is known as the black-body radiation that is governed by Planck's law [16]. The targeted object can either emit radiation due to its own physical temperature or reflect radiation arising from other type of illuminator such as the sun or the background of the target. The strength of the emitted or reflected radiation depends on the physical temperature as well as the emissivity of the object. This dependence creates a contrast between warmer and colder objects in the scene in terms of signal strength which is picked up by the instrument and used to create the image [17]. An example image of the sea surface temperature constructed by Metop AVHRR (The Advanced Very High Resolution Radiometer) observations is shown in Fig. 1.

Active and passive imaging systems have been around for several decades. RADAR was first used in 1903 for military purposes and pulsed RADAR was developed in 1925 for remote sensing experiments. Radiometric systems appeared later in 1930s and 1940s for observing extraterrestrial objects and in 1950s, similar systems were used for terrestrial objects such as water, wood and grass [18]. The performance of such instruments have advanced greatly and became capable of performing more challenging tasks. An example of modern radiometer and RADAR systems are

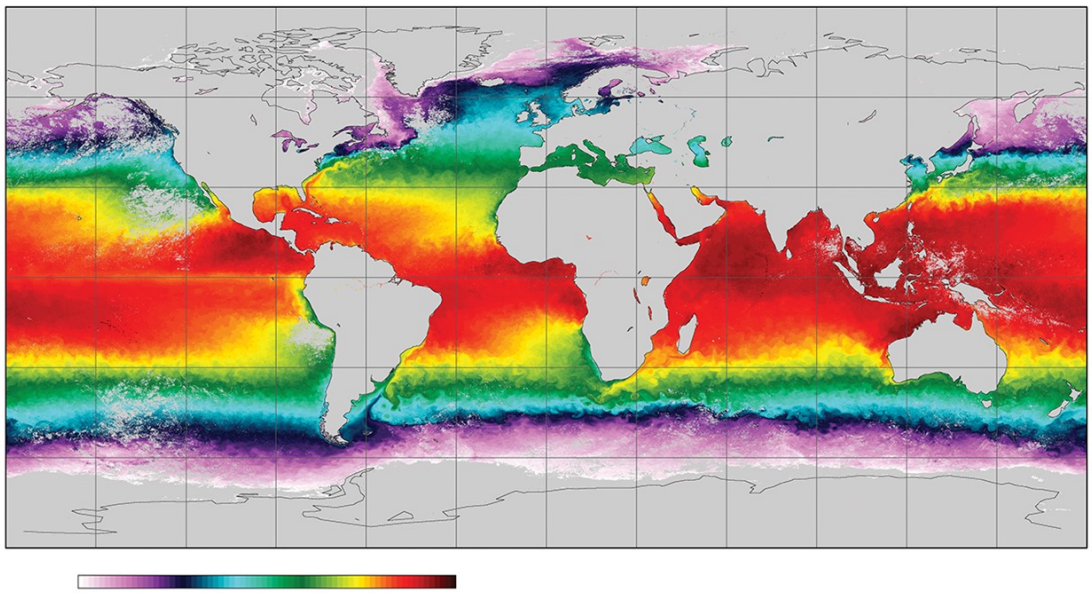

Figure 1: Global sea surface temperature derived from Metop AVHRR observations [1]

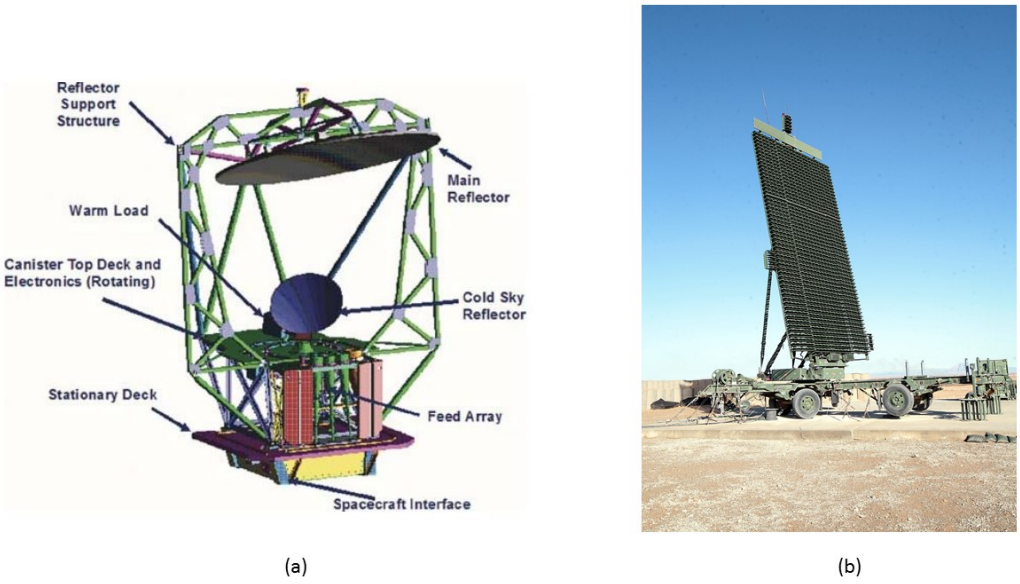

Figure 2: (a) WINDSAT polarimeter [2] and (b) AN/TPS-59 RADAR [3]

shown in Fig. 2 : (a) WINDSAT spaceborne microwave polarimeter (high-precision passive microwave imager) that measures polarized energy reflected from Earth, (b) AN/FPS-123 is a solid-state phased array radar system (SSPARS) used for ballistic missile warning.

Passive imaging systems have several strengths and weaknesses compared to an active system which make these systems suitable for different type of applications.

Passive systems operate on much lower intensity signals which means such systems need extremely low noise components to able to identify the incident signals. Active systems use transmitters to illuminate the scene, as a consequence incident signal power is much stronger and additional information on the scene could be obtained as in the case of RADAR. However, signal strength depends on the range in which the observation is performed therefore active imaging systems are mostly limited to observation of the objects in the earth. Another aspect is the operating frequency of the system. Different parts of the frequency spectrum provides unique features for different type of applications. For example as the frequency increase, spectral features of solid materials become more apparent but the depth of penetration of the signal is reduced which might be desirable for certain applications like concealed weapon detection [19]. Moreover, the addition of a transmitter for high frequency imaging increases the complexity of the system, if not impossible.

Radiometer systems became one of the trending topics in recent years for its crucial applications such as observation of soil moisture, wind speed and surface temperature measurements, monitoring oil spills, mapping ice-sheet melt conditions and various other security applications [4]. Along with the advancements in process technologies, high sensitivity radiometers will play an important role in these critical applications in the future of imaging systems.

1.2 mm-wave Radiometers

Operating frequency of a radiometer could be as low as several hundred MHz for solar flux measurements [20], or as high as THz levels for spaceborne applications [21]. The choice of frequency depends on the specific application and the unique features presented by the part of the spectrum.

Mm-wave spectrum (30-300 GHz) has several characteristics which makes it suitable for a wide range of radiometry applications. Some of the unique properties of mm-wave spectrum are: propagation through atmosphere with minimal attenuation, propagation through fog, rain, dust, haze and smoke, propagation through clothing and baggage, high thermal radiation power from humans relative to other objects, fine range and angular resolution due to short wavelength and wideband operation and also the ability to build smaller systems due to short wavelength [11].

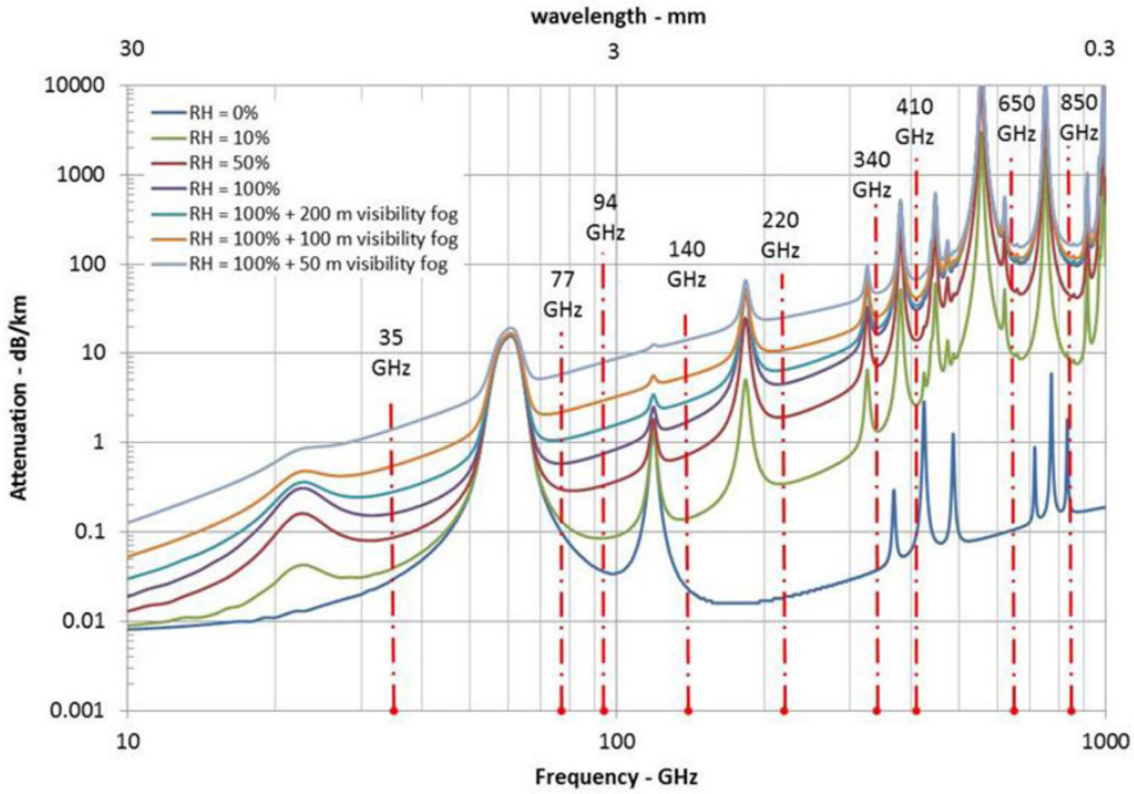

Figure 3: Atmospheric attenuation levels at various RH (Relative Humidity) and foggy weather conditions [4]

Many of the above mentioned properties are a result of exceptional propagation characteristics of mm-wave. Fig. 3 shows the attenuation levels from 10 GHz to 1 THz under various weather conditions. From the plot, peak attenuation levels at 60, 120 and 200 GHz can be seen and they mainly exist due to interactions with water and oxygen molecules that are present in the atmosphere [22]. However, it can also be seen that several atmospheric propagation windows are present at 94, 140 and 220 GHz where attenuation levels are low. These parts of the spectrum are also a window of opportunity for radiometric systems since the radiated power levels are already low and further attenuation would render the systems useless.

Attenuation through fog, rain and dust is another important parameter especially for applications that require imaging at low visibility or all weather conditions. The attenuation level is even more pronounced above mm-wave frequencies which makes sub-mm-wave and IR systems unsuitable for such applications. Fig. 4 shows how much the blackbody radiation intensity drops under foggy conditions.

Due to all these properties, mm-wave spectrum is appropriate for potential applications such as aircraft guidance, low visibility navigation, surveillance, beacon de-

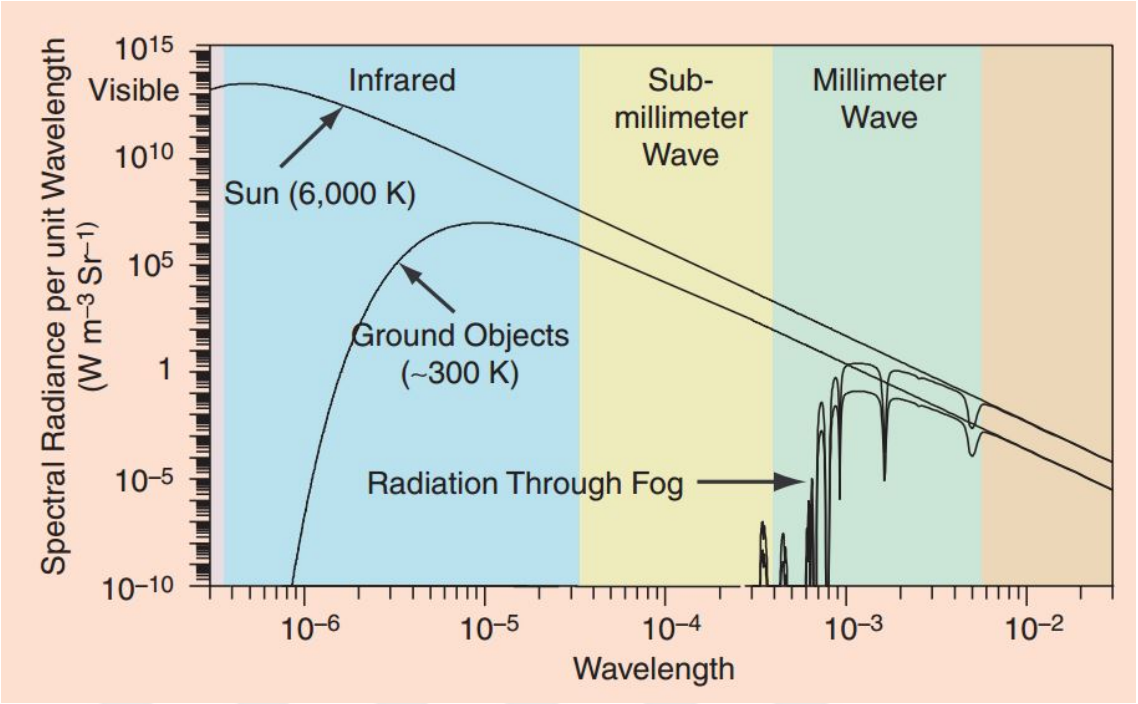

Figure 4: Blackbody radiation intensity at different wavelengths [5]

tection, oil spill detection, search and rescue, ground navigation, concealed weapons detection and many more [5].

1.3 MMIC Radiometers

Historically, radiometers have been implemented using special waveguide components to achieve high sensitivity [23]. This type of radiometers are inherently high cost and also large in size. Especially in space applications where the payload is critical, size and weight of the instruments are serious problems. The development in IC technologies have enabled the implementation of radiometers as system-on-chip (SoC) components. Another advantage of using MMIC radiometers is that it enables multiple receiver arrays on a much larger scale [24]. Such arrays can either be used to improve the resolution of the image, or can be combined together to improve the sensitivity. This feature give flexibility for realizing different type of radiometers depending on the application. One of the promising application is the earth observation through low cost small size CubeSats [25].

The cost is also another highlighted advantage. Radiometer instruments have been widely used in scientific research applications in which the cost of such instruments are of secondary importance compared to the performance of the systems.

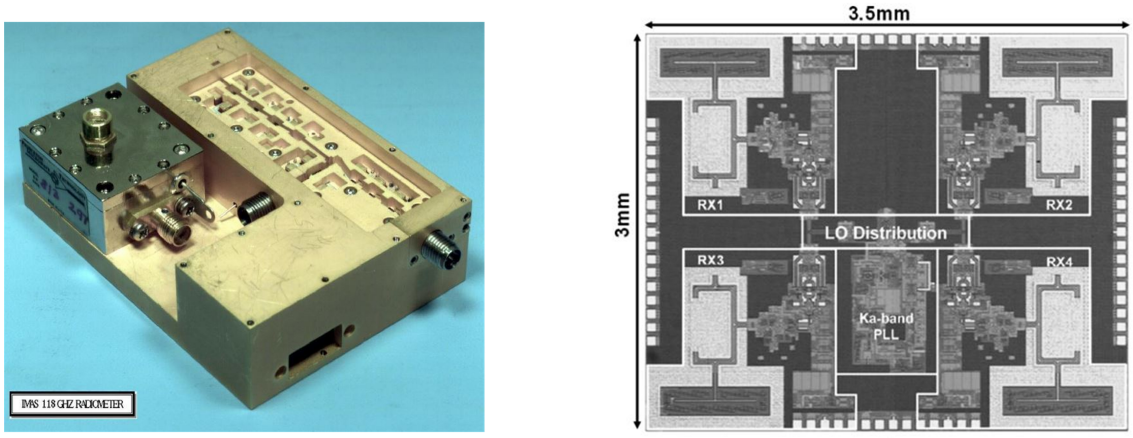

Figure 5: (a) 118 GHz IMAS Radiometer [6], (b) Fully integrated W-Band SoC for imaging applications [7]

MMIC radiometers have the potential to decrease the cost of the systems so new area of applications for commercial use are enabled. This advantage is even more emphasized considering that the silicon based technologies have recently caught up on performance to III-IV technologies such as GaAs or InP that have been used in earlier MMIC radiometers. III-V and silicon MMICs are now able to operate well above 100 GHz with sufficient performance for challenging applications (Fig. 5 (a)).

The performance of the silicon MMIC radiometers have been steadily increasing as well. Recent publications demonstrated silicon radiometers achieving NETD values from 2 K to 0.2 K in CMOS and SiGe BİCMOS technologies [26], [13]. Along with the performance, power consumptions are decreasing as well due to increasing f_t values of transistors. It is also important to note that, further integration other than front-end is becoming feasible with integrated circuit technologies. Front-end, baseband and the antenna can all be integrated on a single chip as shown in Fig. 5 (b) in advanced IC technologies. On top of these advantages, SiGe BiCMOS technology offers several unique properties that makes it suitable for radiometer applications including; one of the lowest $1/f$ noise, tolerance to high level of radiation and low-power thermal control and monitoring [27].

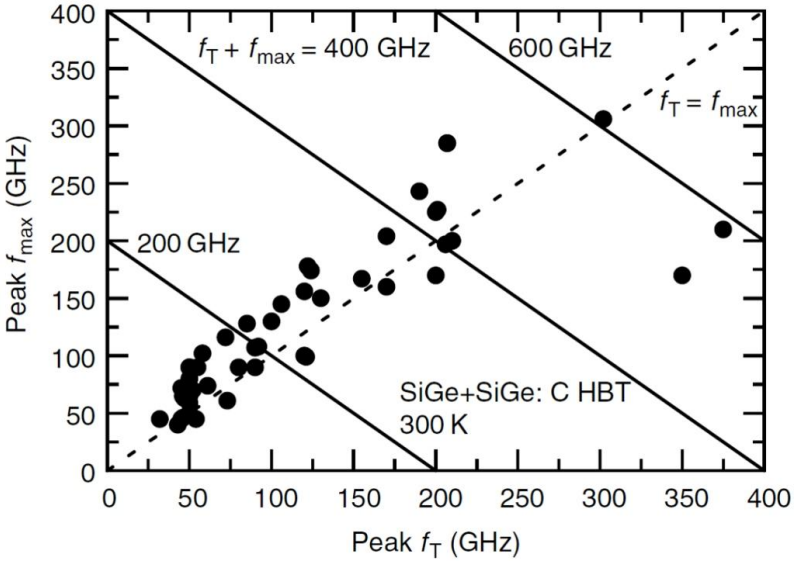

Figure 6: f_t and f_{max} values for various SiGe HBT technologies [8]

1.4 SiGe BiCMOS Technology

SiGe BiCMOS technology is one of the key enabling technologies for mm-wave and THz integrated circuits. Recent publications demonstrate f_t and f_{max} values of SiGe HBTs above several hundreds of GHz which are highly competitive to GaAs and InP technologies [28], [29]. Consequently, high performance MMICs are being developed featuring SiGe hetero-junction bipolar transistors (HBTs) for a variety of applications.

Bandgap engineering enables SiGe HBTs to achieve unprecedented cut-off frequencies in silicon based technologies. In the base of HBTs, SiGe alloys are epitaxially grown which has lower bandgap voltage than silicon due to germanium concentration which has a 0.66 eV of bandgap voltage. Therefore, higher current gain due to increased electron injection can be achieved. Moreover, the graded germanium doping reduces the base transit time which in return further improves cut-off frequency and maximum oscillation frequency [30]. These improvements are crucial for high frequency circuits since the performance is usually determined by f_t and f_{max} values. Fig.6 shows the f_t and f_{max} values for various SiGe HBTs. In addition to the performance, integration with CMOS transistors plays a critical role for highly integrated SoCs which III-IV technologies do not offer inherently. A comparison between SiGe HBTs versus III-IV and Si CMOS technologies is presented in Table 1.

Table 1: Relative performance comparison of various Silicon and III-IV technologies (Excellent: ++; Very Good: +; Good: 0; Fair: –; Poor: – –) [14]

Performance Metric	SiGe HBT	SiGe BJT	Si CMOS	III-V HBT	III-V HEMT
Frequency Response	+	0	0	++	++
1/f and Phase Noise	++	+	–	0	– –
Linearity	+	+	+	+	++
Transconductance	++	++	– –	++	–
Power Dissipation	++	+	–	+	0
CMOS Integration	++	++	N/A	– –	– –
IC cost	0	0	+	–	– –

The circuits presented in this thesis features HBTs with f_t/f_{max} values of 300/450 GHz in IHP's 0.13μm SiGe BiCMOS technology (SG13G2). The cross-section of this process is illustrated in Fig. 7. The back-end-of-line (BEOL) process is comprised of 7 aluminum metallization layers in which the top 2 layers are thick metals. The metal-insulator-metal (MIM) capacitors are formed between the TopMetal1 and Metal5 with a separate insulator layer with high relative permittivity. All the microstrip lines (MSLs) that are used in the circuits are implemented as TopMetal2-Metal1 which are 9.7 μm apart. All the other metals (M1-M5) are only used as bias and ground planes. The front-end-of-line (FEOL) process offers npn SiGe HBTs with an f_t of 300 GHz, f_{max} of 450 GHz and collector-emitter breakdown voltage (BV_{CEO}) of 1.7 V as well as polysilicon resistors with a sheet resistance of 275 Ωcm.

The process also features local backside etching (LBE) in which the thick silicon substrate is etched locally to realize high-Q inductors, low loss transmission lines or high efficiency antennas. The etching of the high relative permittivity (ϵ_r) silicon substrate is especially useful for antennas where the dominant loss mechanism is the thick backside substrate. Fig. 8 shows the cross section of the LBE process.

Finally, Table 2 presents the summary of performance parameters of the npn HBT featured in IHPs 0.13 μm process.

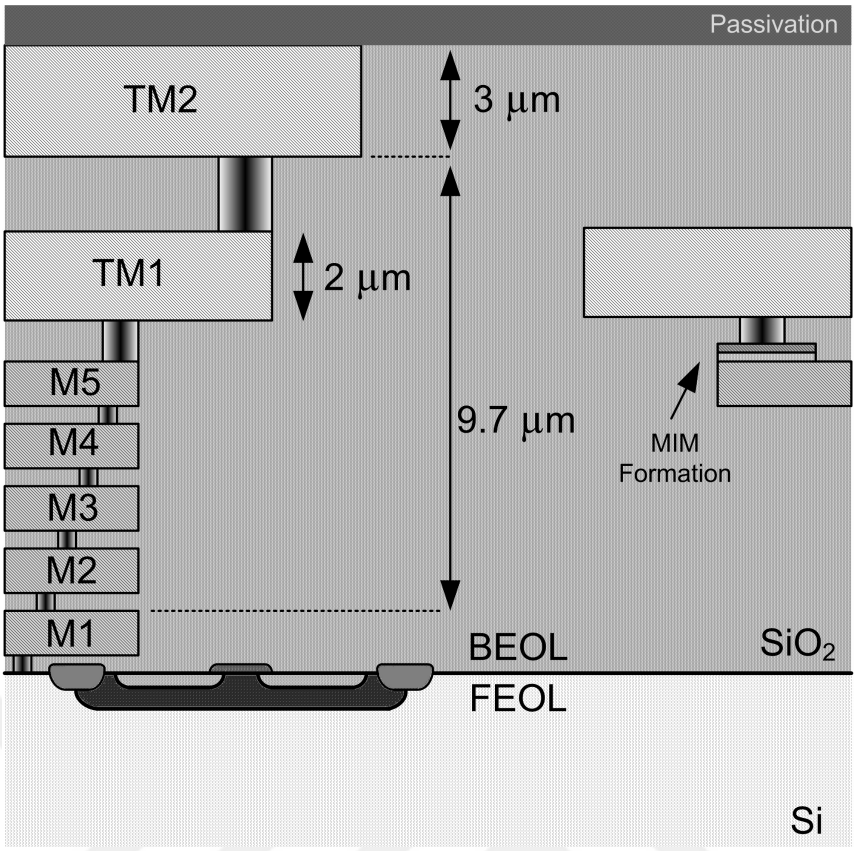

Figure 7: Cross section of the IHP 0.13 μm SiGe HBT process (SG13G2)

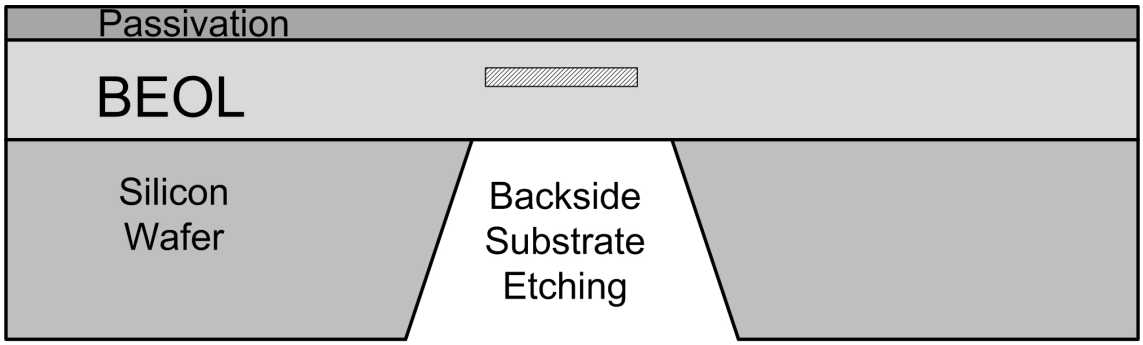

Figure 8: Cross section of the LBE process in IHP 0.13 μm SiGe HBT technology

Table 2: Summary of performance parameters for IHP 0.13 μm HBTs (SG13G2)

peak f_T	300 GHz
peak f_{MAX}	450 GHz
peak β	700
I_C @ peak f_T	2 mA per transistor
BV_{CEO}	1.7 V

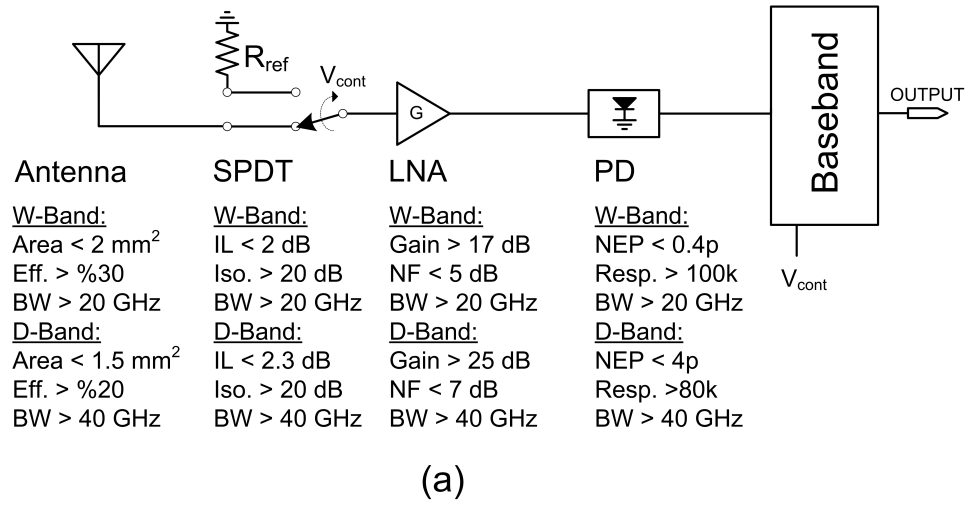

(a)

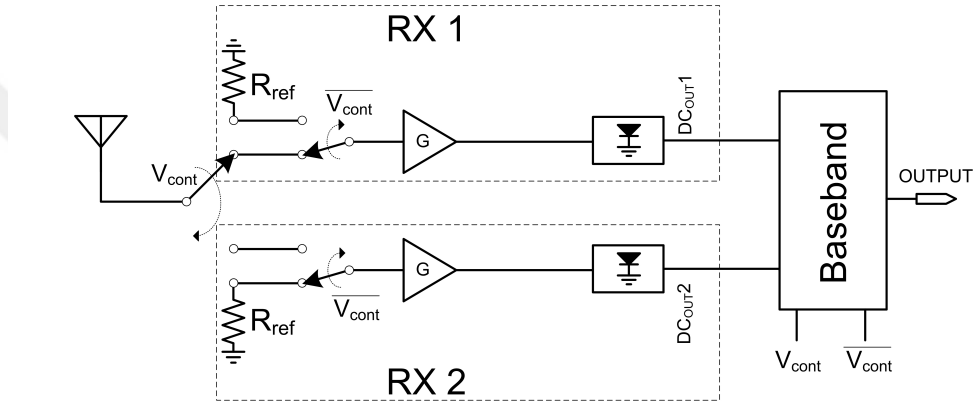

(b)

Figure 9: (a) System block diagram of the proposed W-Band and D-Band Dicke radiometers (b) System block diagram of the W-Band dual receiver Dicke radiometer

1.5 Motivation

In the light of the advancements in silicon based technologies and various new application areas for mm-wave passive imaging systems, the objective of this thesis is set to design of highly integrated front-end receiver systems at W-Band (75-110 GHz) and D-Band (110-170 GHz) for radiometry applications. Until recently, high frequency integrated circuits were subject of III-IV technologies. However, SiGe BiCMOS technology is becoming one of the established technologies in mm-wave

ICs and is also breaking new grounds with f_t values of 300 GHz and above. The W-Band and D-Band as two of the most significant frequency bands in radiometry applications due to its unique propagation characteristics, are being utilized in an unprecedented rate for new set of applications ranging from concealed weapon detection to low visibility detection. Due to the low cost and high yield of SiGe BiCMOS technology compared to III-IV technologies, such applications can be enabled and even more applications can emerge for commercial or scientific use. Moreover, the low $1/f$ noise, radiation tolerance and low power dissipation of the SiGe HBTs make it especially useful for realizing highly sensitive radiometer systems.

Another important feature of SiGe BiCMOS technology is the level of integration that is possible for receiver systems. The CMOS integration is essential to realize baseband processing in a single chip. The III-IV technologies do not have this opportunity inherently and require specialized and relatively high cost processing techniques for integration. Low frequency amplifiers, demodulators, integrators and ADCs are all part of the radiometer system which can be designed using CMOS transistors provided with the technology without increasing the cost and total system area.

The back-end process is also highly essential to design front end circuitry with low loss components especially in high frequencies. The antenna is a fundamental part of a radiometer system, and advanced back-end processes such as LBE which is also provided by the technology, is a unique opportunity to design high efficiency on-chip antennas. Off-chip antennas that are widely utilized in radiometer systems increase the cost and area of the system. Such advanced back-end processes can be employed in the design of on-chip antennas for completely integrated radiometer systems.

With all the advantages of the SiGe BiCMOS technology, it is more than feasible to design highly integrated W-Band and D-Band radiometer systems with an NETD of 0.5 K or better. Therefore, this thesis aims to present design methodology and results of building blocks of radiometer front-ends, namely SPDTs, LNAs, power detectors (PDs) and antennas in both W-Band and D-Band as well as the completed single-chip receivers. The block diagram and the targeted performance parameters of the proposed receivers are presented in Fig. 9 (a).

A new dual receiver Dicke radiometer is also proposed in this thesis in an attempt to enhance the radiometer sensitivity even further which is shown in Fig. 9 (b). The proposed radiometer theoretically enhances the NETD of the system by a factor of $\sqrt{2}$ by doubling the effective integration time. The proposed dual receiver architecture is implemented using W-Band LNA, PD and a unique switch tree.

1.6 Organization

The thesis is organized as follows. Chapter 2 introduces radiometry fundamentals. First, the detection principle in terms of emitted power and received power by the system is presented. The theoretical sensitivity of the Total Power Radiometer is analyzed and limiting factors to achieve high sensitivity are illustrated. This analysis is followed by the investigation of various different radiometer architectures.

Chapter 3 includes the system level analysis of W-Band radiometer as well as the sub-blocks. Design approach and implementation of the W-Band PD, LNA, SPDT and antenna are presented. Simulation and measurement results of the sub-blocks are discussed. System implementations are illustrated for different architectures, including TPR, Dicke radiometer and dual receiver radiometer. The corresponding NETD values are investigated for these systems.

Similar to Chapter 3, Chapter 4 includes system level analysis and design and measurement results of the D-Band radiometer and sub-blocks of this radiometer. Simulation and measurement results are compared and investigated. The implemented receiver front-end ICs are illustrated and analyzed for achievable sensitivity.

Finally in Chapter 5, a conclusion is drawn in terms of achieved specifications and problems encountered throughout the implementation of the systems. Also, possible future work is presented.

2 Radiometer Fundamentals

2.1 Detection Principles

In essence, a radiometer is a sensitive receiver that detects the radiation emitted from the observation area through an antenna looking down the scene. Fig. 10 describes the basic operation principle. An antenna with radiation pattern $A(\theta, \phi)$ is targeted at a scene with brightness temperature T_B . Total observation area is determined by the half power beam width of the antenna and the other optics involved. The received power is proportional to the sum of T_B and the scattered radiation from the scene, T_{SC}, that arise from the background temperature, T_{BG}. The radiation power picked up by the antenna is fed to a low noise receiver and the output is generated either in terms voltage or ADC counts that represents the brightness of the scene.

The electromagnetic radiation emitted from the source or any object is due to its physical temperature is known as black-body radiation. A blackbody, or a perfect

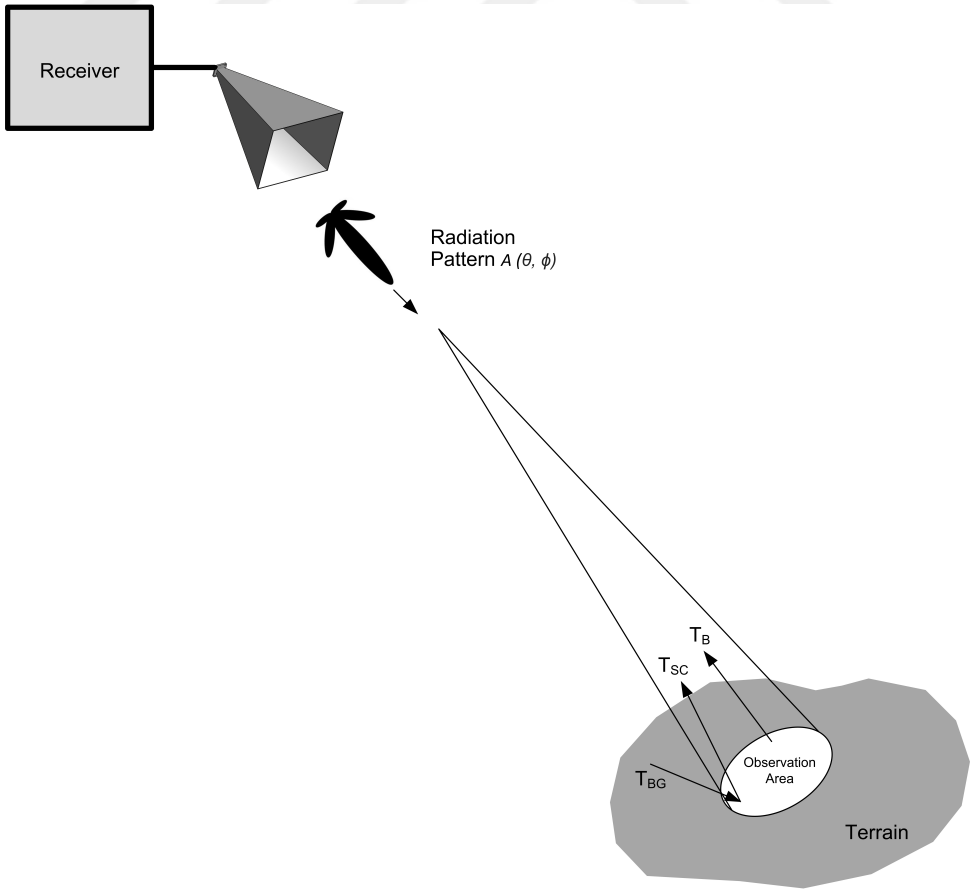

Figure 10: Basic operating principle of a radiometer

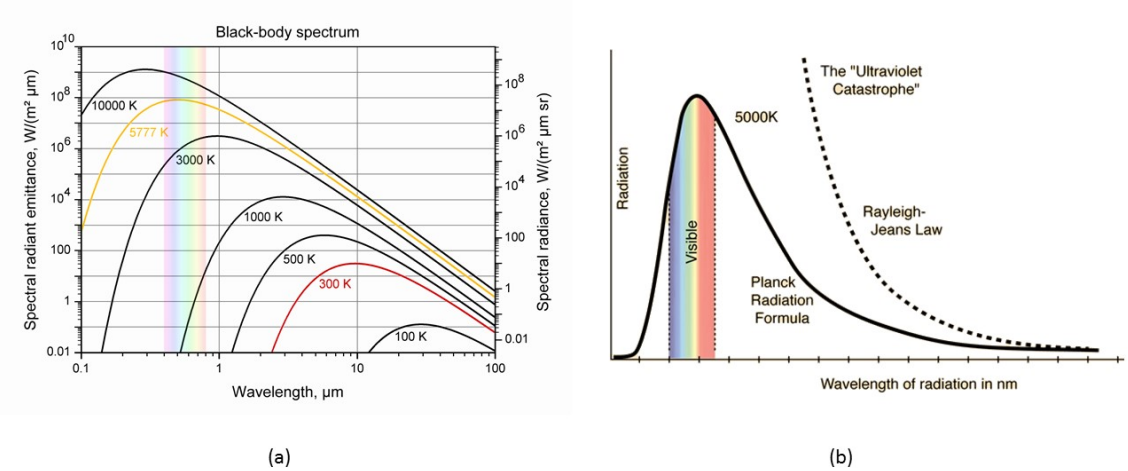

Figure 11: (a) Spectral brightness of a blackbody [9] , (b) Approximation of Plank's law by Rayleigh Jeans law [10]

radiator has the spectral brightness of

$$B_\lambda(\lambda, T) = \frac{2hc^2}{\lambda^5} \frac{1}{e^{hc/\lambda kT} - 1} \tag{1}$$

given by Planck's Law in terms of wavelength where B_λ has the units of $Wsr^{-1}m^{-3}$, h is the Planck's constant, λ is the wavelength, c is the speed of light and k is the Boltzmann constant [31]. Fig. 11 (a) shows the spectral brightness of a blackbody where the peak radiation wavelength is dependent on the temperature. In mm-wave region, a much simpler approximation of Planck's Law is useful, given by Rayleigh-Jeans Law:

$$B_\lambda(\lambda) = \frac{2v^2kT}{c^2} \tag{2}$$

that holds true when $hf << kT$ which is accurate in mm-wave (Fig. 11 (b)) [32].

The amount of power receiver by the antenna can be calculated following the procedure described in [11]. Considering the case illustrated by Fig. 12, the power at the surface A_r radiated by the target A_t, is found by integrating the infinitesimal power at the surface:

$$dP = B_f(f, \theta, \phi) cos\theta d\Omega dA df \tag{3}$$

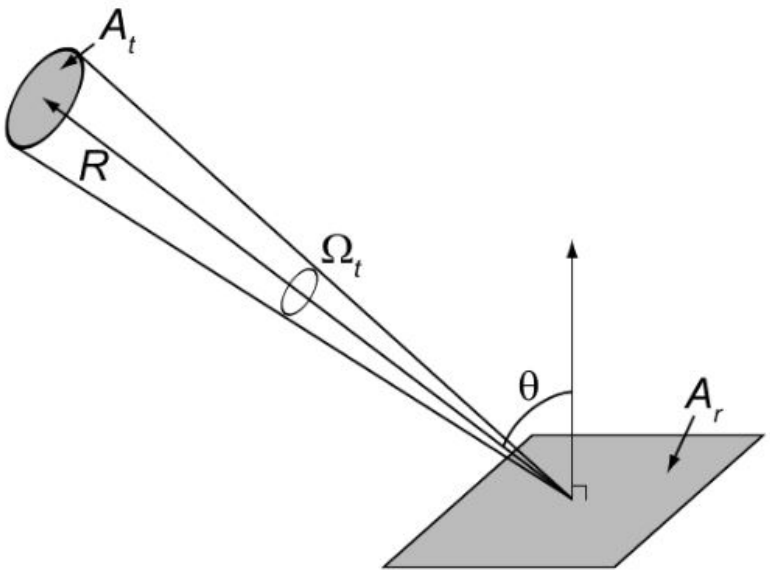

Figure 12: Illustration of the power incident of the receiving aperture A_r, emitted from the surface A_t [11]

over the solid surface Ω , total area A_r and the frequency bandwidth of the system, f, which then becomes

$$P = \int_f \int_{A_r} \iint_{\Omega} B_f(\theta, \phi) cos\theta d\Omega dA df \tag{4}$$

where B_f is the spectral radiance approximated by Rayleigh Jeans law. The frequency dependency of the equation can be dropped by integrating Rayleigh jeans equation over the bandwidth Δf which would yield

$$B = \frac{2kT}{c^2}\left(f^2\Delta f + \frac{1}{12}\Delta f^3\right) \tag{5}$$

Assuming the brightness is constant over the hemisphere and the incident radiation is constant across the surface the power becomes simply

$$P = \pi A_r B \tag{6}$$

Finally, if we take antenna radiation pattern into account, (4) becomes

$$P = \frac{1}{2} A_e \int_f \iint_{\Omega} B_f(\theta, \phi) A(\theta, \phi) d\Omega df \tag{7}$$

where A_e is the effective aperture of the antenna, $A(\theta, \phi)$ is the radiation pattern

Table 3: The emissivity of various materials at 44, 94 and 140 GHz [5]

	Effective Emissivity		
Surface	**44** GHz	**94** GHz	**140** GHz
Bare metal	0.01	0.04	0.06
Painted metal	0.03	0.10	0.12
Painted metal under canvas	0.18	0.24	0.30
Painted metal under camouflage	0.22	0.39	0.46
Dry gravel	0.88	0.92	0.96
Dry asphalt	0.89	0.91	0.94
Dry concrete	0.86	0.91	0.95
Smooth Water	0.47	0.59	0.66
Rough or hard-packed dirt	1.00	1.00	1.00

which replaces $cos\theta$ and the 1/2 term is placed for polarization effects.

So far, all the calculations presented above were for ideal blackbody sources. In reality ideal blackbody sources do not exist. The term emissivity is measure of radiating capability of an object compared to a blackbody [33]. The emissivity is the ratio between the brightness temperature T_B and the physical temperature of the object:

$$e = T_b/T \tag{8}$$

The emissivity of an object may depend on the frequency, direction and temperature [34]. A good emitter would have an emissivity close to 1 and a good absorber close to 0. In general, metals have low emissivity values whereas other common materials have emissivity values much higher. This is the reason why, metal objects appear "colder" in radiometric images as their brightness temperature T_B is lower. A brief table of emissivity of some objects at various frequencies are given in Table 3.

The emitted radiation of the target is not the only source of radiation and the background radiation is also picked up by the antenna. The emissivity term (ϵ) and the reflectivity (ρ) which is $1 - \epsilon$, determines the total brightness temperature of the target scene detected by the radiometer:

$$T_E = T_S + T_{SC} = \epsilon T_0 + \rho T_{ILLUMINATOR} \tag{9}$$

which is described by Fig. 12.

Equations (6) and (7) can be used together to estimate the power incident on the receiving antenna. Assuming 20 GHz of bandwidth at 100 GHz center frequency, 1 mm^2 effective antenna aperture with an isotropic pattern and a scene temperature of 290 K, the spectral brightness P of a perfect radiatior is calculated to be $1.79 \cdot 10^{-5}$ kg/s^3 and the power is $5.62 \cdot 10^{-11} W$ which corresponds to approximately -83 dBm. For an object with an $\epsilon = 0.1$, the input power would be -93 dBm. Obviously, the received power could be increased depending the antenna pattern, gain and effective aperture area, but even with these improvements, the received power would be no more than approximately -70 dBm which is still significantly low and cannot be measured or sensed without specifically designed receivers.

2.2 Theoretical Sensitivity

As shown in the previous section, the input power of a radiometer is usually considerably low, therefore the receiver should also be capable enough to detect such signals. The simplest detection scheme would be a square law detector placed after the antenna but detectors are extremely noisy components so in order to surpass the noise, an LNA must be placed after the antenna which also acts as a bandpass filter. A power detector would generate a DC voltage proportional to the input power which is accompanied by an AC signal.The output of the detector is then averaged for a period of time which removes the AC part of the output signal. The mentioned receiver scheme is also called the Total Power Radiometer (TPR). The sensitivity of the radiometer, NETD (Noise Equivalent Temperature Difference), or as it sometimes called NEDT (Noise Equivalent Delta Temperature), is defined as the RMS output voltage per incremental change in mean output DC voltage with respect to temperature expressed by (10) ([35]).

$$NETD = \Delta T_S = \frac{\sqrt{P_{out,AC}}}{\frac{\partial \sqrt{P_{out,DC}}}{\partial T}} \tag{10}$$

To find the NETD of the TPR, consider the receiver block diagram shown in

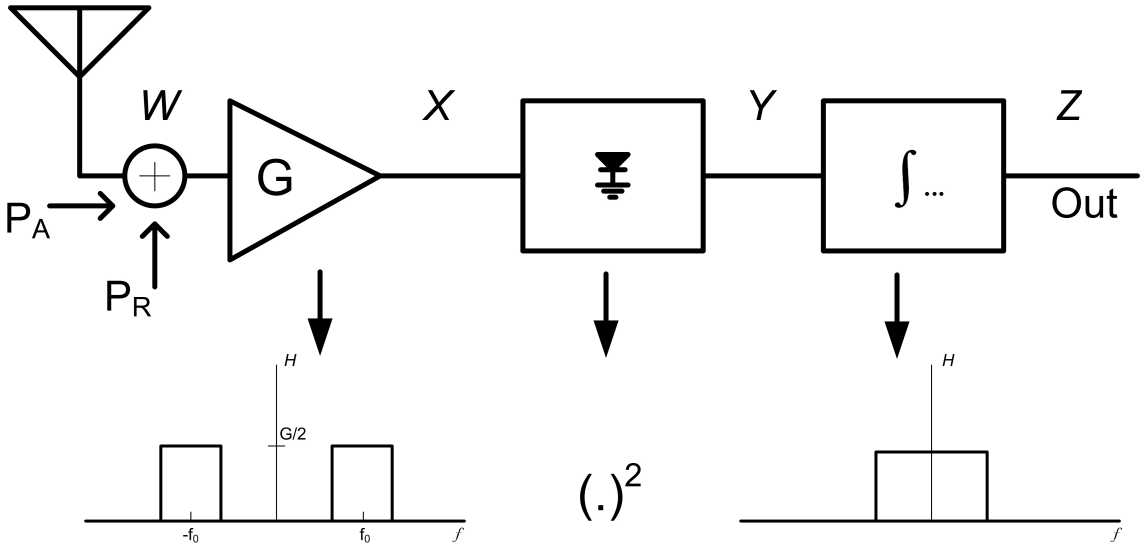

Figure 13: Block diagram of the Total Power Radiometer

Fig. 13 where the effect of antenna and LNA is represented by an ideal bandpass filter with bandwidth B and height $G/2$.

T_A represents the brightness temperature of the scene and T_R is the input referred noise temperature arising from the electronic noise due to transistors, resistors and other components of the receiver. Since they are uncorrelated, the power spectral density at the input of the bandpass filter would be the sum of two:

$$S_W(f) = k(T_A + T_R) = kT_{eff} \tag{11}$$

The PSD at the output of the filter is found by multiplying by the transfer function of the filter:

$$S_X(f) = \frac{kT_{eff}G}{2}\left[rect(\frac{f-f_0}{B}) + rect(\frac{f+f_0}{B})\right] \tag{12}$$

Then the total power would be its autocorrelation at $\tau = 0$ where τ is the integration time, would be

$$R_X(0) = E\left[X^2(t)\right] = \int S_X(F)df = kT_{eff}BG \tag{13}$$

Since square law detector is not linear, one needs to find the autocorrelation function of the detector

$$R_Y(\tau) = E\left[X^2(t)\right] E\left[X^2(t+\tau)\right] + 2E\left[X(t)X(t+\tau))\right] E\left[X(t)X(t+\tau))\right] \quad (14)$$

$$= R_X^2(0) + 2R_X^2(\tau) \quad (15)$$

Taking the Fourier transform of the this function the PSD at the output of the detector is found to be

$$S_Y(f) = (kT_{eff}BG)^2\delta(f) + \frac{(kT_{eff}G)^2B}{2}\left[2tri(\frac{f}{B}) + tri(\frac{f-2f_0}{B}) + tri(\frac{f+2f_0}{B})\right] \quad (16)$$

Equation (16) has two parts, a DC part which is the left part of the summation and the rest is the AC part. The desired DC part is obtained by placing a low pass filter or an averaging filter at the end of the receiver that partially removes the AC part. Then the DC output would be the multiplication of the transfer function of the filter and the DC part of (16) :

$$P_{Z_{DC}} = |H_2(0)|^2 S_{Y_{DC}}(0) \quad (17)$$

where the transfer function is defined as

$$H_2(f) = \tau sinc(\tau f)e^{-j\pi f\tau} \quad (18)$$

Then the DC output power is found to be:

$$P_{Z_{DC}} = |H_2(0)|^2 S_{Y_{DC}}(0) = \tau^2(kT_{eff}BG)^2 \quad (19)$$

The AC output is found by integrating the multiplication of the $H_2(f)$ and the AC part of (16). Here, the approximation $1/\tau << B$ can be made since integration times are usually much longer than the bandwidth of the receiver. As a consequence most of the power will come from the AC part at $f = 0$. The total AC output power becomes:

$$P_{Z_{AC}} = \int |H_2(f)|^2 \, S_{Y_{AC}}(0) df \tag{20}$$

$$= (kT_{eff}G)^2 B\tau \tag{21}$$

We can use the result found in (19) and (21) to find the NETD of the system given by (10), which would result:

$$NETD = \Delta T_S = \frac{\sqrt{P_{out,AC}}}{\frac{\partial\sqrt{P_{out,DC}}}{\partial T}} = \frac{kT_{eff}G\sqrt{B\tau}}{kGB\tau} = \frac{T_{eff}}{\sqrt{B\tau}} \tag{22}$$

The implications of (22) are straightforward: to keep the system sensitivity high, the effective bandwidth of the receiver should be wide and the receiver noise should be as low as possible. The integration time however depends on the application and is determined by the video bandwidth and is related by

$$\tau = \frac{1}{2B_v} \tag{23}$$

where B_v is the video bandwidth. A typical choice of τ for radiometers at W-band is 30-40 ms [36–38].

For imaging applications, 1 K temperature sensitivity or better is usually required to achieve decent quality [39]. Assuming 20 GHz of RF bandwidth and 30 ms integration time, the maximum T_{eff} for 1 K NETD needs to be approximately 24500 K.

For simplification, the calculations presented above did not include gain fluctuations of the amplifier. However, the low frequency gain changes have a significant effect on the radiometer sensitivity since the output signal power is directly affected by the LNA gain. In the presence of these fluctuations, the NETD equation becomes

$$NETD = T_{eff}\sqrt{\frac{1}{B\tau} + \left(\frac{\Delta G}{G}\right)^2} \tag{24}$$

as expressed by [40]. Using the same assumptions and T_{eff} of 24500 K, and also including only %0.1 gain fluctuation, the new NETD becomes 24.5 K, compared to 1 K found out earlier. This result shows how significant the effect of the gain fluctuation term is for system sensitivity. Fortunately, this effect can be minimized

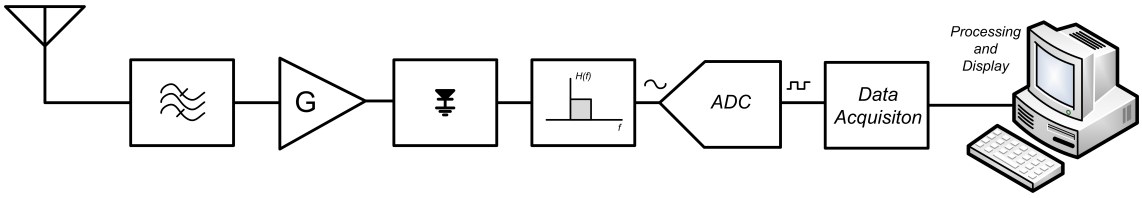

Figure 14: Detailed block diagram of the direct detection Total Power Radiometer

to some extent by using various calibration techniques which will be explained in the following chapter.

2.3 Radiometer Architectures

2.3.1 Total Power Radiometer

The detailed block diagram of the direct detection TPR is shown in Fig. 14. Detection scheme is relatively straightforward in this configuration. A detector is placed at the end of the front-end receiver which generates an output signal proportional to the received power. The detector can be realized by either semiconductor diodes or transistors which act as a square-law detector. The non-linearity of the circuit is exploited to generate a second order harmonic response which becomes the DC output signal and the first order harmonics are cancelled through capacitors. The same detector has to be preceded by a low noise amplifier since the detectors are inherently extremely noisy components. Depending on the technology and the application, the required gain of the LNA can be as high as 40-50 dB or more. The output signal is integrated for a period of time, τ, which can be realized simply by adding a low pass RC filter. The output noise bandwidth is limited by the filter and the output signal is smoothed. The increased τ results in a less noisy output, however the duration of the integration time is limited by the application requirements. Finally, the smoothed output can be converted to ADC counts and processed by a computer. The averaging scheme can either be done in analog domain or digital domain, i.e. the output signal can be first converted to digital signal by an ADC and processed later by a computer or a DSP.

Unfortunately, the gain fluctuations of the LNA pose a serious threat to the sensitivity of the receiver as shown in the previous section. The $1/f$ noise arising from the components, result in gain fluctuations and the detected signal power changes

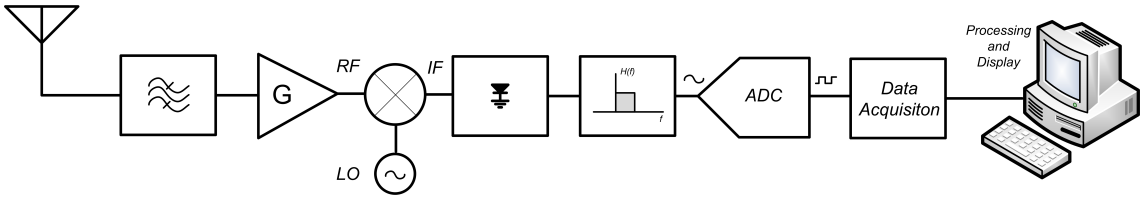

Figure 15: Detailed block diagram of the heterodyne Total Power Radiometer

by these fluctuations. This type of noise cannot be smoothed by the integrator since the duration of integration is typically much smaller than the duration of the low frequency fluctuations. A more detailed NETD equation for the TPR is presented in [41]

$$NETD = \frac{1}{\alpha}\sqrt{\left[2(\alpha T_A + (F-\alpha)T_0)^2 + (\frac{V_n}{k\beta G})^2 \frac{1}{B}\right]\frac{1}{2B\tau}} \tag{25}$$

where α is the attenuation factor of the components preceding the LNA, F is the LNA noise and G is the LNA gain , T_A is the noise equivalent temperature of the antenna, T_0 is the physical temperature of the receiver, k is the Boltzmann constant, V_n is the RMS noise voltage and β is the responsivity of the detector, B is the RF bandwidth and τ is the integration time. Also, the effective RF bandwidth of the receiver can be calculated as [42]

$$B = \frac{(\int_0^\infty FG\beta df)^2}{\int_0^\infty (FG\beta)^2 df} \tag{26}$$

In general, the radiometer systems can be implemented as either direct detection receiver (Fig. 14) or heterodyne receiver (Fig. 15). In the heterodyne scheme, a local oscillator (LO) is placed along with a mixer to downconvert the received RF signal to IF frequency. If the LO signal and RF signal are of same frequency, this scheme is called homodyne receiver. There are several advantages of the heterodyne or homodyne scheme over the direct detection. Since the RF signal power is quite low, mixing this signal with a strong LO signal amplifies it and improves the sensitivity. Also, amplifiers at lower frequency (IF) are expected to have greater performance and lower cost. However, the reduced bandwidth and additional complexity introduced, limit the use of heterodyne or homodyne receivers in wideband applications [43].

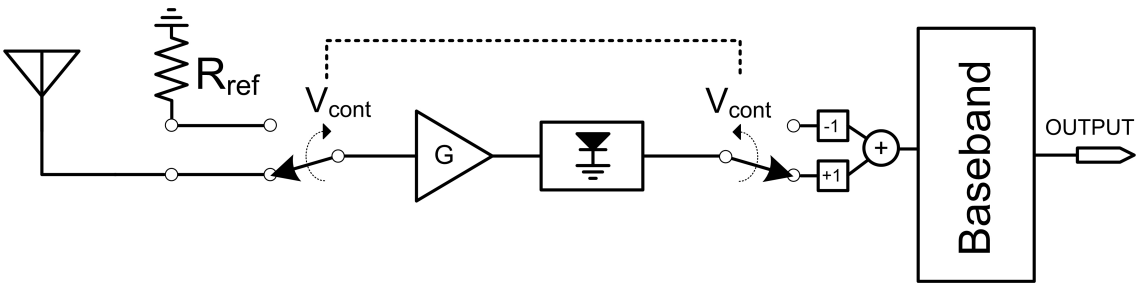

Figure 16: Detailed block diagram of the Dicke Radiometer

2.3.2 Dicke Radiometer

An ingenious solution to the problem associated with the gain fluctuations was first proposed by R. Dicke in 1946 [44]. The schematic of the Dicke radiometer is shown in Fig. 16. In this configuration, a switch is placed after the antenna that alternates between the reference resistor R_{ref} and the antenna. The power detector measures the received antenna power when the switch is directed to the antenna which can be called the observation period, and the noise power of the R_{ref} is measured for a period of time when the switch is directed to R_{ref}, which can be called the calibration period. When low frequency fluctuations occur at the LNA, the gain of the LNA becomes $G + \Delta G$ and the output of the detector increases proportional to the gain. The switching period is set to be much smaller than the period of the fluctuation, such that the gain can still be considered as $G + \Delta G$ after the observation cycle is completed. Consequently, at the calibration cycle, the output voltage is still increased by the same proportion. The difference is then taken by a synchronized demodulator, placed after the detector. As a result the difference is not effected by the gain fluctuation therefore it is removed to some extent. Essentially, the output spectrum is shifted from DC to switching frequency which is higher than the $1/f$ noise corner of the system. The remaining noise is much smaller and is removed by averaging the corresponding output signals.

There are several drawbacks of such a system. First, the assumption that the noise power of the R_{ref} is equal to antenna noise temperature has to be made to completely remove the effect of gain fluctuations. This assumption is not too far off from the reality since both the scene temperature and the physical temperature of the R_{ref} are close to the temperature of the environment where they are placed. Slight changes in the receiver temperature compared to the scene temperature means that

the gain fluctuation term is not completely removed, nevertheless it is minimized. Second, the switch has to be placed in front of the LNA, therefore the loss of the switch increases the noise temperature of the system. Third, the effective observation time is halved since half of the integration period (assuming %50 duty cycle) is spent measuring the power of R_{ref} which in return reduces the system sensitivity by a factor of 2. As a result the NETD equation for the Dicke radiometer becomes :

$$NETD = \sqrt{\frac{4}{B\tau}\frac{1}{2}\left[(T_A + T_N)^2 + (T_R + T_N)^2\right] + (T_A - T_R)^2(\frac{\Delta G}{G})^2} \tag{27}$$

where T_R is the temperature of the R_{ref}, T_A is the antenna noise temperature and T_N is the receiver noise temperature [45]. Assuming $T_R = T_A$, (27) reduces to

$$NETD = \frac{2(T_A + T_N)}{\sqrt{B\tau}} \tag{28}$$

Even with the penalty of two for switching operation and increased T_N, the improvement in sensitivity is much greater compared to the TPR which is why Dicke switching or similar periodic calibration techniques are being utilized in modern radiometer systems.

In general, the periodic calibration technique can be implemented without the switch by the means of mechanical scanning. In such a setup, one or more calibration scenes with known temperatures can be observed periodically along with the target scene which is illustrated in Fig. 17 [40]. The effective observation time is still reduced but the additional loss of the switch is avoided in this case. However, such mechanical scanning techniques introduces additional complexity to the system and is not always preferred.

2.3.3 Other Architectures

The total power radiometer and the Dicke radiometer are two of the most common architectures used in radiometer systems. Many other systems are in part, variants of these types. The noise injection radiometer (NIR) and correlation radiometer (CR) are two widely used examples.

The block diagram of the NIR is presented in Fig. 18. In previous section, it is shown that the gain fluctuations can be removed in the case that the reference noise

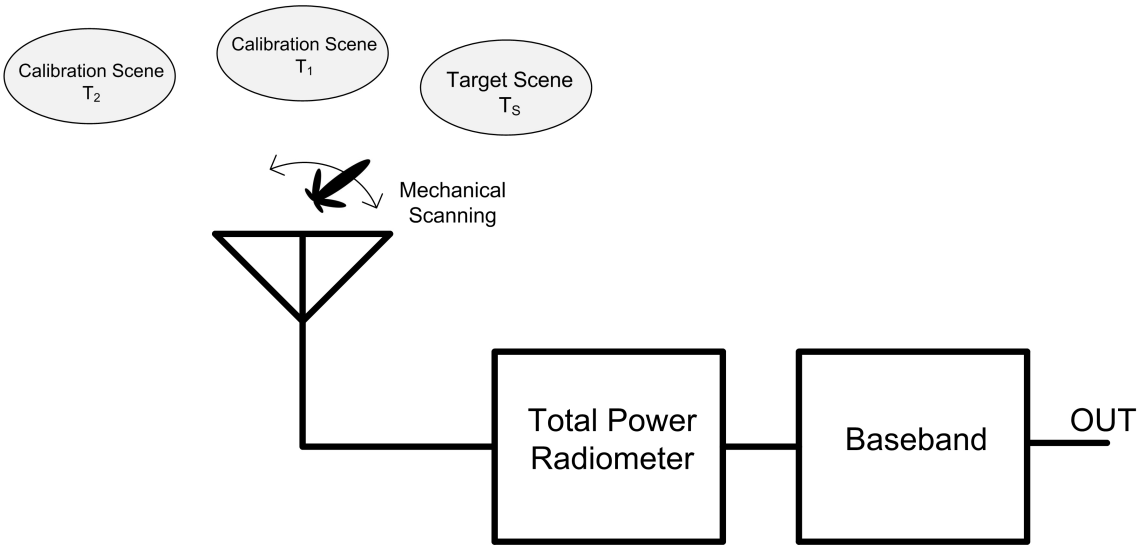

Figure 17: Illustration of the periodically calibrated radiometer with mechanical scanning

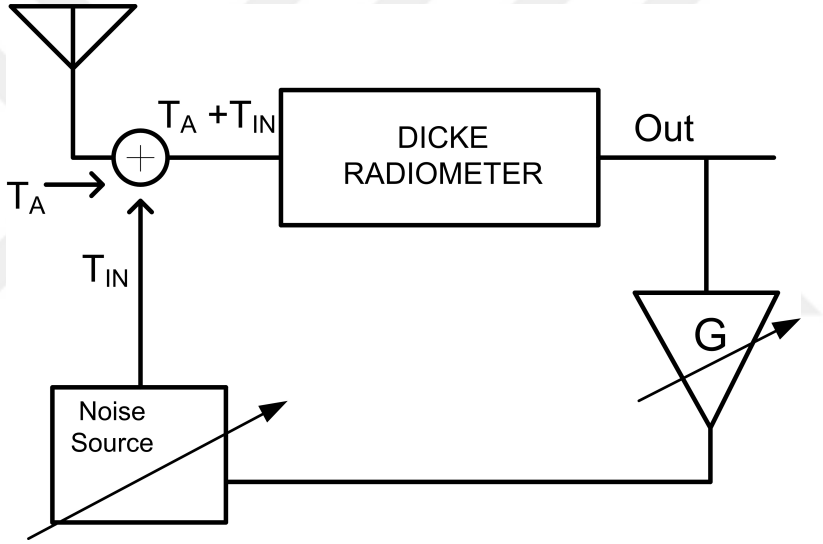

Figure 18: Block diagram of the noise injection radiometer

temperature is equal to the antenna temperature for the Dicke radiometer. In the generalized case where this assumption is not true, the NIR system is proven to be useful. It is basically a Dicke radiometer with additional loop gain and adjustable noise source. When the antenna temperature is less than the reference temperature, noise is injected in to the radiometer such that the sum of the antenna and injected noise temperature is equal to the reference temperature [46]. The amount of noise injected is adjusted through the loop gain. Consequently the NETD of the NIR is equal to (28) but with a greater accuracy than the Dicke radiometer.

Another architecture is the correlation radiometer illustrated in Fig.19. In this

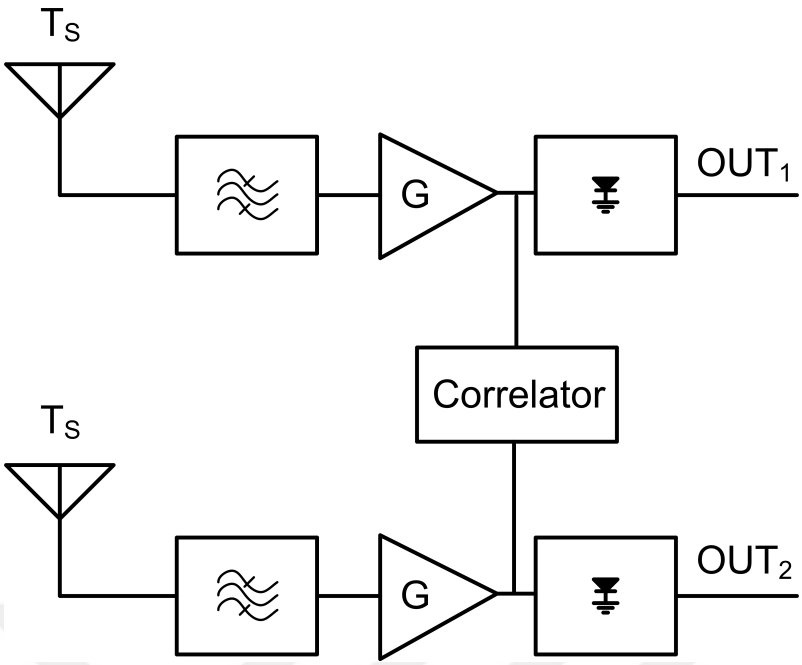

Figure 19: Block diagram of the correlation radiometer

system, two identical total power radiometers are connected to identical but separate antennas observing the same scene. The output of the LNAs are separated into real and imaginary signals of the cross correlation through a correlator [46]. Since the noise of the receivers are uncorrelated but the signal power is highly correlated, the output signal represents the received signal power [47]. The corresponding NETD of the CR improves by a factor of $\sqrt{2}$ compared to TPR.

There other architectures that improve the sensitivity of the radiometer by various techniques based on TPR or Dicke radiometer. Using multiple calibration sources or varying duty cycle for switching period can be used to improve NETD to some extent. Nevertheless, almost all of them operates on the basic principles presented in this section.

2.4 Radiometric Imaging

The quality of the radiometric image obtained from the system depends on not only the temporal resolution of the system but also the spatial resolution which is related with the antenna aperture half power beamwidth. Also, the imaging method varies depending on the application, i.e. whether it is airborne, space-borne or ground based application. An example of a ground based application is concealed

weapon detection and the image output of a 90 GHz radiometer of a person with concealed weapons standing in 2.5 m distance from the system is illustrated in Fig. 20. Such images can be generated after processing the output signal of the radiometer given that the system sensitivity is sufficient in terms of temporal and spatial resolutions.

In general, there are multiple ways of composing an image based on radiometric measurement data. First is the mechanical scanning method. A single pixel can be scanned along an axis or multiple axes and at each point of measurement, the output data is stored along with the corresponding coordinates. After the scan is completed, the output data which is usually an ADC count after the baseband operation is complete, can be mapped into a 2D plane using the data coordinates. The corresponding ADC count can also be mapped into a gray scale in which a zero count means black and a maximum count is white. Same approach can be utilized even if the system has multiple receivers/pixels and the only difference is that mechanical scanning takes less time. Second is the synthetic apertures that use multiple antenna arrays in single axes. In this scheme, both the amplitude and phase information of the detected signal is measured and correlated to construct an image. Lastly, focal plane arrays (FPA) is another method to obtain an image in which multiple antennas are configured in a 2 dimensional array with a fixed distance which is determined by the wavelength and the spatial resolution required. The field of view of the FPA can be adjusted using additional optics as shown in Fig. 21. Multiple receivers can also be placed along with the antennas or can be placed separately if the feedlines are long enough. The principle is same with mechanical scanning in FPA systems; radiometric measurements of the multiple receivers are processed and mapped into the image. The advantage of an FPA system is that usually no mechanical scanning is required which lowers the cost and complexity of the systems.



Figure 20: Concealed weapon detection using a 90 GHz radiometer [12]

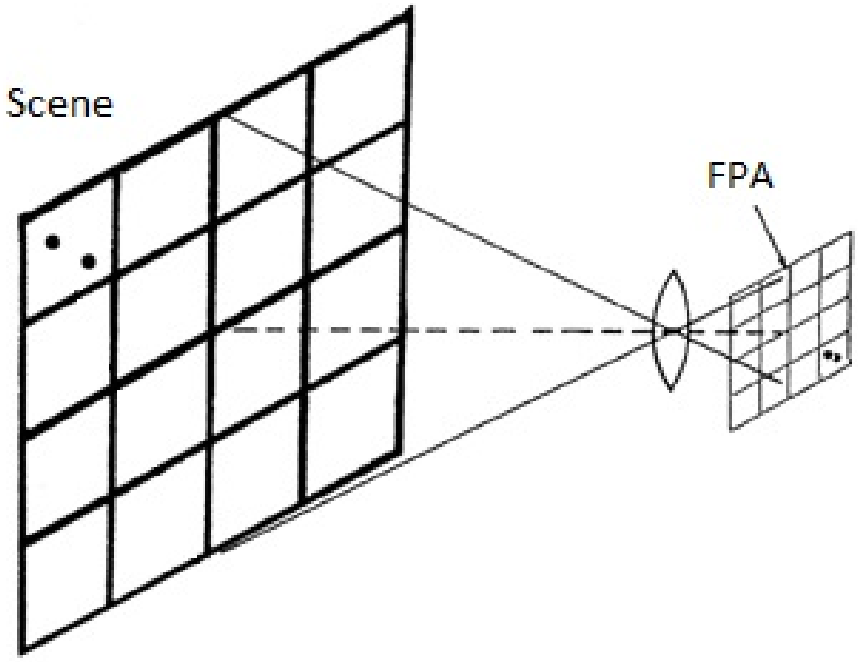

Figure 21: Illustration of an FPA with additional optics and the corresponding image mapping

3 W-Band Radiometer Design in SiGe BiCMOS

In this chapter, the design methodoloy and experimental results of the sub-blocks of the TPR and Dicke radiometer which are shown in Fig. 22 are presented. Comparison with the state-of-the-art (SoA) is highlighted for each block. Also, the proposed dual receiver Dicke radiometer topology is discussed in detail. The implementation of TPR, Dicke and dual receiver systems are presented and achievable sensitivity for these systems are analyzed.

3.1 Sub-Block Designs

3.1.1 Power Detector

It is good practice to start the design of the radiometer from the power detector because the noise equivalent power (NEP) of the detector is mostly determined by the technology and the rest of the stages have to be designed accordingly so the noise is surpassed. The schematic of the power detector (PD) is shown in Fig. 23. When an input signal is applied, a second order DC response is generated by the input transistor (Q1) and the first order response is cancelled by the 500 fF capacitor at the collector. The output transistor (Q2) acts as a current buffer and the DC current is reflected on to the load resistor which creates a DC voltage difference proportional to the input power.

The detector is implemented in a cascode like configuration. Single ended design instead of differential is chosen for a compact layout. Even though the output noise is increased by Q2 by a relatively insignificant amount, any large load present at the output could potentially introduce undesired parasitic inductance and capacitance

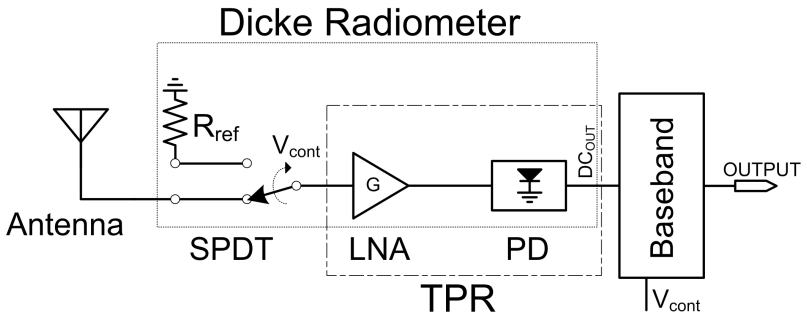

Figure 22: Block diagram of the TPR and Dicke radiometers

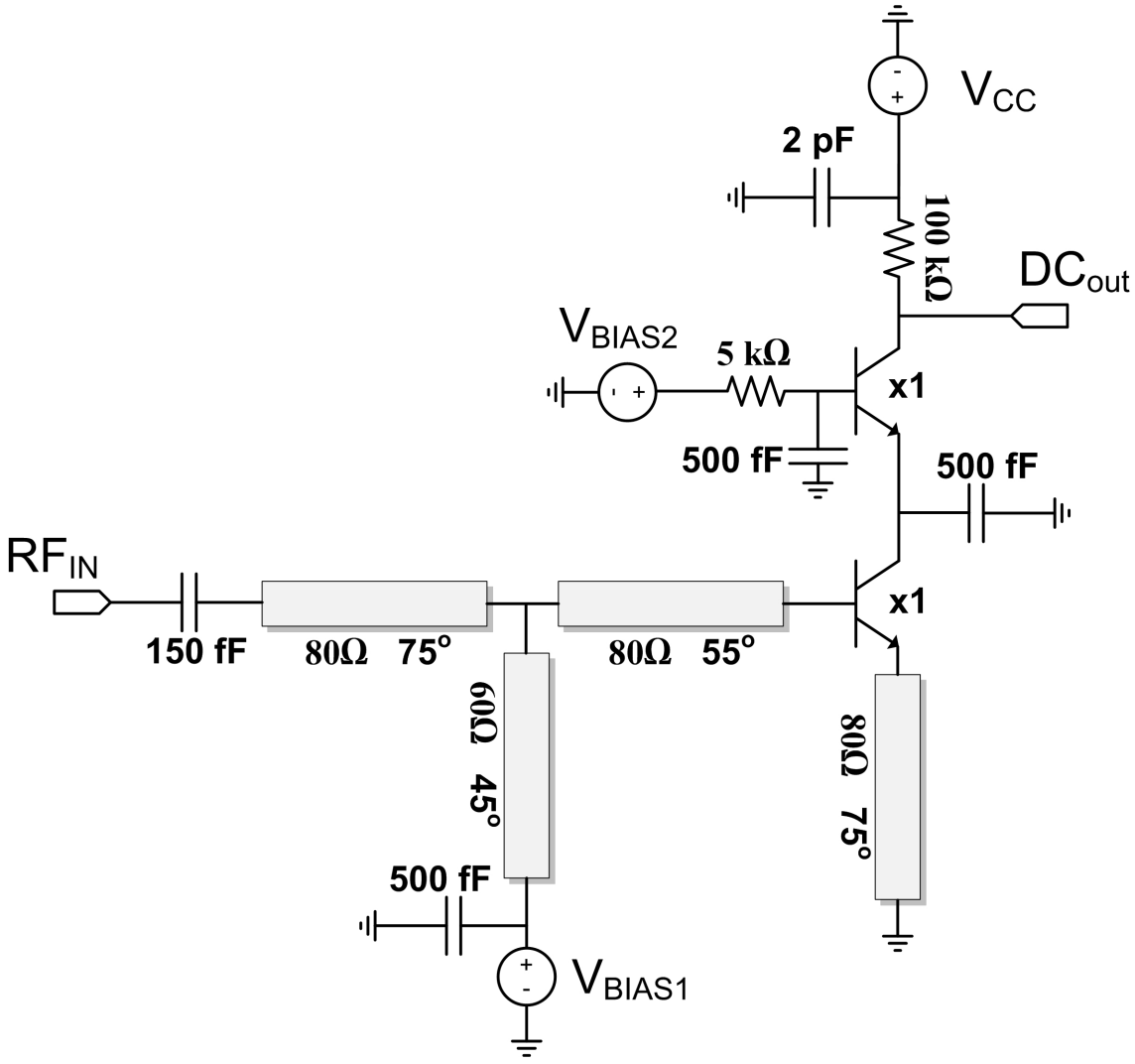

Figure 23: The schematic of the W-Band Power Detector

that would impact the input matching, consequently the responsivity of the circuit. Secondly, this buffering keeps the collector voltage of the Q1 constant therefore reducing the sensitivity of the matching with respect to the input power. Lastly; the maximum voltage drop at the output is now determined by the BV_{CEO} of Q2 instead of Q1. It is shown that a SiGe HBT biased with a forced emitter current could have BVCEO as high as the twice of the nominal value [48]. If needed, this effect could increase the maximum detectable input power depending on the responsivity. However, since the received power by the antenna is expected to be around -80 dBm, the input power to detector would be -60 to -50 dBm depending on the gain of the LNA which is low enough not to compress the detector.

The two most significant performance parameters of the PD, NEP and responsivity, are related as

$$NEP = \frac{v_n}{\beta} \tag{29}$$

where v_n is the RMS output noise voltage normalized to 1 Hz bandwidth and β is the responsivity. The load resistor, bias point and the input matching are all significant to achieve low NEP and high β.

The responsivity of the circuit is directly proportional to the load resistor, however the NEP does not directly decrease by improving responsivity since the output noise is also effected by the increased load. An analysis presented in [49], shows that increasing the load would result in lower NEP, which is expressed by (30).

$$NEP = \frac{1}{\alpha}\sqrt{\frac{q}{I_{DC}} + \frac{4kT}{I_{DC}^2 R}} \tag{30}$$

The first term inside the square root in (30) is not effected by the load resistor, whereas the second term decreases with respect to increased R_{LOAD}. The minimum NEP is achieved when the second term diminishes in the presence of a sufficiently high load. This is also verified by simulations that show R_{LOAD} of approximately 50 $k\Omega$ or higher would not improve NEP significantly whereas the responsivity is always enhanced proportional to the load, which is illustrated in Fig. 24. Also, when a high load is present at the output, V_{CC} must be increased as well to keep Q2 out of saturation. Finally, the input impedance of the following stage needs to be high, such that the responsivity and NEP do not degrade. With all these considerations in mind, the R_{LOAD} is chosen to be 100 $k\Omega$ and V_{CC} to be 5.5 V for improved responsivity and low NEP. The PD can be followed by a FET input pre-amplifier with input impedance of 1 $M\Omega$ or greater without any significant degradation in performance.

To minimize NEP, bias point and the transistor size need to be selected carefully. The non-linear behavior of the Q1 should be enhanced which would improve the second order response of the circuit. This happens with the minimum transistor size, biased at the edge of active region. This intuition is also verified by the simulation results that is presented in Fig. 25. Increasing the number of transistors from 1 to 4 nearly triples the NEP at the same bias point. The optimum bias point is also found to be 750-760 mV. The final choice of transistor size is $1x$, biased at 755 mV.

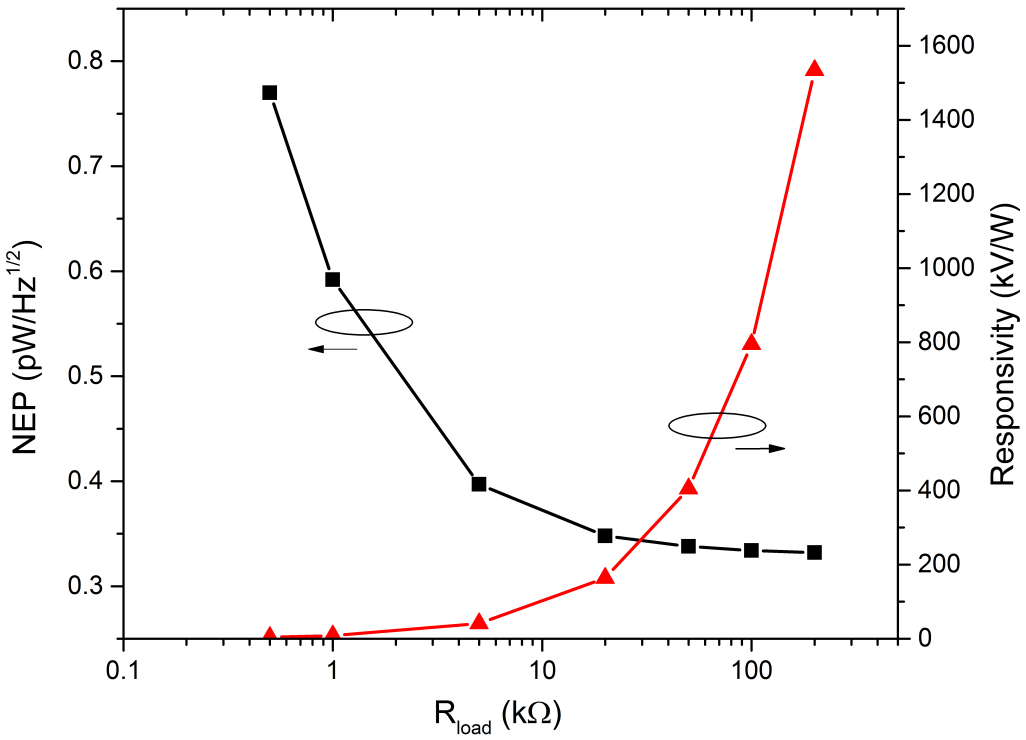

Figure 24: NEP and Responsivity vs. R_{load}

Input matching greatly effects the responsivity, consequently the NEP as well. The reflected power at the input would not be detected at all therefore the circuit needs to be matched over a wide bandwidth to keep the average NEP low over the entire W-Band. However, it is also challenging to design wideband matching with the given transistor number and bias point. Nevertheless, the use of T-type matching with high characteristic impedance transmission lines (TLs) at the base along with emitter degeneration would yield more than 20 GHz of bandwidth. The electrical length of the implemented TLs as shown in the schematic of the circuit (Fig. 23) are given at 94 GHz. The introduced loss at the input also degrades responsivity and NEP, e.g a 3 dB loss at the input halves the responsivity and doubles the NEP. As a tradeoff, wideband matching is prioritized to keep average NEP low instead of minimizing NEP as much as possible. Using the simulated NEP value of 0.28 $pW/Hz^{1/2}$ and assuming 20 GHz of bandwidth, the corresponding noise figure (NF) is calculated as

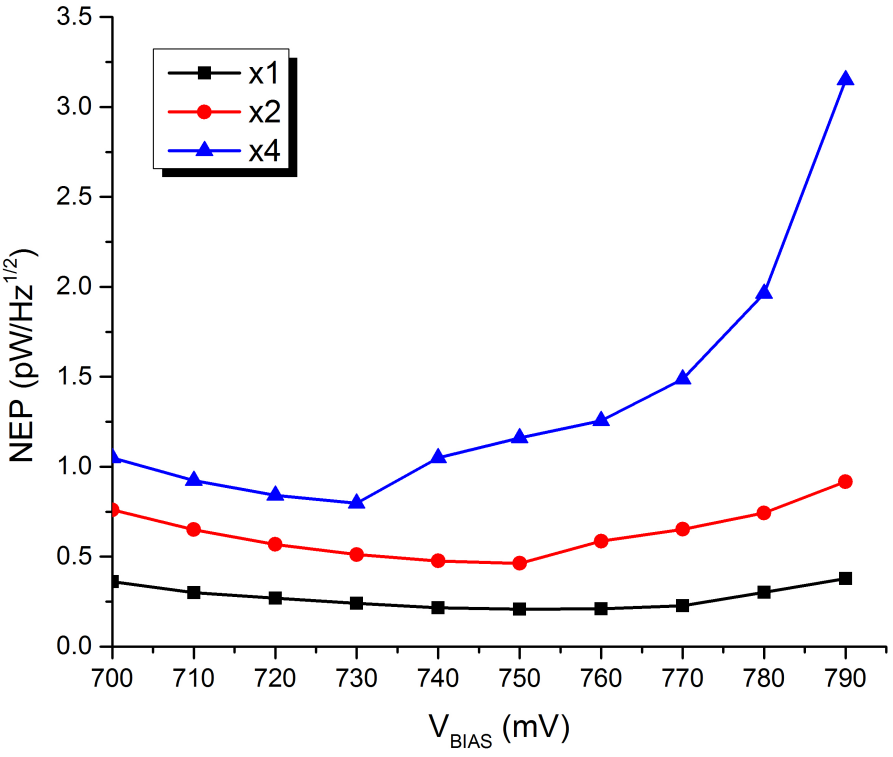

Figure 25: NEP of the Power detector vs. V_{bias} for different number of HBTs

$$NF = 1 + \frac{NEP}{kT\sqrt{B}} \tag{31}$$

which is given in [50]. The resulting NF is found to be 27 dB.

All the TLs are implemented as microstrip lines which are meandered whenever possible to keep the layout of the PD compact. 500 fF MIM capacitors with adjusted geometry such that they self-resonate close to 100 GHz are used to implement RF shorts. A 150 fF DC block capacitor is used which also facilitates matching slightly. The bias voltage is applied directly rather than over a resistor to keep the noise contribution minimal. The 13 fF parasitic capacitance due to the RF pads did not degrade the matching performance significantly, therefore it is included in the matching without any additional treatment. Full chip electromagnetic (EM) simulation is performed in ADS Momentum Microwave that incorporate all the vias as well as the capacitors, shown in Fig. 26.

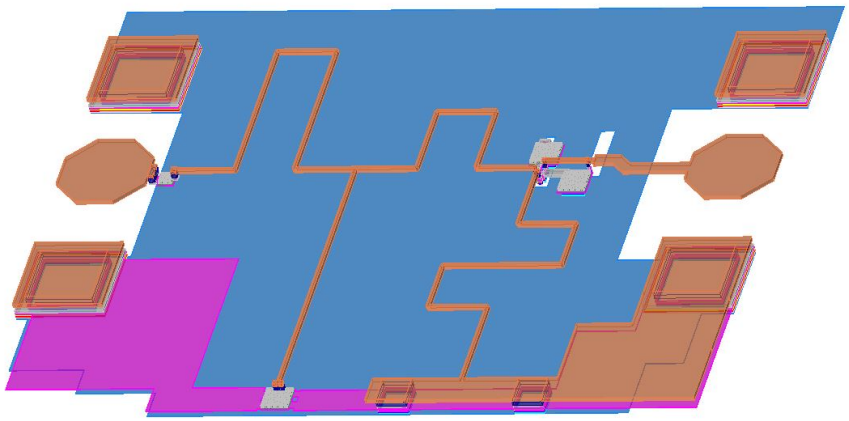

Figure 26: EM simulation setup of W-Band Power Detector in ADS Momentum

3.1.2 Low Noise Amplifier

Using (28) and simulated 27 dB NF of PD, as well as assuming 20 GHz of bandwidth, 2 dB IL for the SPDT switch, 290 K T_0, and 30 ms of integration time; the achievable NETD is analyzed for various LNA gain and NF values. Fig. 27 shows that approximately 18 dB gain and 4-5 dB NF is sufficient for NETD of <0.5 K. Even though higher gain would improve NETD even further, low power and wideband design is prioritized over high gain.

The schematic of the W-Band LNA is presented in Fig. 28. 4 stage common emitter (CE) topology is chosen as CE offers around 5-7 dB gain per stage which is sufficient to achieve 18-20 dB compared to cascode stage which would provide 3 dB more but at the expense of higher power consumption and slightly higher NF. Another reason is the low isolation of a CE stage which gives designer more degrees of freedom since output matching circuit also effects the input. As a result wideband matching at the input, output as well as at the interstages can be obtained.

First stage is optimized for minimum NF and moderate gain whereas the rest of the stages which are identical are designed for higher gain. 1.2 mA collector current (I_C) and 5x transistor size is found to be optimum for the first stage to obtain simultaneous power and noise matching. A shorted stub is placed at the input matching along with a relatively large emitter degeneration to avoid any series TLs which would increase the NF, while still allowing for a wideband input matching.

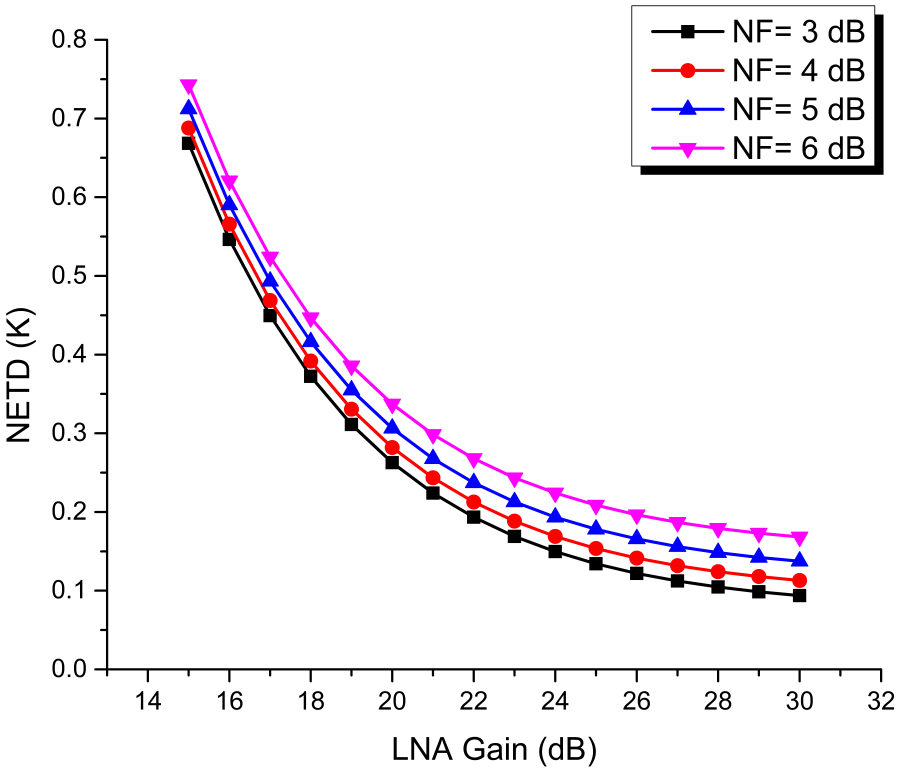

Figure 27: Calculated NETD vs. LNA gain for different NF values

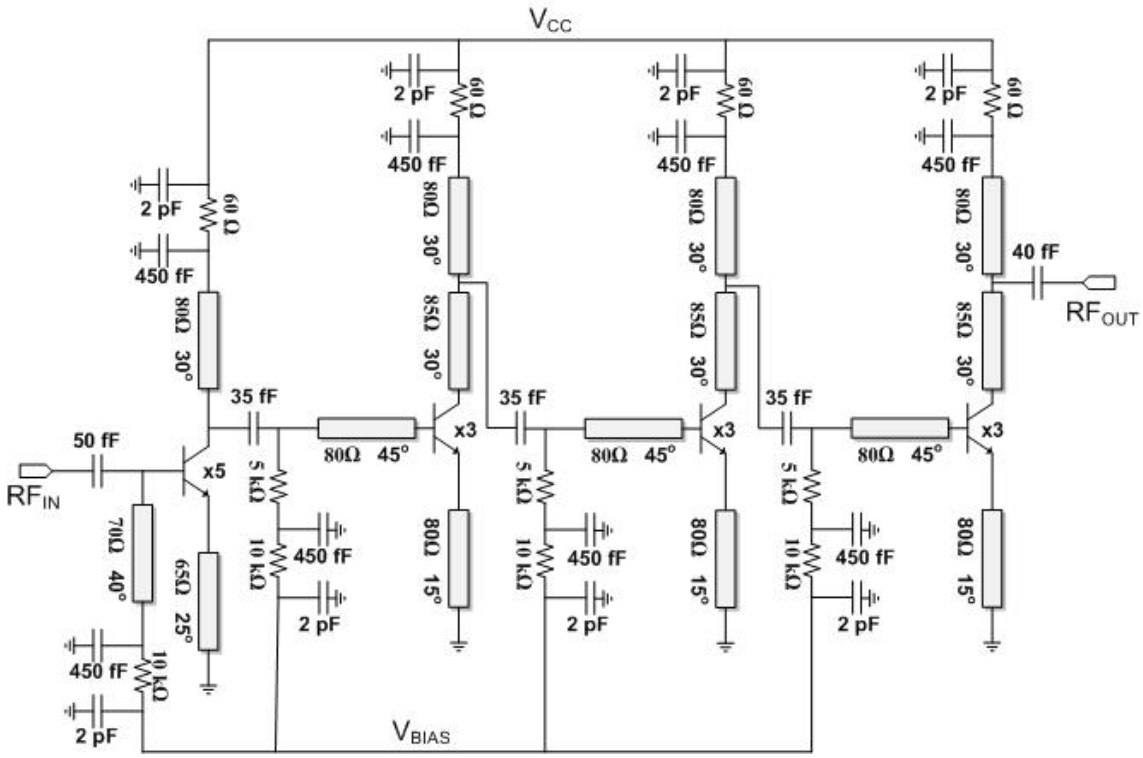

Figure 28: The schematic of the W-Band LNA

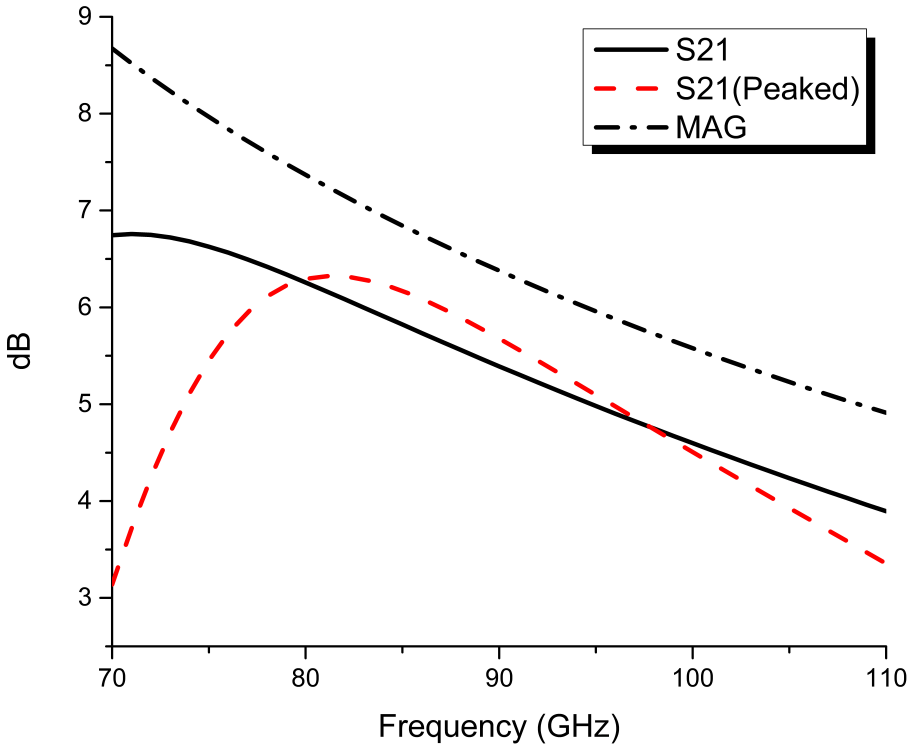

Figure 29: MAG vs. S21 curves for different loads for a CE stage

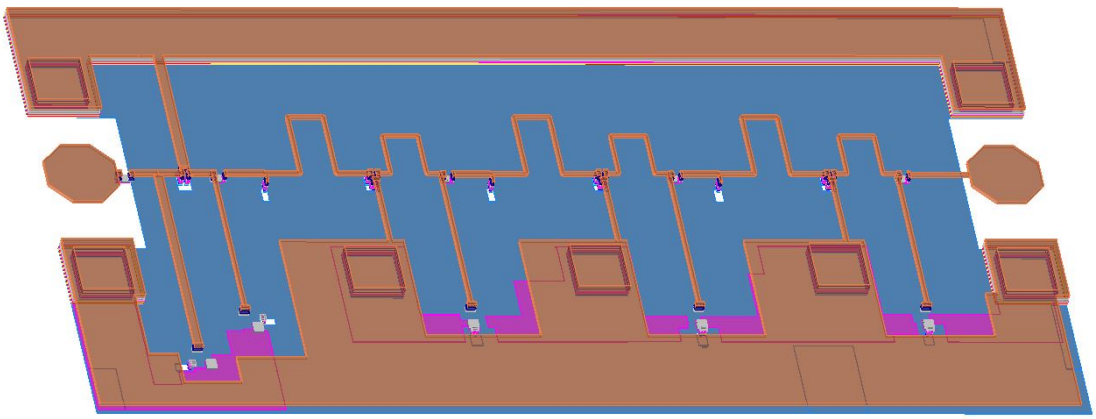

Figure 30: EM simulation setup for W-Band LNA in ADS Momentum

The 50 fF MIM capacitor is used as DC block and for matching as well. The (I_C) is set to 1.7 mA with a transistor size of $3x$ for the rest of the stages for higher current density per transistor to increase the gain. The V_{CC} is set to 1.3 V also for low power consumption and can be further reduced without any significant degradation in performance. The emitter degenerations are also reduced for the same purpose. Interstages are matched to 50 Ω using T-type matching network and

series TLs. All of the TLs are chosen with high characteristic impedance to allow for wideband interstage matchings as a tradeoff to increased loss. Also, S-Probe analysis is applied at the interstages to ensure unconditional stability such that the $\Gamma_{IN} \cdot \Gamma_{OUT}$ magnitude is <1 at all frequencies.

The type and the quality factor of the load determines the frequency at which the gain of each individual stage is peaked. Using a high-Q load, S21 can be peaked at the center of the frequency band. However this also effects the output matching of the stages such that it becomes much more narrowband compared to using a low-Q load. Even though the maximum achieved gain would be closer to the maximum available gain (MAG) curve with a high-Q load, the gain rolls off steeper when the load is out of resonance, which is shown in Fig. 29. On the contrary, tracking the MAG curve over the entire bandwidth improves the average gain, interstage matching bandwidth and consequently the effective noise bandwidth of the LNA.

Alll the TLs are implemented as MSLs and 450 fF MIM capacitors are used for RF short. 60 Ω silicide resistors are placed to improve low frequency stability. The electrical length of the implemented TLs as shown in the schematic of the circuit (Fig. 28) are given at 94 GHz. 2 pF MIM capacitors are used to bypass in addition to the bias planes placed in between two ground planes which adds several pFs to the bypass network. EM simulations are performed using ADS Momentum excluding the secondary capacitor banks and fillers which is shown in Fig. 30. All the layout work is completed using Cadence.

3.1.3 SPDT Switch

The schematic of the first version of the single-pole-double-throw (SPDT) switch is shown in Fig. 31. The circuit employs $\lambda/4$ transmission lines and shunt HBTs at the input. At high frequencies, the use of series switches are limited since the insertion loss (IL) severely degrades due to R_{on} resistance of the HBTs. Therefore only shunt switches are used which reduces the isolation between the ports but keeps the IL minimum. When V_{cont} is high, Q1 shorts the node to ground and $\lambda/4$ TL transforms it to open. The input signal is then directed to the other path.

There are two dominating loss mechanism in $\lambda/4$ SPDTs. First, is the parasitic effects associated with the HBTs. When used as a shunt switch, both the para-

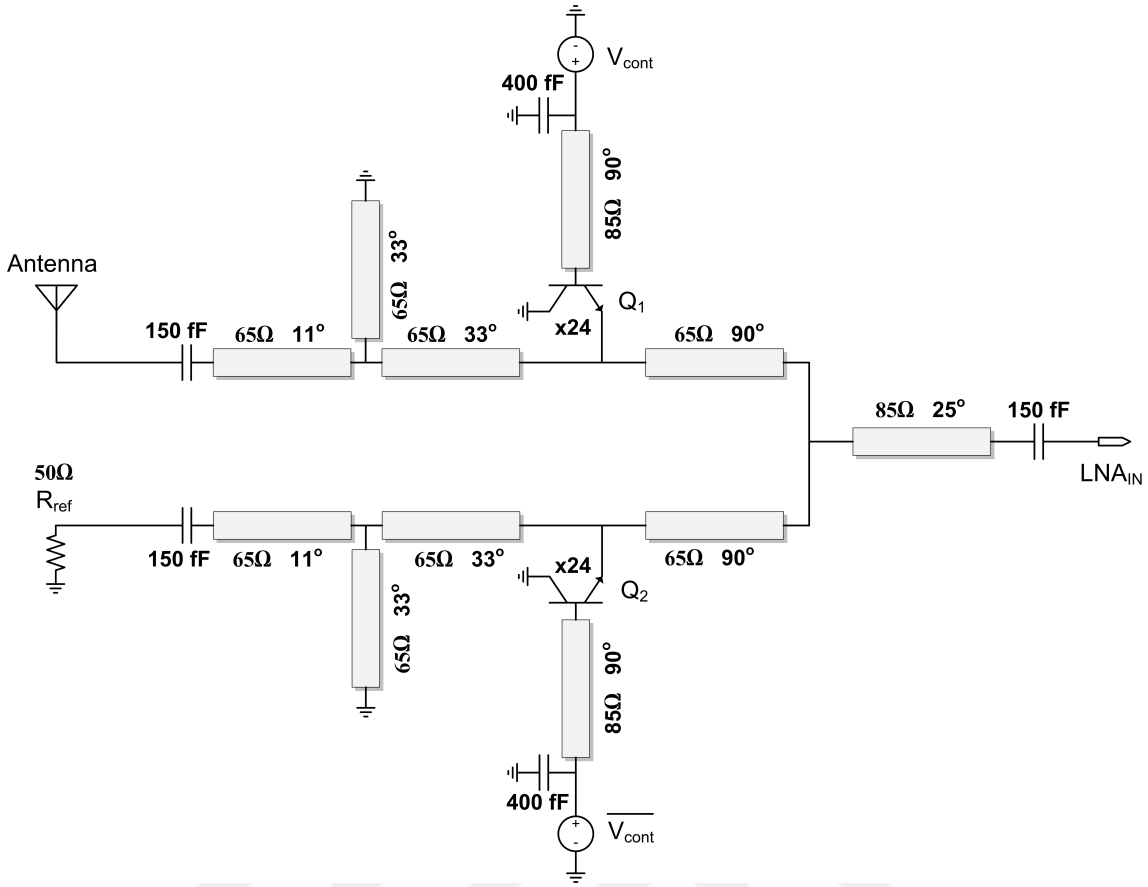

Figure 31: The schematic of the W-Band SPDT Switch (First version)

sitic resistance and the capacitance to ground, introduces additional loss as well as lowering the isolation. When several HBTs are paralleled, the parasitic resistance drops but total capacitance is then increased by the same amount which impacts IL. However, this parasitic capacitance can be left floating through the use of shorted $\lambda/4$ TL. In return, the IL improves, however, a sacrifice has to be made in terms of isolation since the floated capacitance helps the node to become short better. The IL of the SPDT is much more significant in radiometer systems to achieve low NETD, since the NF of the LNA also gets amplified by the IL of the SPDT. Consequently, all the tradeoffs that improve IL have been made. Furthermore, the shunt HBTs are used in reverse saturation mode which also reduce IL due to higher off-state resistance [51].

The other loss mechanism in SPDTs is the loss of the passive components, in this case TLs and vias. While the loss of tungsten vias cannot be avoided, the TLs can be designed such that losses are minimized. One of the methods to reduce the loss of the TLs, is the slow-wave method. In the slow-wave TLs, the wave velocity of the

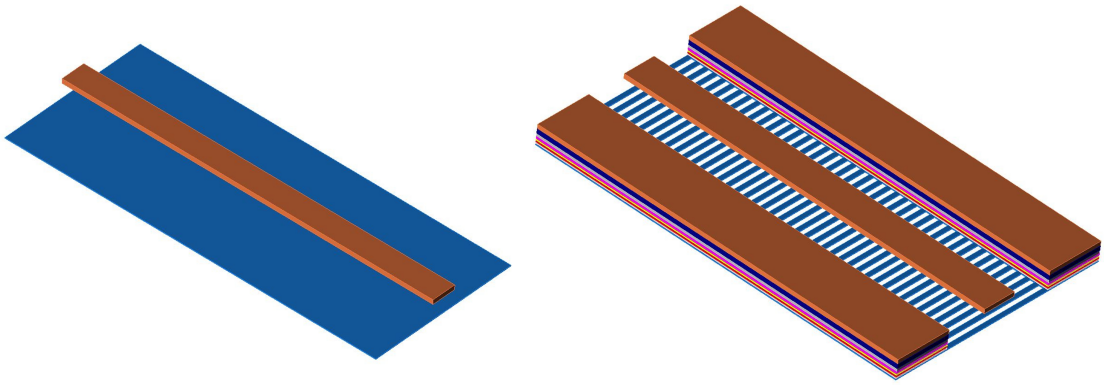

Figure 32: (a) Microstrip transmission line (b) Slow-wave Coplanar transmission line

signal is reduced due to higher effective ϵ_r between the signal line and ground plane due to the slotted nature of the ground plane. As a result, it is possible to achieve higher electrical length per physical length in slow-wave TLs [52]. This improves the quality factor of the lines and therefore lower attenuation per phase shift can be obtained using slow-wave coplanar lines (Fig. 32 (b)) compared to microstrip lines (Fig. 32 (a)). The higher effective ϵ_r also helps to keep the overall area of the chip minimum due to reduced size of the TLs.

Even though the slow-wave TLs offer higher performance and potentially lower area, the required computation time for simulation as well as the accuracy might suffer to employ slow-wave TLs. Therefore two versions of the SPDT switch shown in Fig. 31 are designed, one employing microstrip lines, and other slow-wave coplanar lines. The simulations also verify that 0.1-0.3 dB improvement in IL and 0.5 dB improvement in isolation for slow-wave version.

One of the drawbacks of using HBTs in SPDT design is the static power consumption. The base voltage can be set to 0.9 V or higher for a tradeoff between IL and power consumption. Above 1 V, the improvement in IL is less than 0.1 dB. The final choice of bias voltage is 0.95 V for a tradeoff between power consumption and IL, and the total current drawn from it is 11 mA.

The input and output of the SPDT switch are matched to 50 Ω through T-type matching network. The 25° TL at the input helps the matching achieve more than 20 GHz of bandwidth. 150 fF capacitors are used as DC block and RF shorts are implemented using 400 fF MIM capacitors. The parasitic capacitance of the RF

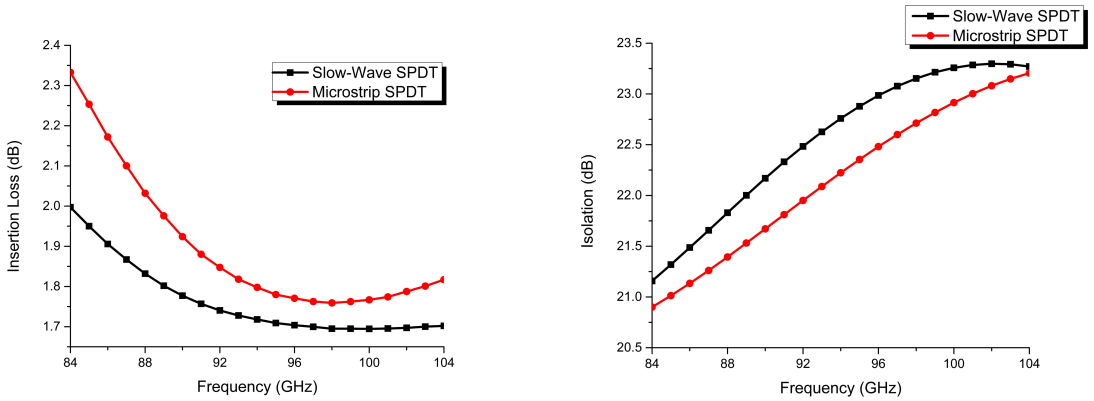

Figure 33: Simulated (a) IL and (b) isolation of the microstrip and slow-wave SPDTs

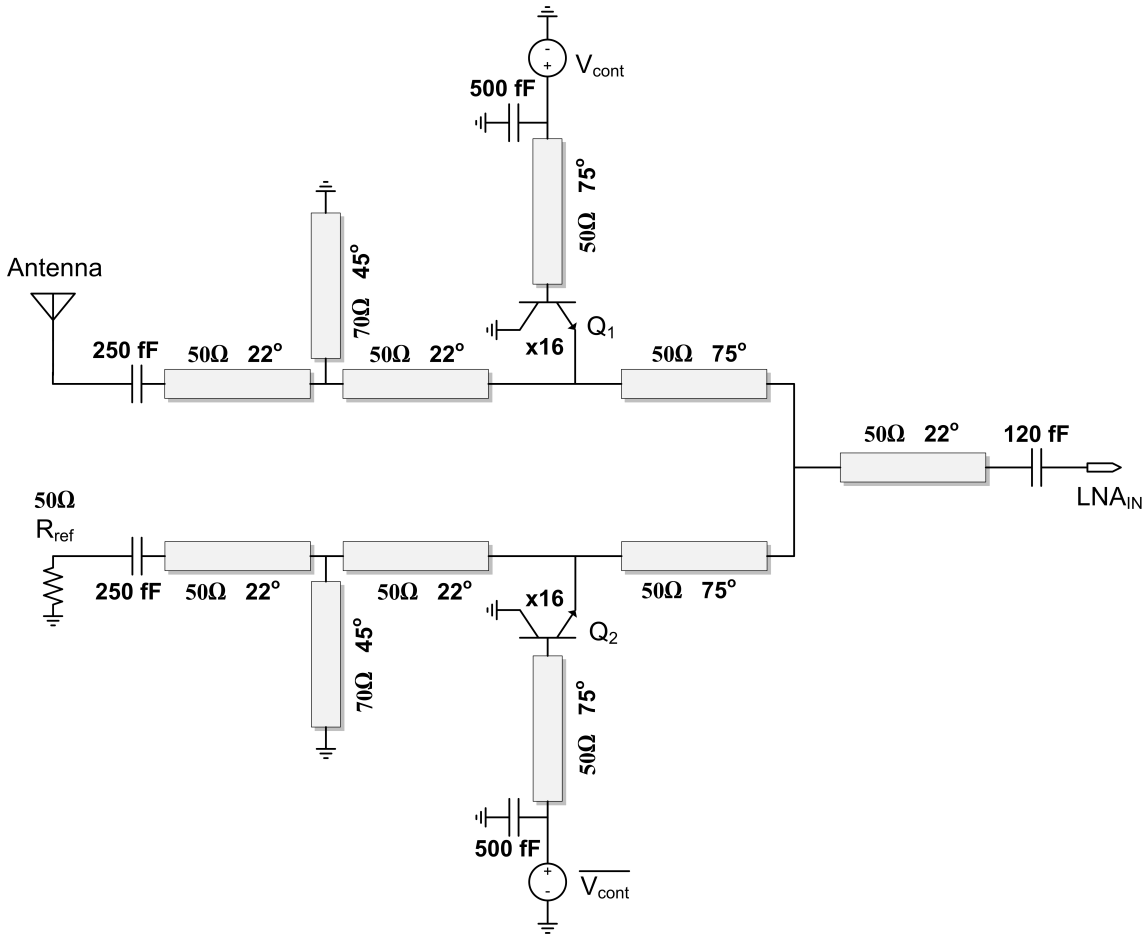

Figure 34: The schematic of the W-Band SPDT Switch (Second version)

pads are also included in the matching.

The first post layout simulations show that <2 dB and >21 dB isolation for slow-wave SPDT which is shown in Fig. 33 (a) and (b). However, after the measurements, it is observed that IL of the SPDTs have degraded significantly to 4-5 dB

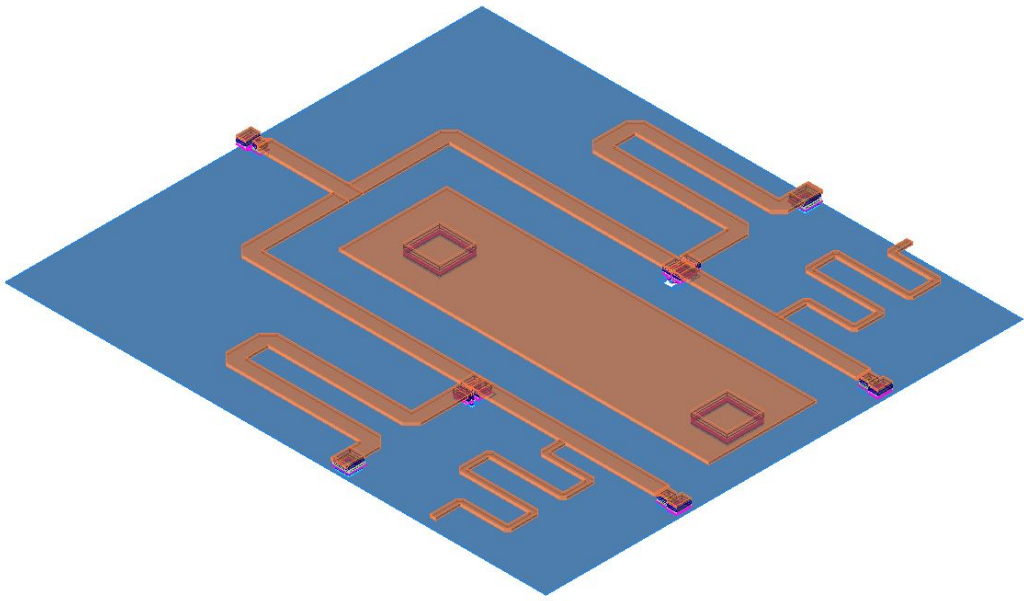

Figure 35: EM simulation setup for W-Band SPDT in ADS Momentum (Second version)

and matchings have also shifted quite considerably. Therefore, the simulations are redone, this time incorporating all the passive elements in single simulation setup. Much better agreement is achieved with the microstrip SPDT than the slow-wave version which also shows the degradation in performance to some extent. Consequently, a new SPDT is designed utilizing microstip TLs and the results are verified by full-chip EM simulation.

Fig. 34 presents the schematic of the newer SPDT switch. Similar to previous versions, T-type matching is utilized as well as the reverse saturated HBTs. The number of HBTs is reduced to $16x$ to achieve wideband input and output matching. The wideband matching also keeps the IL from overshooting due to mismatch at the edge of specified frequency band. Therefore, the input and output are matched to 50 Ω from 75 to 110 GHz. The fewer number of transistor also reduces the power consumption to almost half the value that of previous versions. The TL sizing also slightly adjusted to optimize IL and isolation over the bandwidth.The electrical length of the implemented TLs as shown in the schematic of the circuit (Fig. 31-34) are given at 94 GHz. Full chip EM simulation is performed to achieve greater agreement between simulation and measurement (Fig. 35). Pads are not included in the matching in this version to implement this SPDT in the complete

radiometer system.

3.1.4 Antenna

The antenna is designed to match the wideband specifications of the rest of the circuit. For this reason a bow-tie antenna is implemented utilizing the LBE process for improved efficiency. The radiation efficiency of on-chip antennas is severely degraded by the dielectric constant and conductivity of the silicon backside, as well as the conductor losses. Conductor loss cannot be avoided, however, advanced processes such as LBE are highly suitable for the implementation of on-chip antennas which removes the lossy silicon backside from the chip. The removed backside enhances the radiation efficiency, hence the performance of the on-chip antennas can become comparable to that of off-chip planar antennas.

The antenna layout is presented in Fig.36. The width of the antenna is set to be 1 mm which is slightly higher than $\lambda/2$ at 90 GHz to improve efficiency at lower frequencies. The distance between each arm is 2 μm and the maximum length of the arm is 0.7 mm. TopMetal2 is used for the arms due to its higher thickness compared to other metals. Differential to single ended conversion is done using an LC balun with 83 pH inductor and 55 fF capacitor. To facilitate matching, slightly lower impedance MSL (40Ω 70°) is used before the RF pad. It is also useful to have a rather long feedline to place the antenna further away from the receiver front-end to minimize coupling effects.

One of the limitations of designing on-chip antennas is the relatively strict DRC rules. Therefore, complying with the DRC rules while still achieving sufficient performance is challenging. First, the process only allows for 45° bends, therefore to get the desired angle, the edges are implemented as staircase. Although this reduces the efficiency, it is necessary for the wideband requirements. The perimeter of the antenna is filled with Metal1-5. Also TopMeal2 and TopMetal1 are used near the RF pad for density rules.The backside of the arms cannot be etched completely due to maximum area restrictions, therefore 100 μm separation is left between etched areas. Similarly, around 200 μm space is left between the edge of the chip and the LBE areas for DRC rules.

The first set of simulations are completed in ADS Momentum. After the mea-

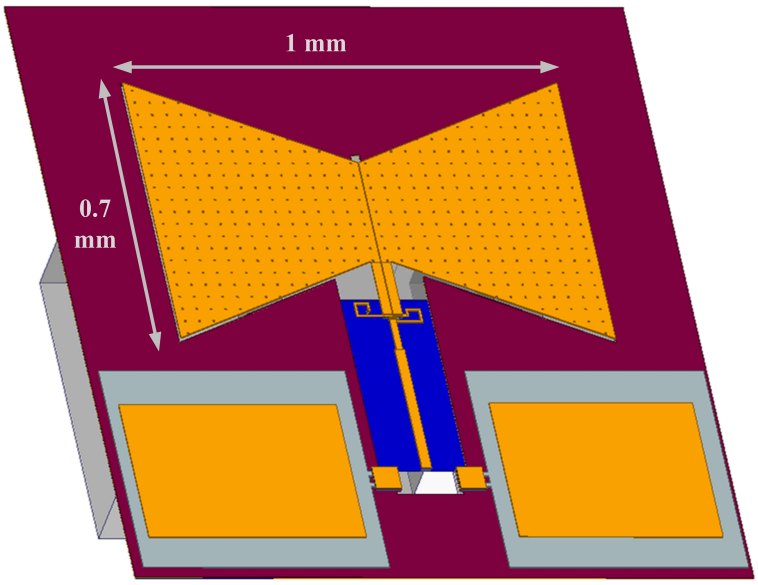

Figure 36: EM simulation setup for W-Band antenna in HFSS

surements same simulations have been performed using HFSS for better agreement between simulation and measurements.

3.2 Simulation and Measurement Results of the Sub-Blocks

3.2.1 Power Detector

The power detector is fabricated in IHPs 0.13 μm SiGe BiCMOS process. Micrograph of the chip is shown in Fig. 37. The W-Band PD occupies 0.35 mm^2 (0.54 x 0.65 mm) of area including the RF and DC pads. the chip consume less than 150 μW of power from 5.5 V supply. 755 mV of bias voltage is applied to the base of the input transistor and the output transistor is biased with 2.3 V.

S-parameters are measured on wafer in IHP's facilities using separate setups for W-Band PD. S-Parameter measurement results are illustrated in Fig 38. The measurements were made using a 0-110 GHz setup with frequency extenders and 100 μm GSG probes. Excellent agreement between simulation and measurement is observed. Input return loss of the chip remains below -10 dB from 80 to 108 GHz. This result is also important to show that full-chip EM simulations are sufficiently accurate at W-Band.

The simulation results of the responsivity and NEP of the detector are shown in Fig. 39-41. The responsivity is calculated using the harmonic balance simulation

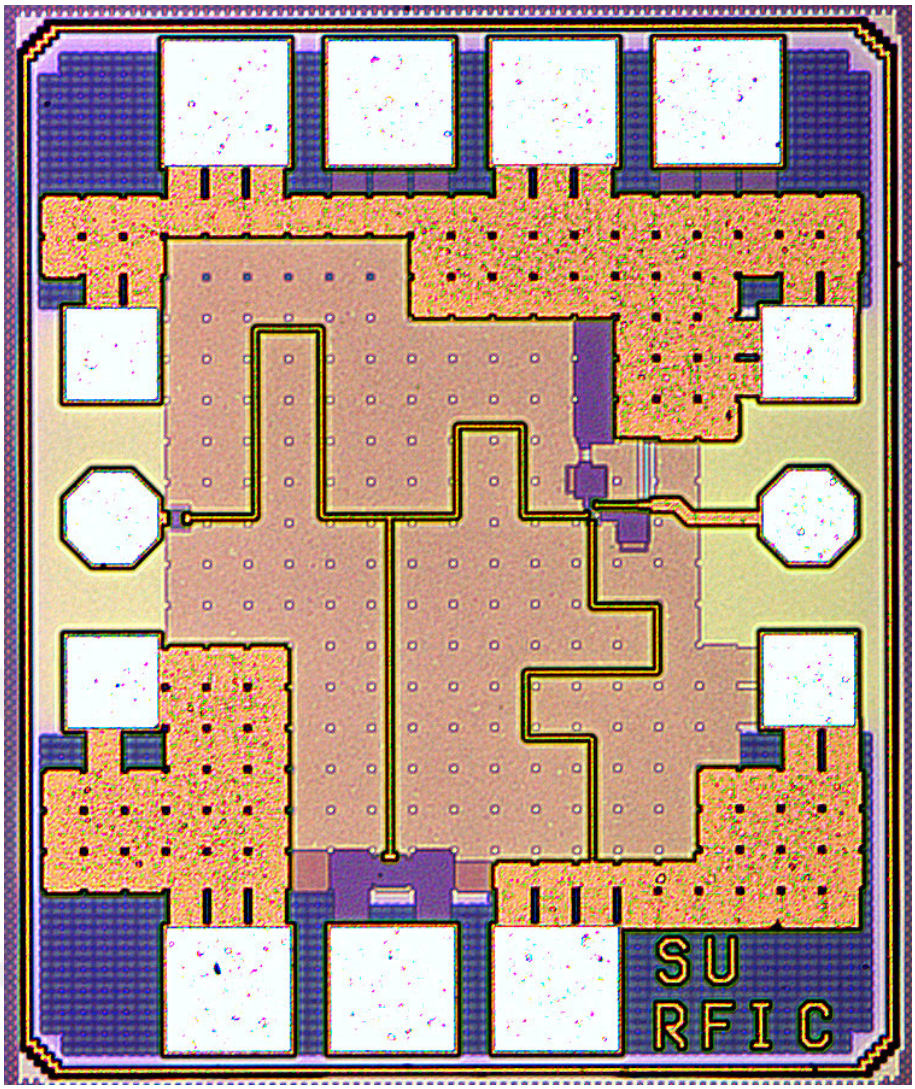

Figure 37: Micrograph of the W-Band Power Detector

results. From Fig. 39 it can be seen that, the logarithm of the output DC voltage difference ($DC_{P_{IN}=0} - DC_{P_{IN}}$) is linear with respect to the input power in dBm up to -25 dBm which is high enough for the targeted radiometer specifications. The slope of the curve gives the desired responsivity value in which the peak value is found out to be 960 kV/W at approximately 90 GHz. The NEP is calculated through the transient noise simulations. The rms noise voltage at 1 kHz at 1 Hz bandwidth is 265 $nV/Hz^{1/2}$ and the $1/f$ noise corner is below 10 Hz. The resulting NEP and responsivity values are calculated at 10 GHz frequency steps. The results are illustrated in Fig. 41.

The minimum NEP of the W-Band is simulated to be 0.28 $pW/Hz^{1/2}$ and the responsivity peaks at the same frequency, 85 GHz, with a value of 960 kV/W. Thanks to the wideband matching of the detector, NEP remains below 0.7 between

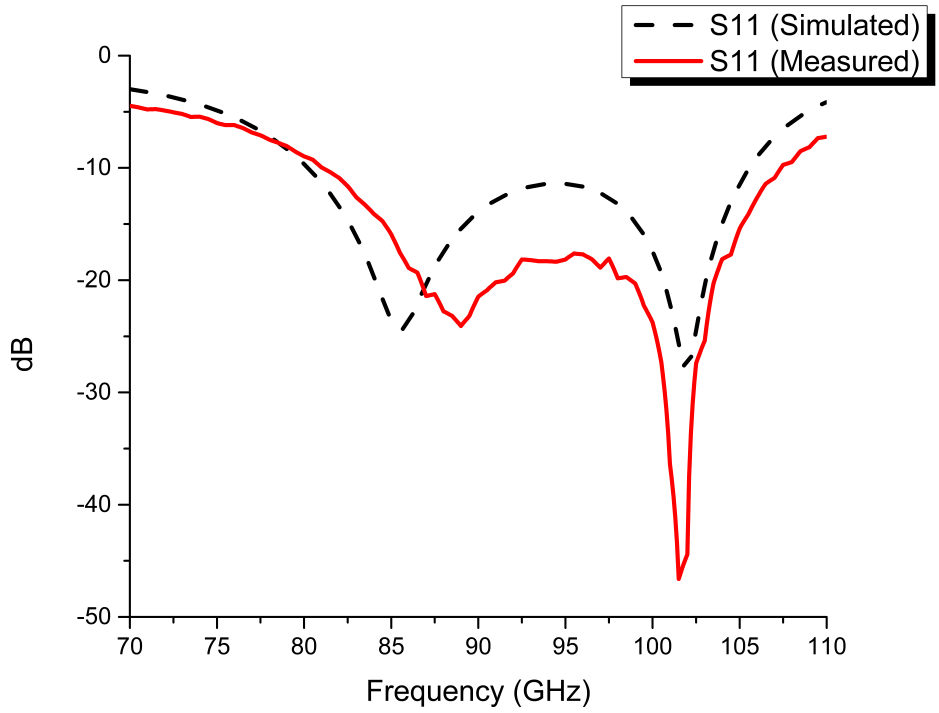

Figure 38: Simulated and measured S11 of the W-Band Power Detector

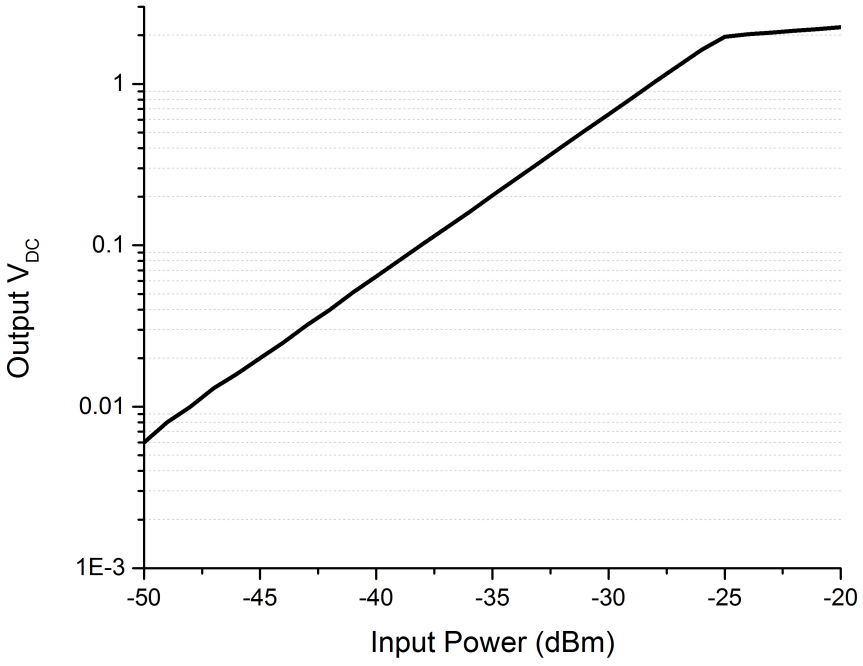

Figure 39: Simulated V_{OUT} difference vs P_{IN} of the W-Band Power Detector at 94 GHz

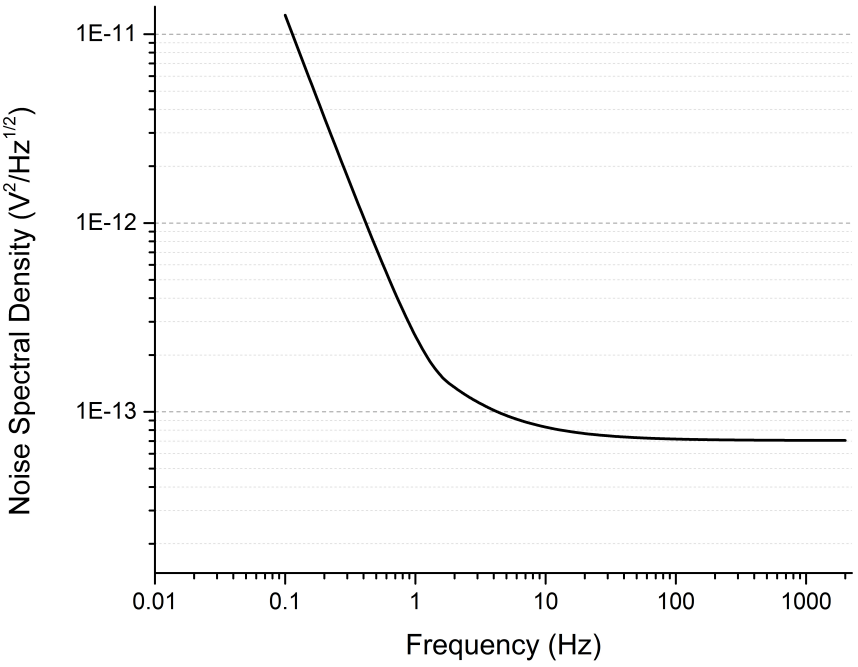

Figure 40: Simulated output noise power spectrum of the W-Band Power Detector

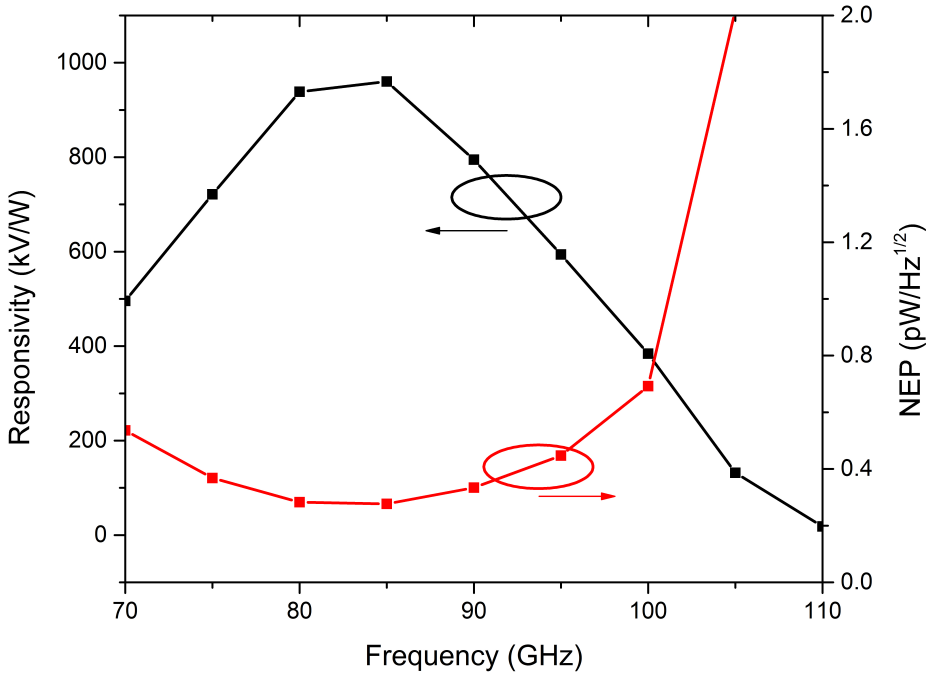

Figure 41: Simulated responsivity and NEP vs frequency of the W-Band Power Detector

Table 4: Summary of performance of the W-Band PD and comparison with the SoA SiGe PDs

	Tech.	NEP ($pW/Hz^{1/2}$)	Resp. (kV/W)	R_{LOAD} ($k\Omega$)	S11 <-10dB @ (GHz)	Area (mm^2)
[49]	0.18 μm SiGe	0.5	91	23	90-100	0.43
[53]	0.13 μm SiGe	0.4	80	10	85-92	N/A
[54]	0.12 μm SiGe	3	12	0.75	88-98	N/A
This Work	**0.13 μm SiGe**	**0.28**	**960**	**100**	**80-108**	**0.35**

70-100 GHz for the W-Band. The resulting overshoot in NEP at 110 GHz is because the matching at that frequency is only -2 dB, hence the responsivity drops considerably, and consequently NEP increases. It is also useful to calculate the corresponding noise figure (NF) of the detectors based on measurement results. Using the equation (31), and assuming 20 GHz of bandwidth for the W-Band, the NF of the detector is calculated to be 27 dB. Table 4 presents the performance of the PD in comparison with other SiGe power detectors at W-Band.

The designed detector achieves one of the lowest NEP values in the recent literature thanks to the high f_t transistors and the careful choice of load resistor and bias voltage. Also it is important to note that the matching bandwidth of the detector is much higher which makes it suitable for wideband radiometer systems.

3.2.2 Low Noise Amplifier

The W-Band LNA is fabricated in IHPs 0.13 μm SiGe BiCMOS process. Micrograph of the chip is shown in Fig. 42. The W-Band LNA occupies 0.6 mm^2 (0.85 x 0.7 mm) of area including pads and consumes only 8 mW of power from a 1.3 V supply.

W-Band S-parameter measurements were made using a 0-110 GHz setup with frequency extenders and 100 μm GSG probes. Measurement results are illustrated in Fig. 43-44. Measured peak gain of the W-Band LNA is 22.5 dB at 73 GHz and drops to 10 dB at 110 GHz and in very good agreement with simulation results. Average gain of the LNA is 17.5 dB. Also, the input and output return losses remain below -10 dB from 75 to 110 GHz.

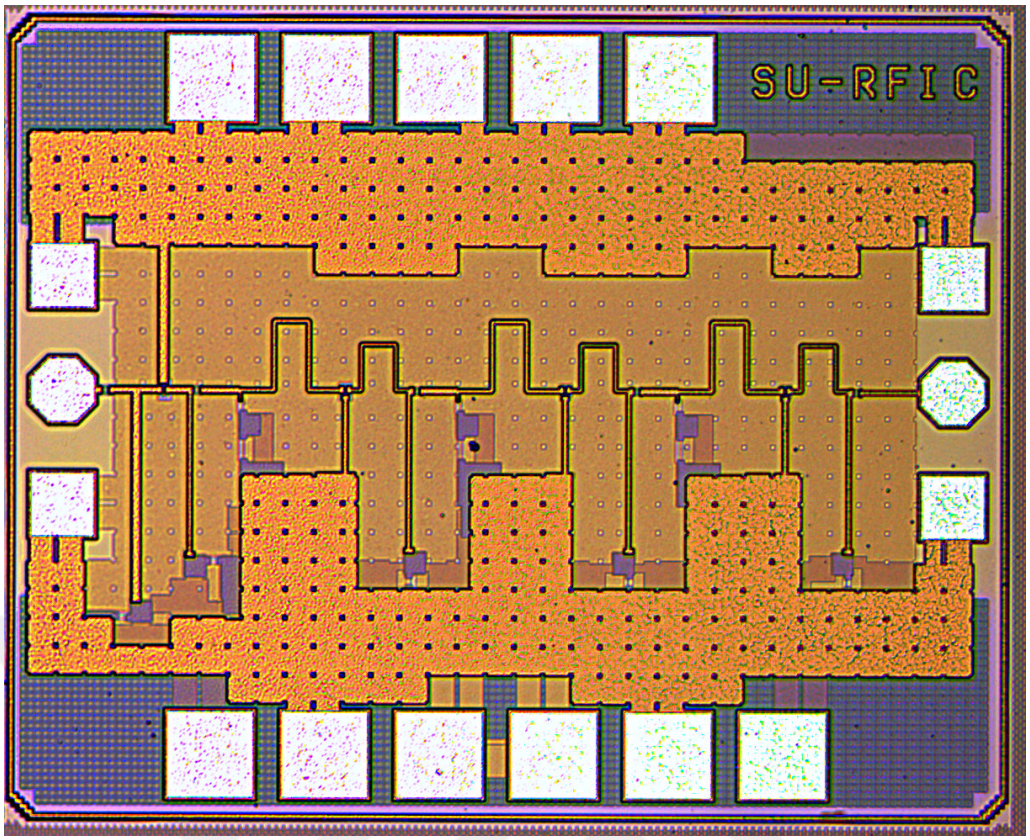

Figure 42: Micrograph of the W-Band LNA

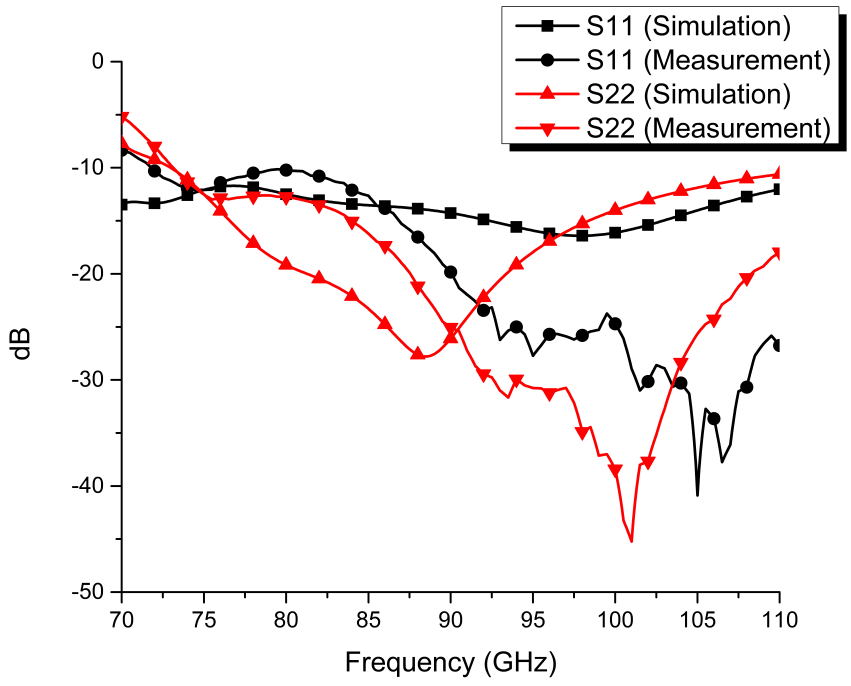

Figure 43: Simulated and measured input and output return loss of the W-Band LNA

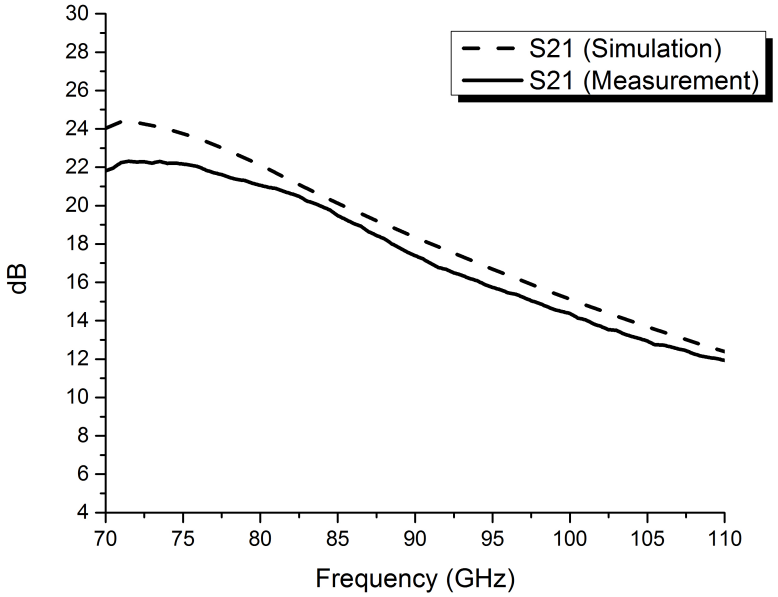

Figure 44: Simulated and measured gain of the W-Band LNA

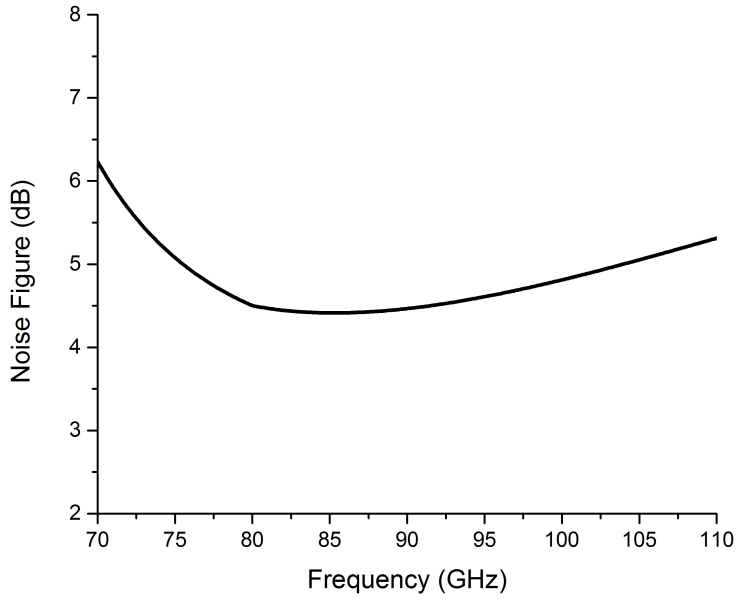

Figure 45: Simulated noise figure of the W-Band LNA

The noise figure simulation result is shown in Fig. 45. Minimum NF of the W-Band LNA is 4.5 dB and is better than 5.5 dB from 72 to 110 GHz. Input P_{1dB} of the LNA is simulated to be approximately -30 dBm.

It is worthwhile to calculate the effective noise bandwidth (ENB) of the LNA to assess its viability in a radiometer system. Using the measurement results and the

Table 5: Summary of performance of the W-Band LNA and comparison with the SoA SiGe LNAs

	Tech.	Topology	3-dB BW (GHz)	Peak Gain (dB)	NF (dB)	P_{DC} (mW)	Area (mm^2)
[57]	90 nm SiGe	5x CE	66-84	34.5	4	15.6	0.3
[54]	0.12 μm SiGe	5x CE	82-100	27	7	27.6	0.26
[58]	0.18 μm SiGe	5x CE	70-97	19	8.5	35	1*
This Work	**0.13 μm SiGe**	**4x CE**	**68-85**	**22.5**	**4.5**	**8**	0.6

**including pads*

expression

$$ENB = \frac{\left[\int_0^\infty G(f)df\right]^2}{\int_0^\infty G(f)^2 df} \tag{32}$$

given in [55], [56]; the ENB of the W-Band LNA is found out to be 35 GHz. Table 5 illustrates the performance of the LNA in comparison with the recent publications.

The designed LNA achieves sufficient gain for NETD below 0.5 K with only 8 mW of power consumption which is highly competitive to similar SiGe LNAs. The effective bandwidth of the LNA also has a considerable effect on the system sensitivity. The measurement results confirm that the LNA is suitable for the proposed radiometer systems.

3.2.3 SPDT Switch

The first version of the SPDT switches are fabricated and S-parameters are measured on-wafer in IHP's facilities. 100 μm pitch GSG probes were used at the RF ports and DC needles were used to bias the circuit. To avoid the use of GSGSG probes, one of the ports is terminated to 50 Ω on-chip so only one port is available for measurement. To measure IL and isolation, two set of biases are applied; 0.95 V at V_{bias1} and 0 V at V_{bias2} for IL and vice versa for isolation. To observe the effect of bias voltage on the IL and isolation, same procedure is repeated using bias voltage of 0.85 V to 1 V with 50 mV steps. Fig. 46 presents the fabricated first version microstrip and slow-wave SPDT switches. Microstrip version occupies 0.43 mm^2 (0.55 x 0.78 mm) and slow-wave version occupies 0.32 mm^2 (0.43 x 0.74 mm)

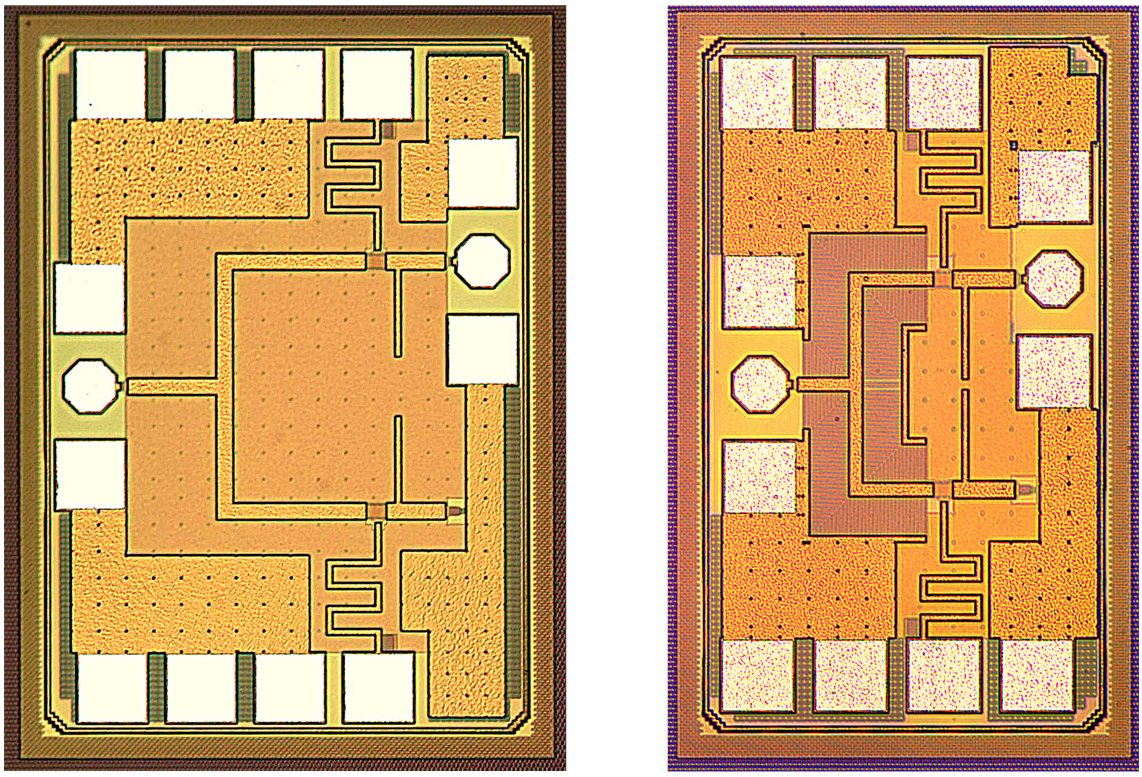

Figure 46: Micrograph of the first version (a) microstrip and (b) slow-wave W-Band SPDT switch

due to shorter quarter wave TLs, both including pads.

The S-Parameter measurement results are illustrated from Fig. 47 to 49. Due to significant discrepancy between post-layout simulation and measurement results, the MS SPDT is simulated again including all the parasitic and coupling effects and compared to the measured results. The new simulation results show much better agreement with the measurements. The input matching of the MS SPDT is shifted by 5 GHz to approximately 95 GHz. The output matching is deteriorated significantly and is better than -10 dB only at 95 to 105 GHz. The input and output matchings of the slow-wave version are much worse compared to old simulation results and the MS SPDT. The reason for this can be attributed to the lack of accuracy in the simulation of slow-wave TLs. The IL of the chips also much higher than older simulation results. Even though the new simulations predict around 1 dB increase in IL, the measured IL of the MS SPDT is higher than 3.5 dB and 1 dB higher than new simulation results. The increase in IL is due to lower β of the HBTs, the high contact loss between the probe and RF pads (estimated to be around

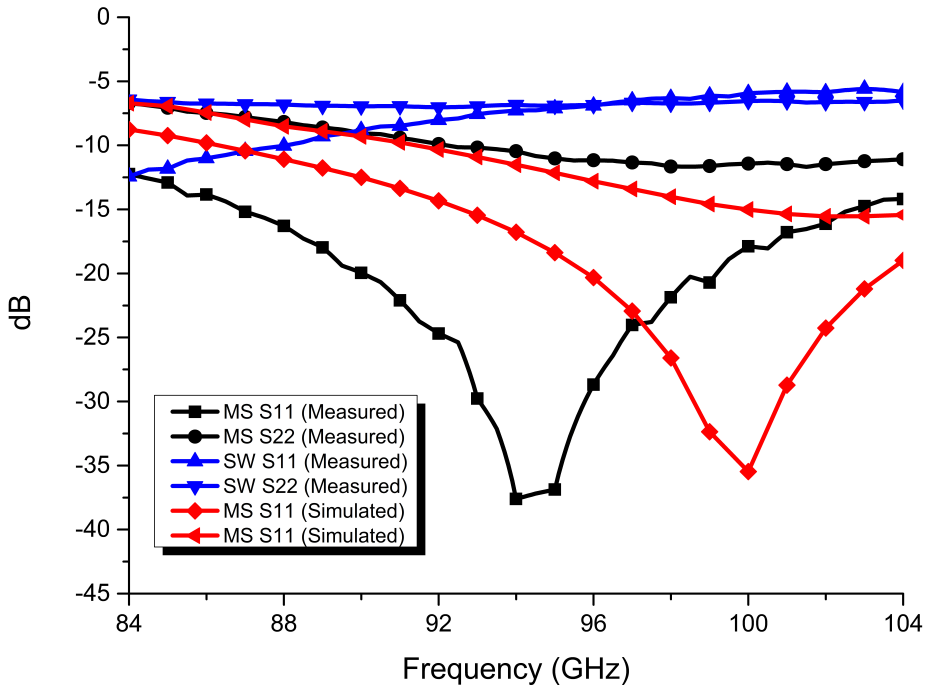

Figure 47: The simulation and measurement results of input and output return loss of the first version W-Band SPDT switch

0.3 dB total) and underestimated via losses. The slow-wave SPDT is measured to have 5-5.5 dB IL, because of the insufficient matching which results in increased IL. The isolation of the switches are better than 22 dB from 84-104 GHz and is well captured by the simulations.

The IL and isolation of the SPDTs at different bias voltages are shown in Fig. 50 to Fig. 51. At 0.85 V bias, the switches draw 0.3 mA of current (P_{DC} of 0.26 mW), 1.2 mA at 0.9 V (P_{DC} of 1.08 mW), 3.9 mA at 0.95 V (P_{DC} of 3.7 mW) and 9.1 mA at 1 V (P_{DC} of 9.1 mW). This result shows that the β of the HBTs are %20 lower than simulated. The IL improves by 0.1-0.2 dB and isolation improves by around 1-2 dB per 50 mV increase in bias voltage which is in line with simulations. However, after 0.9 to 0.95 V the improvement is minimal and power consumption increases dramatically.

The measurement results indicates that the performance of both of the SPDTs are not sufficient and that the room for improvement is relatively large. As a result, a new SPDT is designed using microstrip lines due to the fact that simulation results are much closer to measurement than slow-wave. The micrograph of the new SPDT

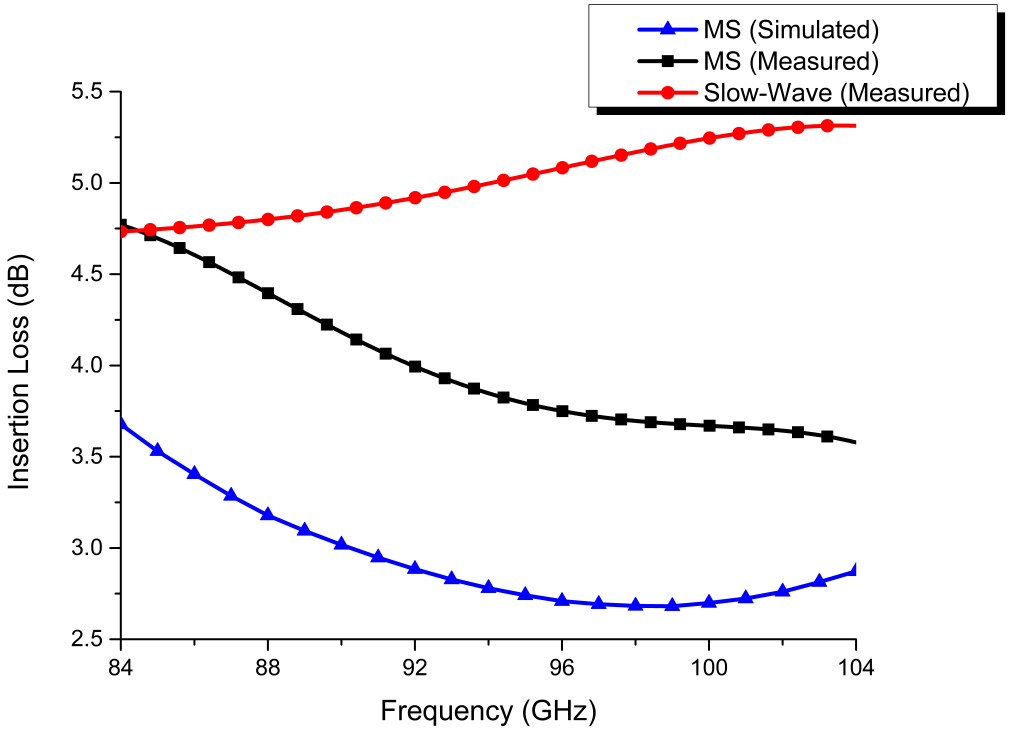

Figure 48: The simulation and measurement results of insertion loss of the first version W-Band SPDT switch

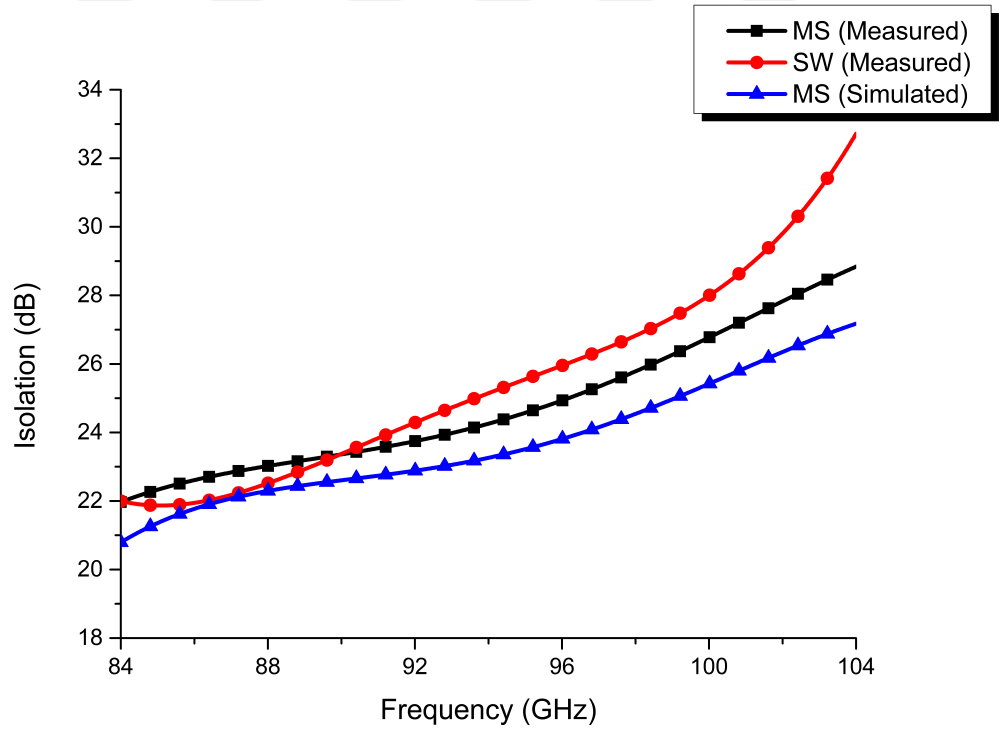

Figure 49: The simulation and measurement results of isolation of the first version W-Band SPDT switch

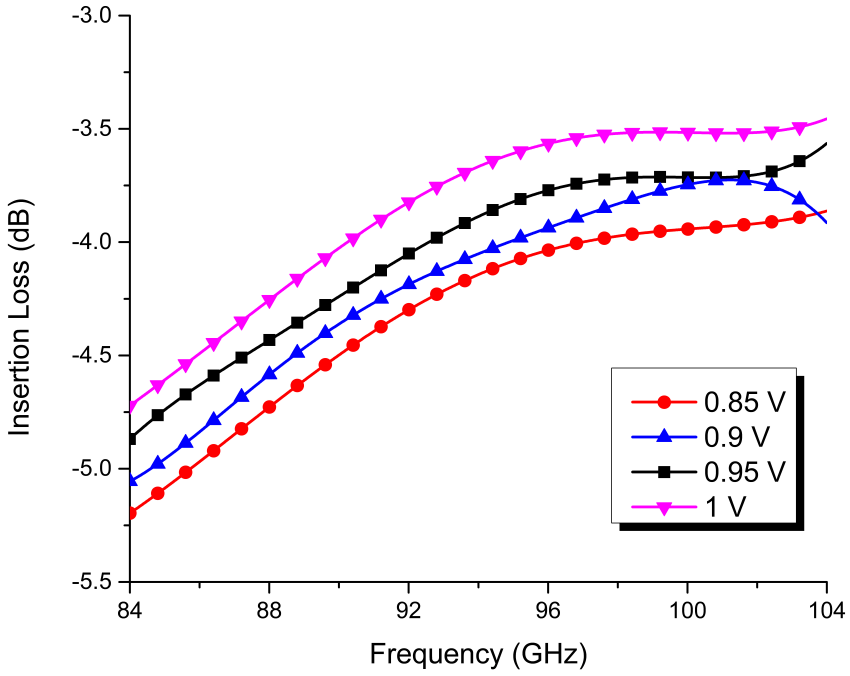

Figure 50: The measurement results of insertion loss of the first version microstrip W-Band SPDT switch at different bias voltages

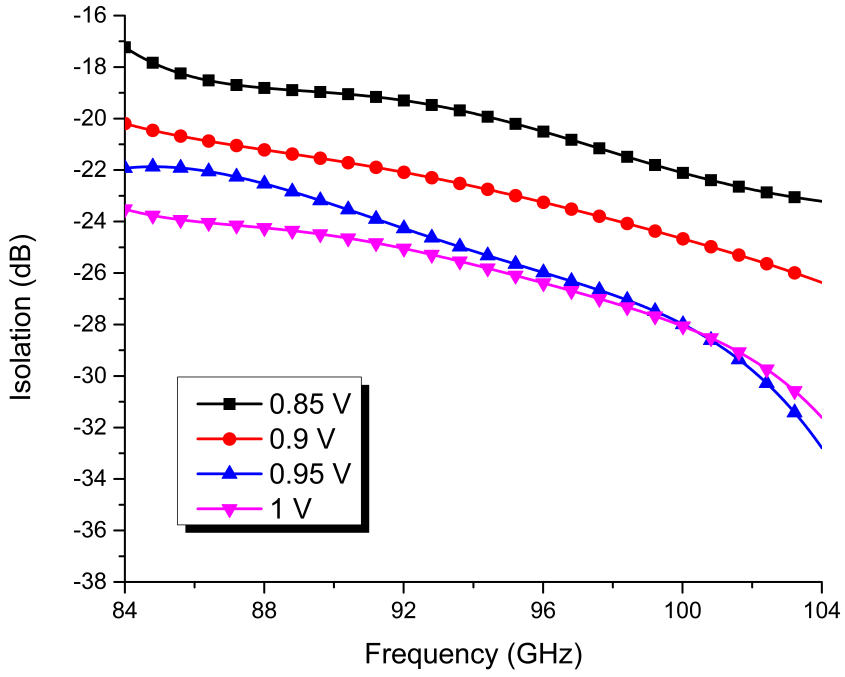

Figure 51: The measurement results of isolation of the first version microstrip W-Band SPDT switch at different bias voltages

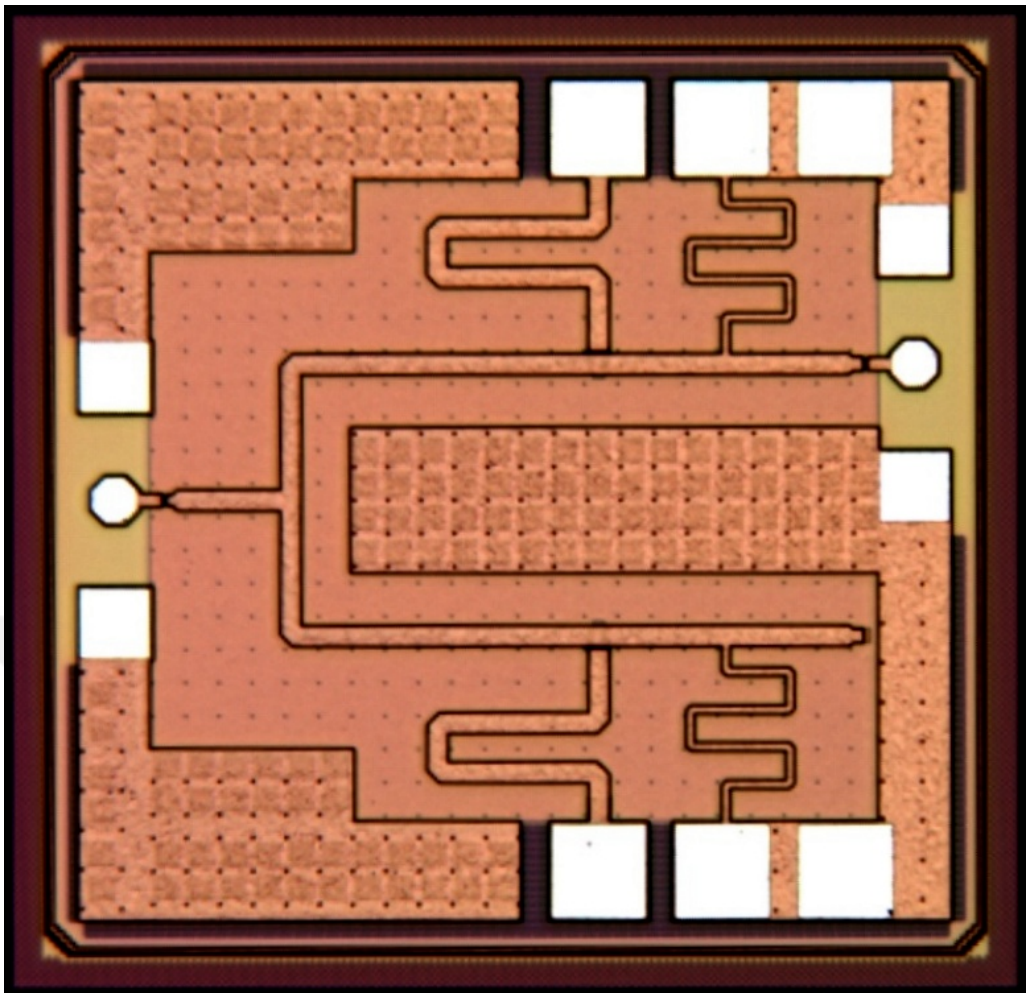

Figure 52: The micrograph of the second version W-Band SPDT switch

switch is shown in Fig. 52. The chip occupies 0.56 mm^2 (0.76 x 0.74 mm) and the bias voltage is set to be 0.95 V for a tradeoff between IL and P_{DC}. The circuit draws a total of 5 mA from 0.95 V supply (P_{DC} of 4.8 mW). Fig. 53 to 55 shows the simulation results of the new SPDT switch. The input and output return loss of the chip is better than -13 dB between 70-110 GHz and peak isolation is 22 dB at 95 GHz and is higher than 20 dB for the same frequency band. The simulations show that the IL of the chip less than 2.4 dB and minimum of 1.7 dB including the effect of the pads. Without the pads, minimum IL drops to 1.6 dB and is better than 2 dB across the entire bandwidth which is a significant improvement from previous SPDTs. The previous measurement results show that 0.5 to 1 dB increase in IL can be expected due to reasons mentioned before. Even with 1 dB increase, the IL of the SPDT is expected to remain better than 3 dB without RF pads from 70 to 110 GHz which makes this design suitable to be used in the proposed W-Band receiver.

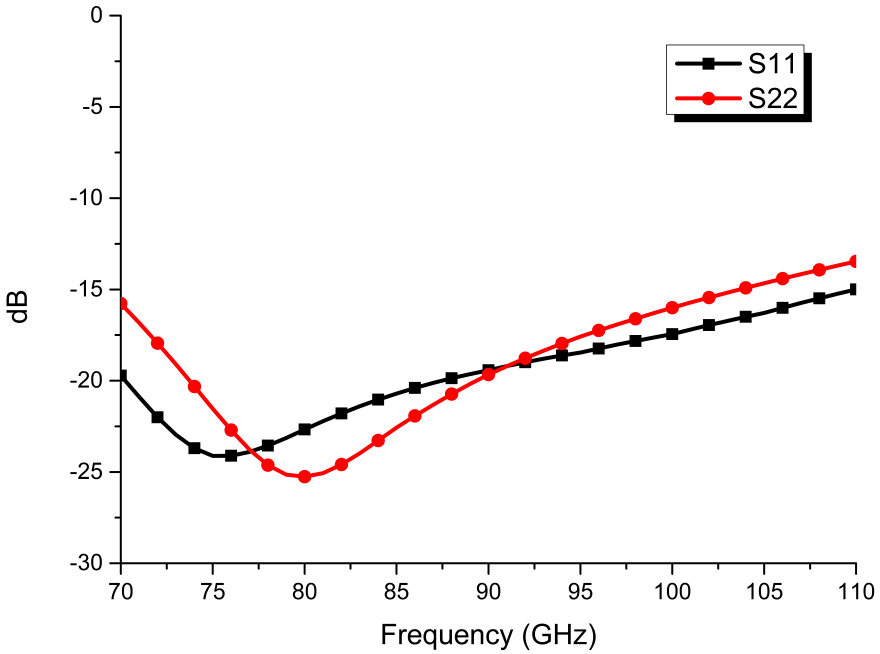

Figure 53: The simulation results of the input and output return loss of the second version W-Band SPDT switch

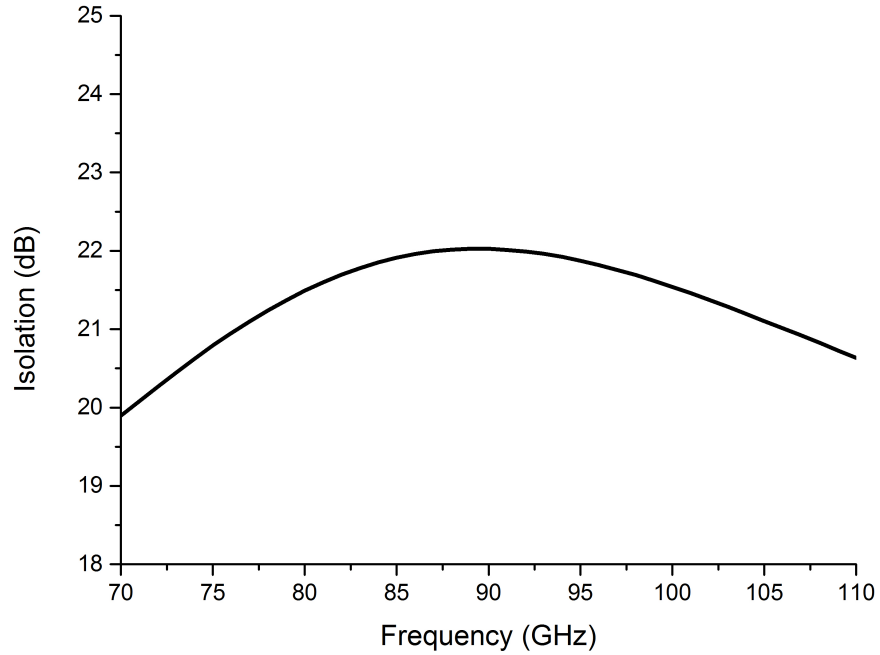

Figure 54: The simulation results of the isolation of the second version W-Band SPDT switch

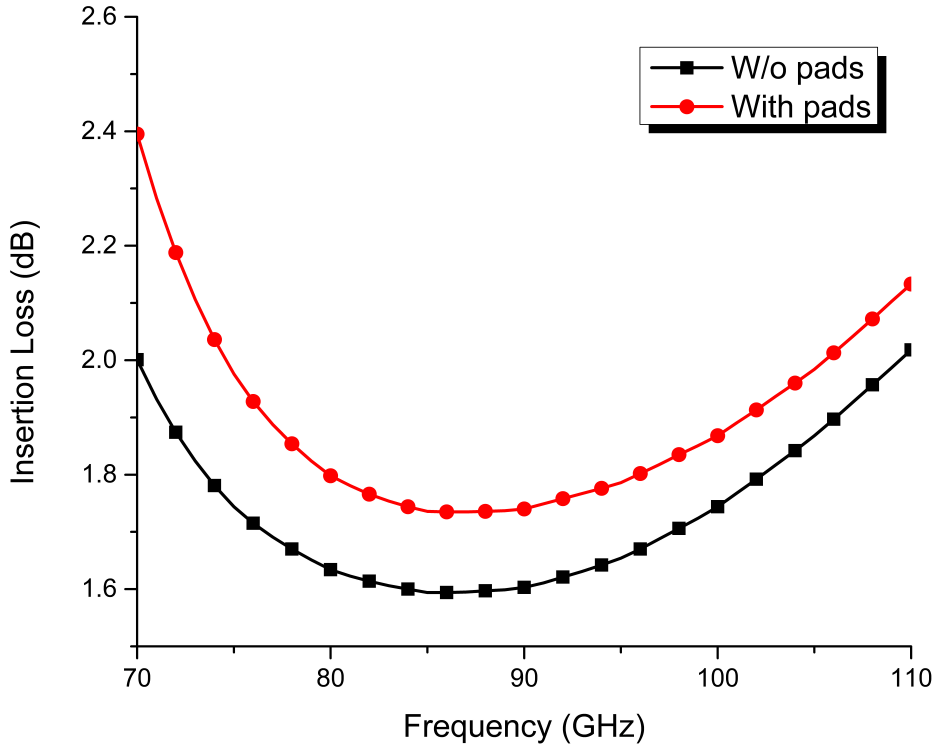

Figure 55: The simulation results of the insertion loss of the second version W-Band SPDT switch with and without RF pads

Table 6: Summary of performance of the W-Band SPDT and comparison with the SoA SPDTs

	Tech.	Tpg.	IL @ 70-110 GHz (dB)	IL_{MIN} (dB)	Iso. (dB)	P_{DC} (mW)	Area (mm^2)
[51]	90 nm SiGe	$\lambda/4$ Shunt Rev. Sat. HBT	<2	1.1*	>20	5.9	0.21*
[59]	0.13 μm SiGe	$\lambda/4$ Shunt Rev. Sat. HBT	<5	2	>22	9	0.36
[60]	50 nm InAlGaAs HEMT	$\lambda/4$ Shunt Rev. Sat. HBT	<2.3	1.8	>20	0	0.75
This Work	**0.13 μm SiGe**	$\lambda/4$ **Shunt Rev. Sat. HBT**	**<2***,**	**1.6****	**>19****	**4.8**	0.56

**without pads **simulated*

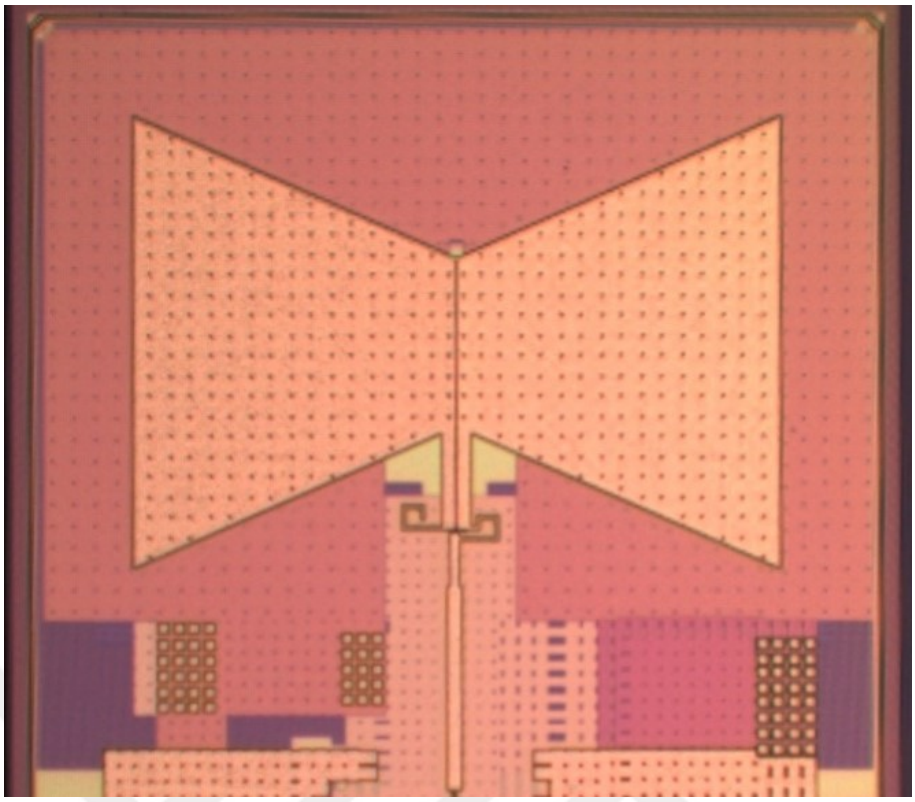

Figure 56: Micrograph of the W-Band LBE on-chip antenna

Table 6 present the summary of performance of the second version W-Band SPDT switch in comparison with similar SPDT switches operate at W-Band. Even though the minimum IL and isolation are not the best, the IL stays low across the entire 70-100 GHz band which is an excellent performance for wideband systems.

3.2.4 Antenna

The S-parameters of the standalone antenna fabricated in IHP's BEOL run is measured on-wafer with substrate thickness of 750 μm. The micrograph of the antenna is shown in Fig. 56.The total area of the antenna is 2.4 mm^2 (1.5 x 1.6 mm).

The first simulations were done in ADS and after the measurement, HFSS is used to obtain better correlation between the measurement and simulation results. Fig. 57 presents the simulation results obtained in HFSS and ADS compared to the measurement results. The measured S11 is better than -9 dB between 80-100 GHz. The HFSS simulation are in better agreement than ADS which overestimates the bandwidth and the resonance frequency is also shifted in ADS simulations. This

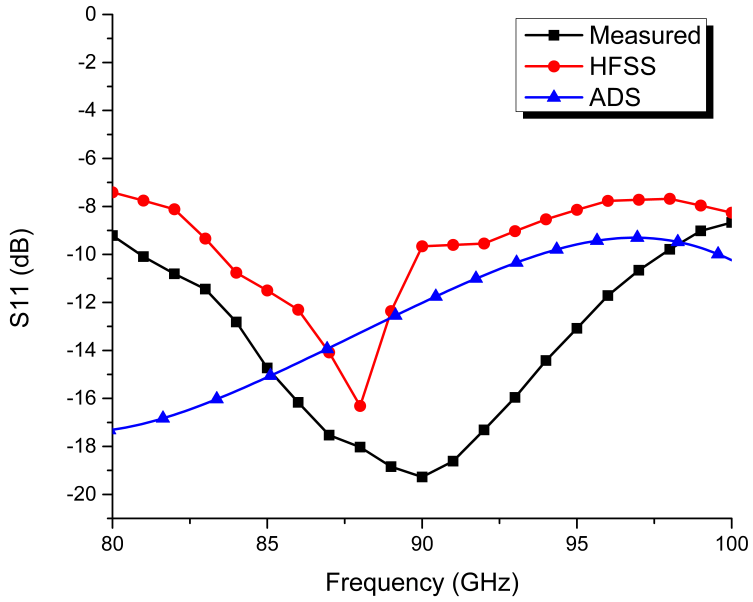

Figure 57: Measured and simulated input return loss of the W-Band antenna

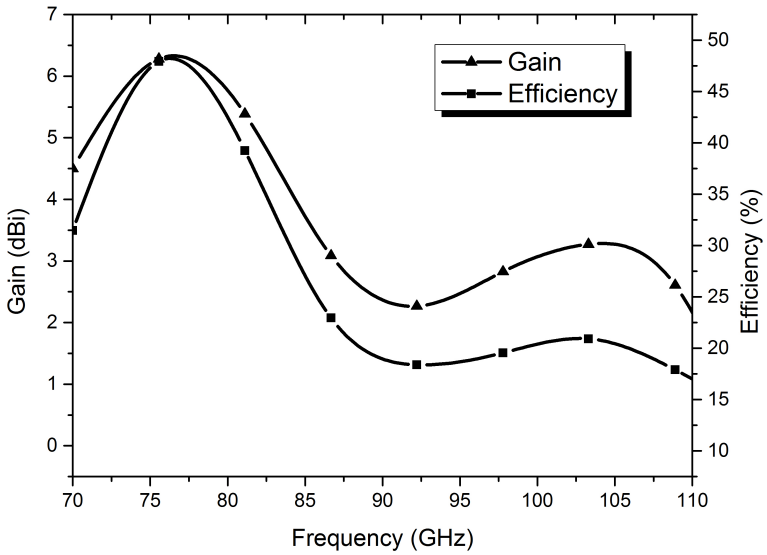

Figure 58: Simulated gain and efficiency of the W-Band antenna in ADS

result can be attributed to the presence of the backside etched areas which cannot be modeled properly in 2.5D simulations. The gain and efficiency simulation results obtained from ADS are presented in Fig. 58. The peak efficiency is around %48 and the corresponding gain is 6.5 dBi. However the gain is also overestimated in ADS by 2-3 dB compared to HFSS which shows -1 dB of gain with around %15-

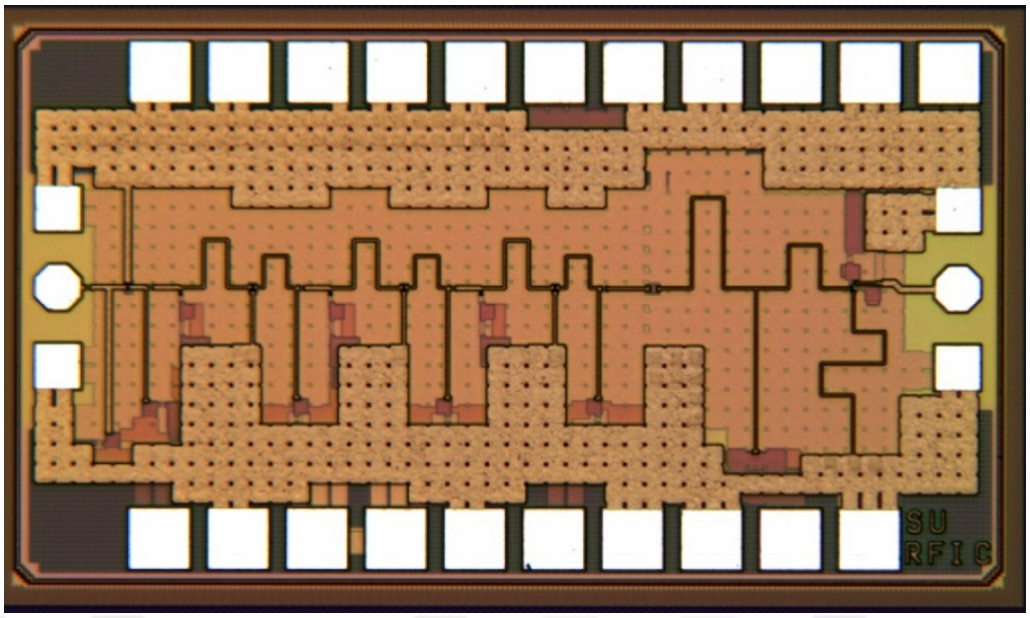

Figure 59: Micrograph of the W-Band TPR without the antenna

%20 of efficiency. At 300 μm substrate thickness, the matching does not degrade significantly, however gain decreases by another 2-3 dB.

The obtained performance of the antenna is relatively low for an LBE antenna which can achieve almost %70 efficiency or better at mm-wave frequencies [61]. Nevertheless, the results are sufficient for the proposed radiometer systems.

3.3 TPR and Dicke Radiometer System Implementations

The designed sub-blocks of PD, LNA and antenna are found to be suitable to be used in the radiometer systems. To demonstrate this, completed front-end receivers are implemented in the form of TPR and Dicke radiometer. Even though the Dicke radiometer is expected to achieve better sensitivity, TPR is also designed to further investigate the effect of gain fluctuations and external calibration performance. Furthermore, both the TPR and Dicke radiometer are implemented in two versions; one with the antenna and one without it. The reason for this is to characterize the systems easier using the external noise sources with the standalone receiver without the antenna. Complete characterization can be made using the receivers including the antenna.

The micrographs of the 4 implemented radiometers are presented in Fig. 59 - 62. The total area of the chips are; 0.88 mm^2 (1.25 x 0.7 mm) for TPR without

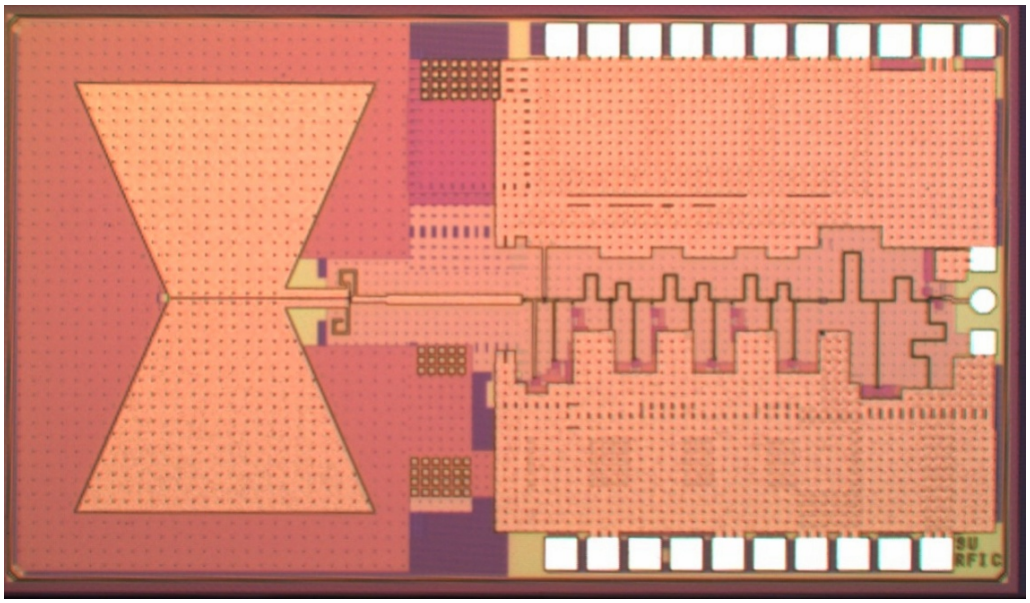

Figure 60: Micrograph of the W-Band TPR with the antenna

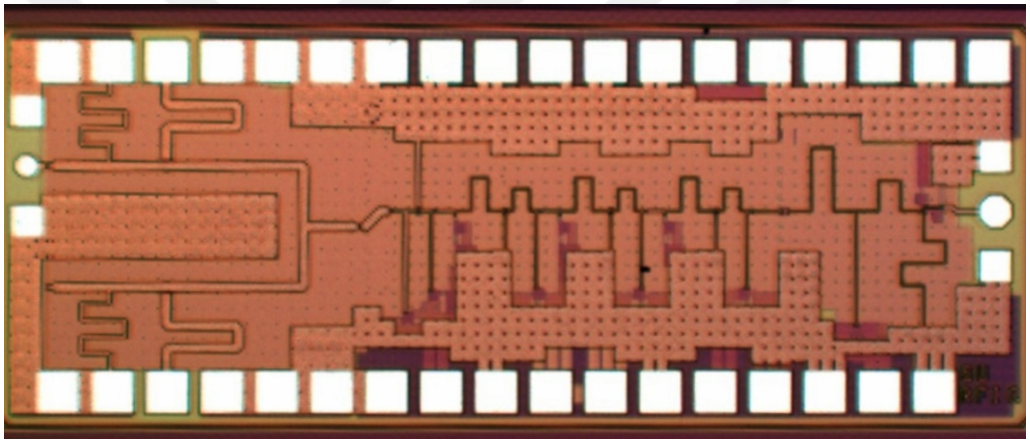

Figure 61: Micrograph of the W-Band Dicke radiometer without the antenna

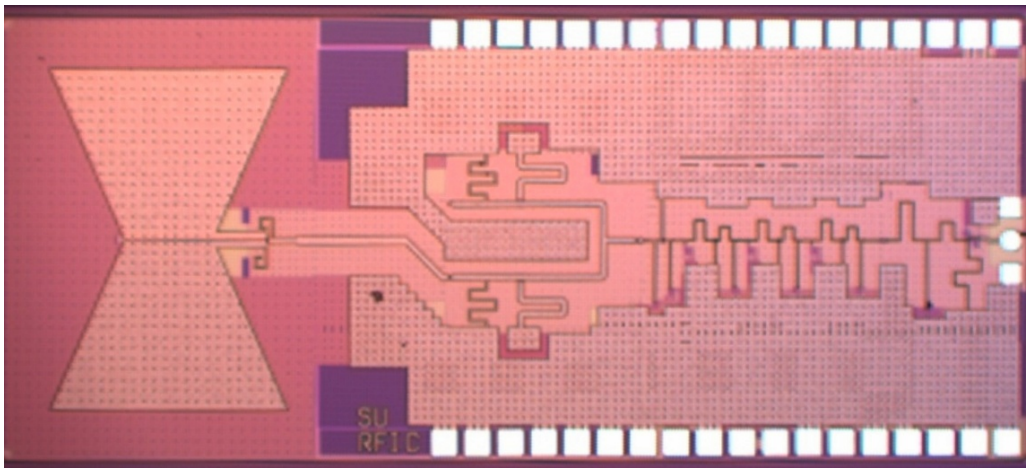

Figure 62: Micrograph of the W-Band Dicke radiometer with the antenna

antenna, 3.23 mm^2 (2.39 x 1.35 mm) for TPR with antenna, 1.4 mm^2 (1.9 x 0.73 mm) for Dicke radiometer without antenna and 4.17 mm^2 (3.11 x 1.34 mm) for Dicke radiometer with antenna. The increase in the area for the systems including the antenna is mainly due to the width of the antenna (1.34 mm) dictating the width of the complete system. As a result, the remaining areas are filled with bypass capacitors and ground metals. The power consumption of the TPR systems are only 8 mW and 12.8 mW for Dicke Radiometer.

All of the sub-blocks were designed to match 50 Ω therefore the loading effects on each other are minimal for both of the systems. Only in the Dicke radiometer with antenna, a small 50 Ω TL is placed between the antenna and SPDT to fit the blocks in a more convenient way.

The achievable NETD of the systems are analyzed using simulation and measurement results. The MATLAB code to calculate the NETD is given in Appendix A. Without any calibration, the NEP of the PD is calculated using the rms noise value at DC which corresponds to 2.6 $pW/Hz^{1/2}$ at 85 GHz. This is 10 dB increase in NF of the PD which becomes around 37 dB. The resulting NETD is 1.6 K for the TPR using 30 ms integration time and 35 GHz of bandwidth, without accounting in the gain fluctuations of the LNA. However, if external calibration is to be applied, the system noise temperature is 3400 K and NETD is 0.21 K for the same integration time and bandwidth for the TPR assuming the calibration frequency is 100 Hz. The same calculations are performed for Dicke radiometer; using the simulated 1.6 dB IL of the SPDT switch. The system noise temperature is 4900 K and 0.3 K NETD is found. Even with assuming 2 dB IL for the SPDT, the NETD only increases to 0.33 K. Even though the TPR achieves lower NETD in calculations due to the absence of additional loss at the input, the complications of realizing an externally calibrated system can overwhelm the advantage of 0.1 K improved sensitivity. Also the calibration frequency might be lower than 100 Hz for an externally calibrated system, hence reducing the NETD improvement even more.

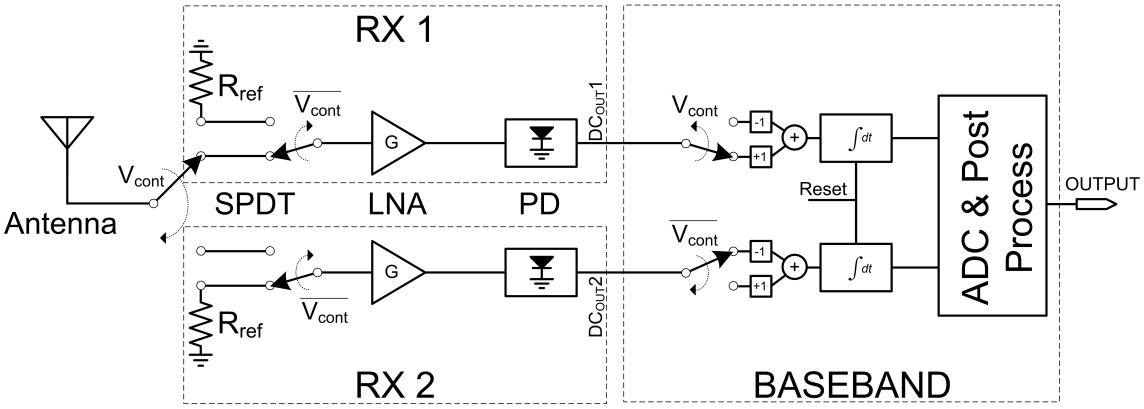

Figure 63: Detailed block level diagram of the dual channel radiometer architecture

3.4 Dual Channel Radiometer System Implementation

3.4.1 System Description

The proposed dual receiver W-Band radiometer is illustrated in Fig. 63. The basic operating principle is the same as the well-known Dicke radiometer. An SPDT switch alternates between the reference resistor (R_{ref}) and the antenna, and the received power is detected by the PD after being amplified by the LNA which reduces the system noise temperature. However, when the receiver is detecting the noise power, the antenna is isolated from the system therefore the scene is not observed anymore. The dual receiver system gets around this problem through the use of an SPDT switch tree which are controlled by V_{CONT} and $V_{CONTBAR}$ voltages. When the R_{X1} is directed to the antenna, R_{X2} measures the noise power of R_{ref} and vice versa. Consequently, the signal power received by the antenna is always sampled by either R_{X1} or R_{X2} while the other one completes its calibration cycle. An example of the transient output signals is presented in Fig. 64 with the assumption that the noise of the LNAs are uncorrelated. Both the output signals can be integrated separately at the baseband circuit, then averaged. The final output becomes the average of the output of the signals, consequently signal to noise ratio (SNR) improves by $\sqrt{2}$. Effectively, the total integration time is doubled since receivers produce a total of $\tau \cdot f_{switch}$ number of samples for the duration of integration compared to $\tau \cdot f_{switch}/2$ of a single receiver would produce. The same process can also be thought as combining N exposures of the same scene image which improves the SNR by $\sqrt{N}$. Ultimately, the NETD of the radiometer would improve by the same amount.

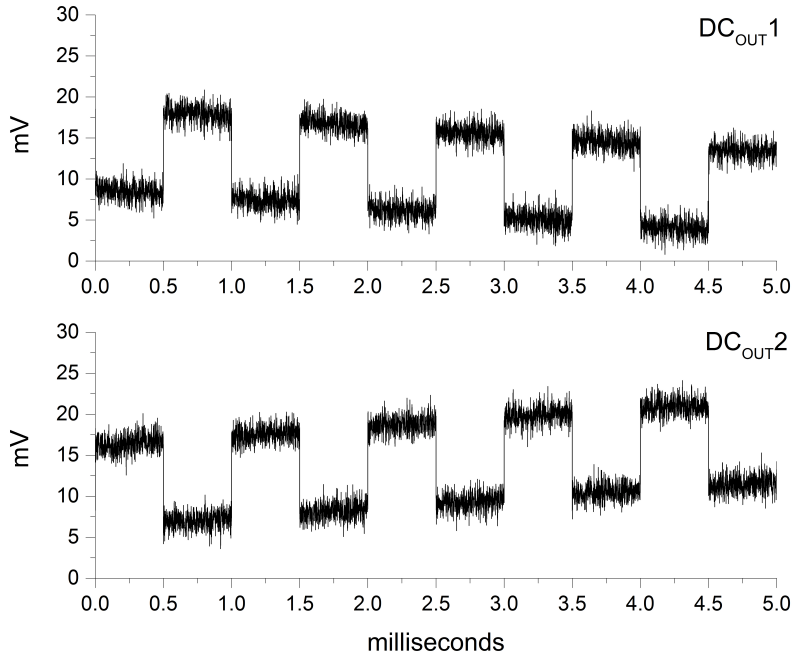

Figure 64: Output of the R_{X1} and R_{X2} in the presence of gain fluctuations

There are several complications when realizing the proposed system. First, the additional SPDT switch at the input introduce additional loss which is highly undesired and could render the advantage of using dual receivers useless or degrade the NETD to even worse. However, instead of cascading the same SPDT switch which would double the IL in terms of dB, the complete switch tree can be designed as one, such that the IL increases by a relatively insignificant amount. Second, the power consumption is doubled which is unfortunately inevitable. Nevertheless, since the major contributor to the power consumption is the LNA, it can be designed to have rather low P_{DC} while still providing sufficient gain thanks to the high f_t of the technology.

The final consideration is the total area of the chip which would also be doubled without an on-chip antenna. The back-end processes are rapidly evolving and high level of integration is becoming more desirable in mm-wave designs. In fact, there are already several works that incorporate on-chip antennas in their design [7], [62]. However, the physical size of the antenna is dictated by the wavelength of the desired signal and is relatively independent of the design. For instance, at 90 GHz, an on-chip half-wave dipole antenna would have approximately 800 μm of length. Consequently, at least one dimension of the total chip area is usually fixed by the

antenna. On the other hand, receivers can be designed to occupy much smaller area compared to the antenna. In the case of dual receivers, the final die size would increase by less than twice since the antenna would occupy larger portion of the area anyway.

3.4.2 Switch Design

At W-Band, SPDTs designed with HBTs typically exhibit around 2 dB insertion loss. For the implementation of dual receiver, system a total of 3 SPDTs configured in a tree formation is required which is shown in Fig. 63. This configuration results in 4 dB IL or more by simply cascading separate SPDTs which is unacceptable to achieve low NETD.

The main loss mechanisms in SPDTs are the parasitics associated with the shunt HBTs and the conductor loss of the passives. The passive losses cannot be directly avoided, however, the shared nodes of the $SPDT_1$ and $SPDT_2$ as well as $SPDT_1$ and $SPDT_3$ can be exploited to avoid the use of additional HBTs at these nodes which improves the IL significantly.

Fig. 65 presents the schematic of the switch. The Q_1 and Q_4 transistors are shared between the main SPDT and secondary SPDTs. When V_{CONT} is high, Q_1 and Q_3 is shorted to ground and the antenna signal is directed to the LNA_2 whereas the LNA_1 is directed to the reference resistor and vice versa. The only additional loss in this design compared to a single SPDT is the conductor loss of the 70° TL which is approximately 0.5 dB at 90 GHz. Consequently, the total IL from antenna to LNA would be increased from 2 dB to around 2.5 dB which is exceptional compared to the 4 dB of the cascaded design. Also, the power consumption of this switch is only 4 mW (4.2 mA from 0.95 V supply).

Similar to previous SPDT switch designs, the HBTs are utilized in reverse saturation mode which reduces insertion loss slightly. The overall IL can also be further improved by an amount of 0.2-0.3 dB by adding $\lambda/4$ TLs at the base of the transistors such that the C_{BE} parasitic capacitance floats. However, this also reduces isolation between ports by 3-4 dB. To achieve 20 dB isolation or more, the addition of this TL is avoided.

The electrical length of the TLs are slightly adjusted from $\lambda/4$ to compensate

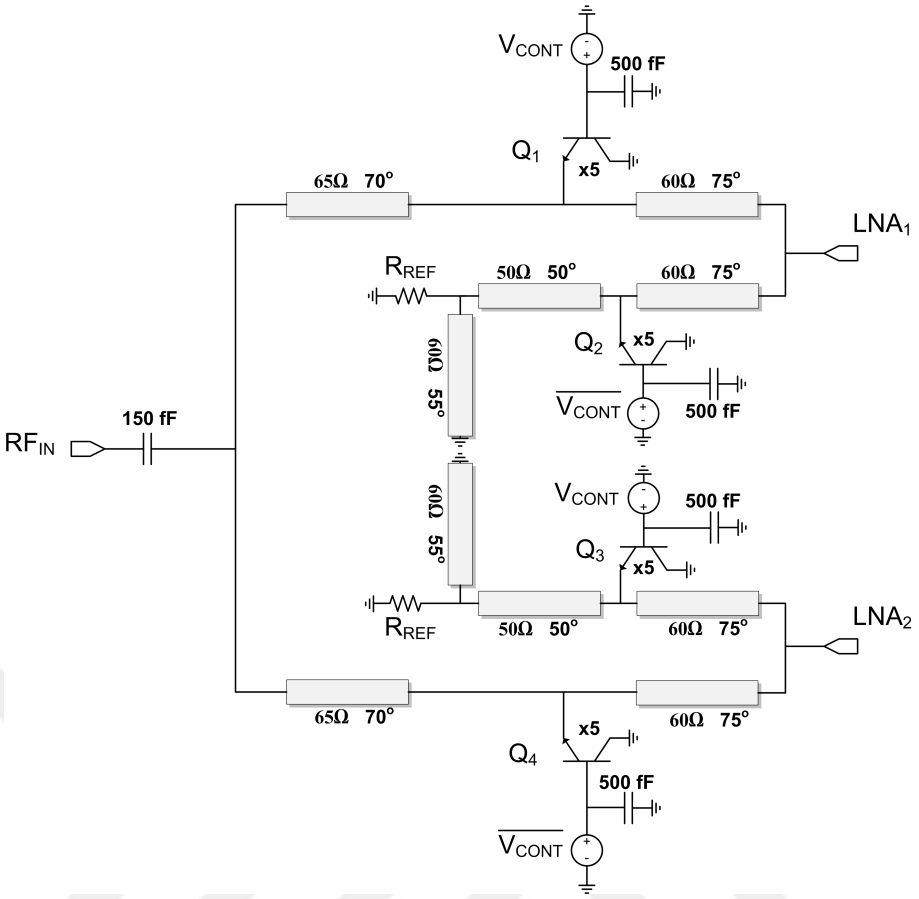

Figure 65: The schematic of the designed switch tree for W-Band dual receiver radiometer

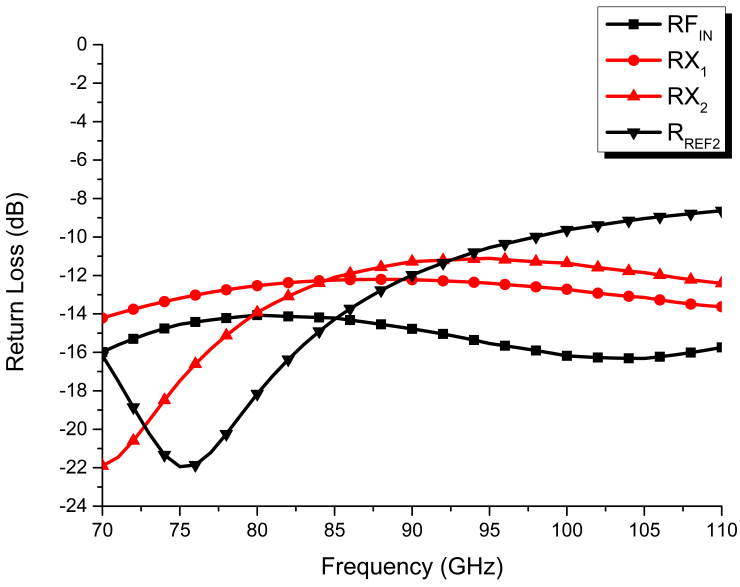

Figure 66: The simulated input and output return loss of the W-Band switch tree

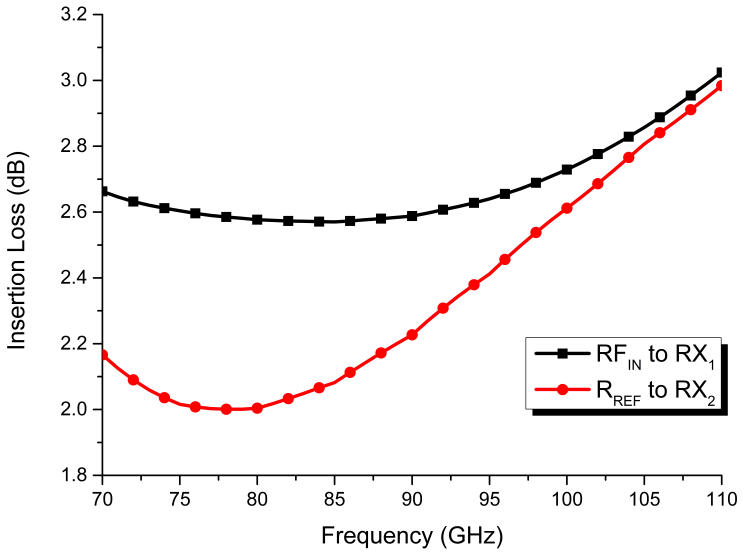

Figure 67: The simulated insertion loss of the W-Band switch tree

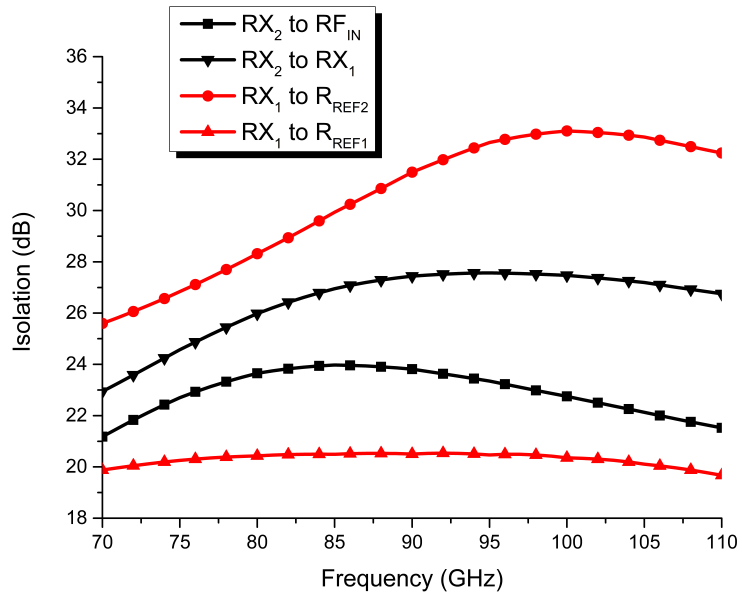

Figure 68: The simulated isolation of the W-Band switch tree

for the parasitic effects of the HBTs and also, to improve matching. Reference resistors are 50 Ω polysilicon resistors that are matched using the shunt TLs which also provide a DC current path to HBTs. DC block capacitors are not used at the LNA ports since it is included at the input of the LNA and the 150 fF capacitor facilitates the input matching. Similar to PD, full chip EM simulation is performed that includes all the passive components.

A standalone version of the switch is not taped-out seperately. The simulation results are presented in Fig. 66-68 for the case when the R_{X1}, (LNA_1) is directed to the RF_{IN} (antenna) and R_{X1} (LNA_2) is directed to the reference resistor (R_{REF}). The simulated return losses are better than -8 dB for the entire W-Band. The minimum insertion loss from antenna to the LNA is 2.6 dB and is below 2.8 dB from 70 to 105 GHz. The IL from R_{REF} to LNA is 2-3 dB due to the shorter path between these nodes. This result also shows that cascading SPDT switches would result in 4-6 dB IL compared to the 2.6-3 dB IL of the designed switch tree. The isolation is worst between the R_{REF} and the R_{X1} with 19-20 dB, and is much better for the other remaining ports. The simulation results can be verified by the complete front-end system measurements.

3.4.3 Dual Receiver Front-end System

The dual receiver radiometer is implemented using the previously designed and measured LNA and PD as well as the new switch tree designed specifically to this receiver. Similar to previous radiometer systems, two versions are taped out, with and without the antenna for characterization purposes. The layout of the radiometers are presented in Fig. 69- 70. The area of the system without the antenna is 2.47 mm^2 (1.95 x 1.27 mm), 4.2 mm^2 for the one with the on-chip antenna, and the power consumption is only 20 mW in which the 16 mW of this is due to LNAs and 4 mW due to the switch.

Using the measurement results of 35 GHz ENB, 17.5 dB average gain and 4.5 dB NF of the LNA, 27 dB NF of PD, 2.7 dB IL of the switch, and assuming 30 ms integration time, 290 K T_0 and T_A, the NETD of the dual receiver radiometer is calculated by factoring in the multiplier by 2 for the integration time. The resulting NETD of the radiometer is 0.27 K. For comparison, 0.3-0.33 K NETD is calculated for a single receiver radiometer assuming 1.6-2 dB IL for the SPDT. The corresponding improvement is approximately %10-%20. The theoretical improvement of using dual receivers is around %30 and the actual improvement is lower due to the increased IL of the switch.

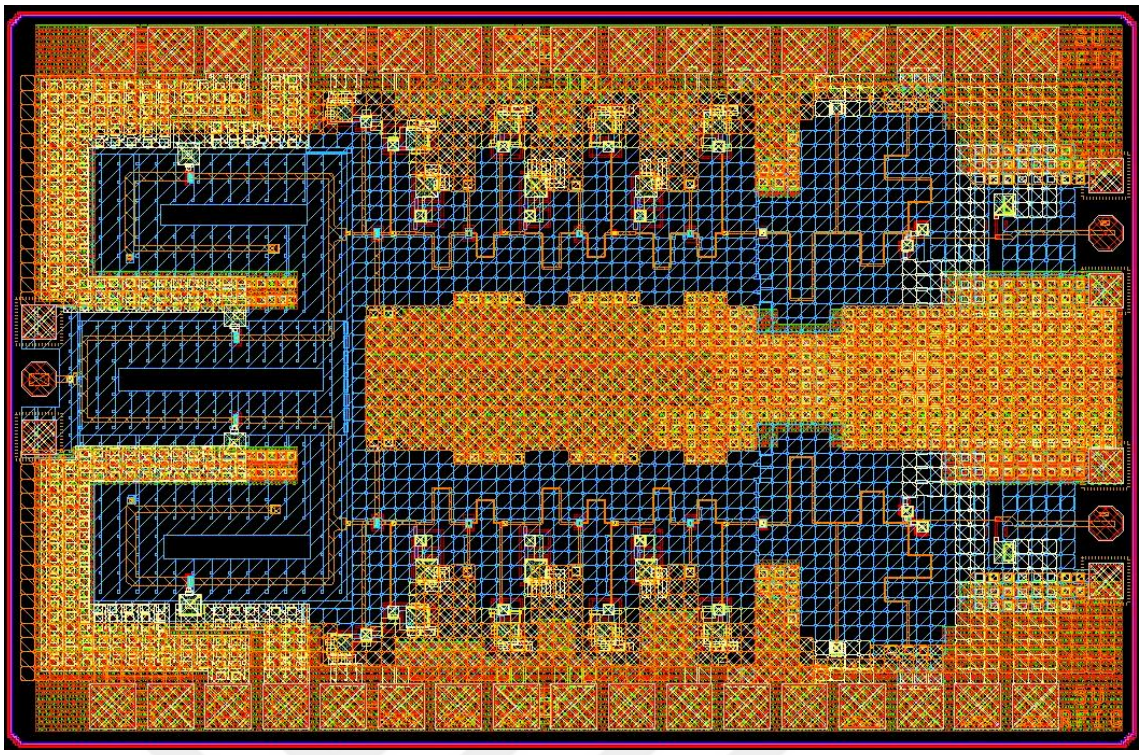

Figure 69: Layout of the W-Band dual channel radiometer without the antenna

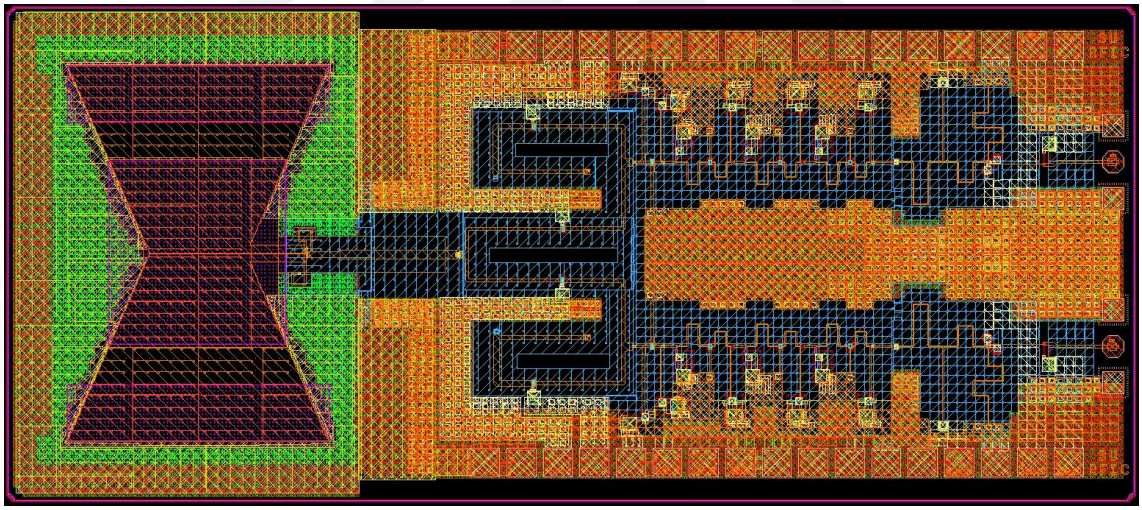

Figure 70: Layout of the W-Band dual channel radiometer with the antenna

3.5 Summary of Performance and Comparison of the Implemented Systems

Table 7 presents the performance summary of the implemented TPR, Dicke and dual channel radiometer systems in comparison with state-of-the-art W-Band silicon MMIC radiometers. The level of integration varies between the published works where the only front-end integration is implemented the most. The presented TPR

Table 7: Summary of performance of the implemented radiometer systems and comparison with SoA W-Band radiometers

	Tech.	Topology	System Integration	P_{DC} (mW)	Area (mm^2)	NETD
[63]	65 nm CMOS	Dicke Free Dual Receiver with Hybrid	Front-end +off-chip antenna on nitride sub.	196	5.32	0.43*
[64]	0.18 μm SiGe	Dicke	Front-end + Baseband	200	12.5	0.4
[54]	0.12 μm SiGe	Dicke	Front-end	35	0.4	0.83
[54]	0.12 μm SiGe	TPR	Front-end	27.6	0.25	0.69**
[13]	0.13 μm SiGe	Dicke Using Switched Amplifier	Front-end	28.5	3.42	0.21
[65]	65 nm CMOS	Dicke	Front-end	110	0.41	1.1
This Work	**0.13 μm SiGe**	**TPR**	**Front-end + Antenna**	**8**	**3.23**	0.21**
This Work	**0.13 μm SiGe**	**Dicke**	**Front-end + Antenna**	**12.8**	**4.17**	0.33
This Work	**0.13 μm SiGe**	**Dual Receiver Dicke**	**Front-end + Antenna**	**20**	**4.2**	0.27

**Measured at 20 ms int. time, rest are calculated at 30 ms **Assumed external calibration*

performances are based on the assumption that an external calibration methodology is present which might not be desirable in some applications. The demonstrated radiometers achieves <0.33 K NETD or better sensitivity calculated from simulation and measurement results which is one of the best performance presented in the literature compared to other silicon radiometers. The achieved performance is especially significant considering the power consumption of the implemented systems are also much lower than the recently published works.

4 D-Band Radiometer Design in SiGe BiCMOS

This chapter demonstrates the design methodology and experimental results obtained of the D-Band radiometer sub-blocks as well as the implemented systems. The achievable sensitivity of the D-Band TPR and Dicke radiometer are analyzed. Finally, comparison with SoA is presented with respect to recent literature.

4.1 Sub-Block Designs

4.1.1 Power Detector

The schematic of D-Band PD is presented in Fig. 71. A much more conservative design approach is taken in this design. First, the load resistance is reduced to 20 kΩ to decrease the supply voltage to 3 V and to also to drive the detector easier. Nevertheless, the load resistance can simply be increased by off-chip components along with the supply voltage to improve responsivity. Second transistor is also removed to reduce the number of bias voltages.

Major changes were made to widen the matching bandwidth of the circuit. Number of transistor is doubled whereas the bias voltage is kept same at 755 mV for a tradeoff between NEP and matching. Secondly double stub matching is employed utilizing shorted stubs. The characteristic impedance of the TLs are not selected to be the same for greater degree of freedom. Similar to W-Band design, all the TLs are meandered to reduce the total area.The electrical length of the implemented TLs as shown in the schematic of the circuit (Fig. 71) are given at 140 GHz. The geometry of the 500 fF MIM capacitors are slightly adjusted to increase the resonance frequency as well and the 100 fF capacitance is used for DC blocking. All the resistors are implemented using polysilicon resistors with a sheet resistance of 275 Ω.

The parasitic capacitance of the RF pads effects the matching of the circuit significantly. Rather than including it in the matching, 50 μm long 50 Ω microstrip line is added from the RF pads and a set of standard fixtures are designed including open, short, match and through as well as $\lambda/4$ lines at 110, 140 and 170 GHz to deembed the effect RF pads and the MSL. The EM simulation setup in ADS is presented in Fig. 72.

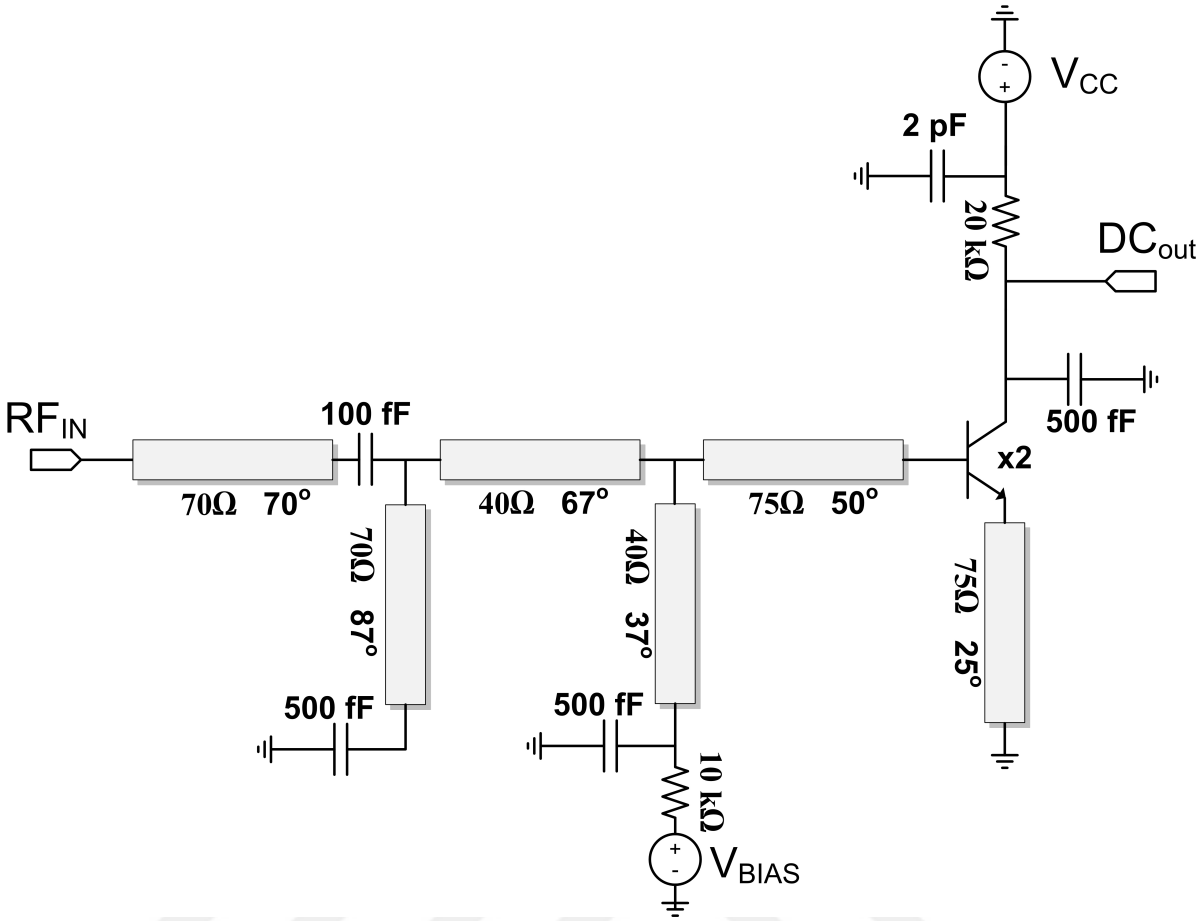

Figure 71: The schematic of the D-Band Power Detector

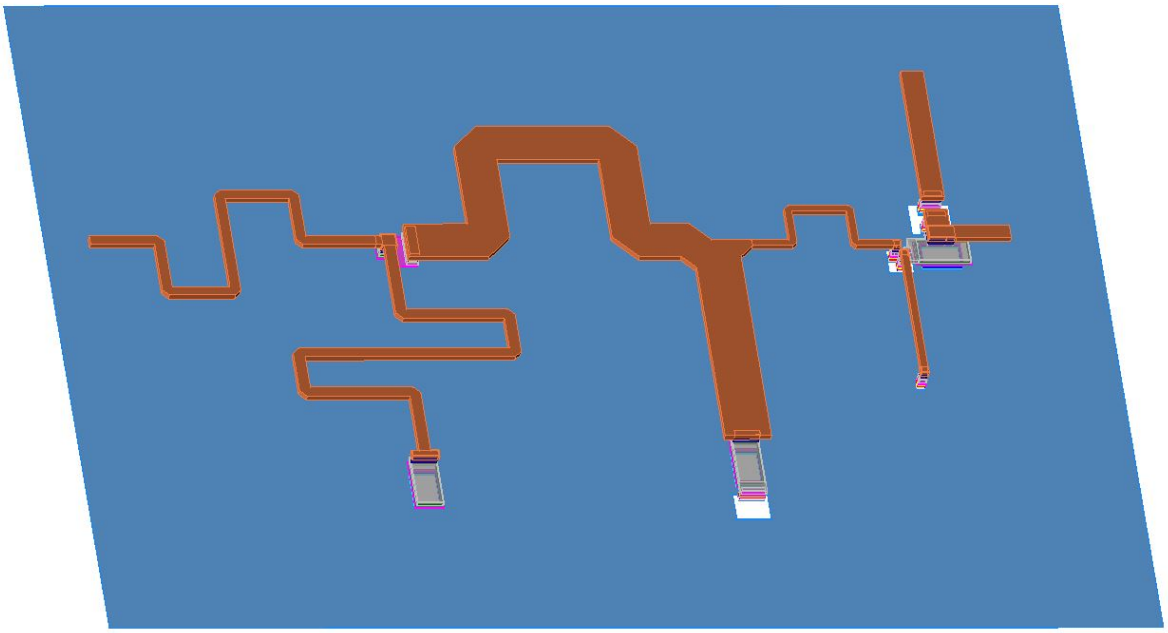

Figure 72: The EM simulation setup of the D-Band Power Detector

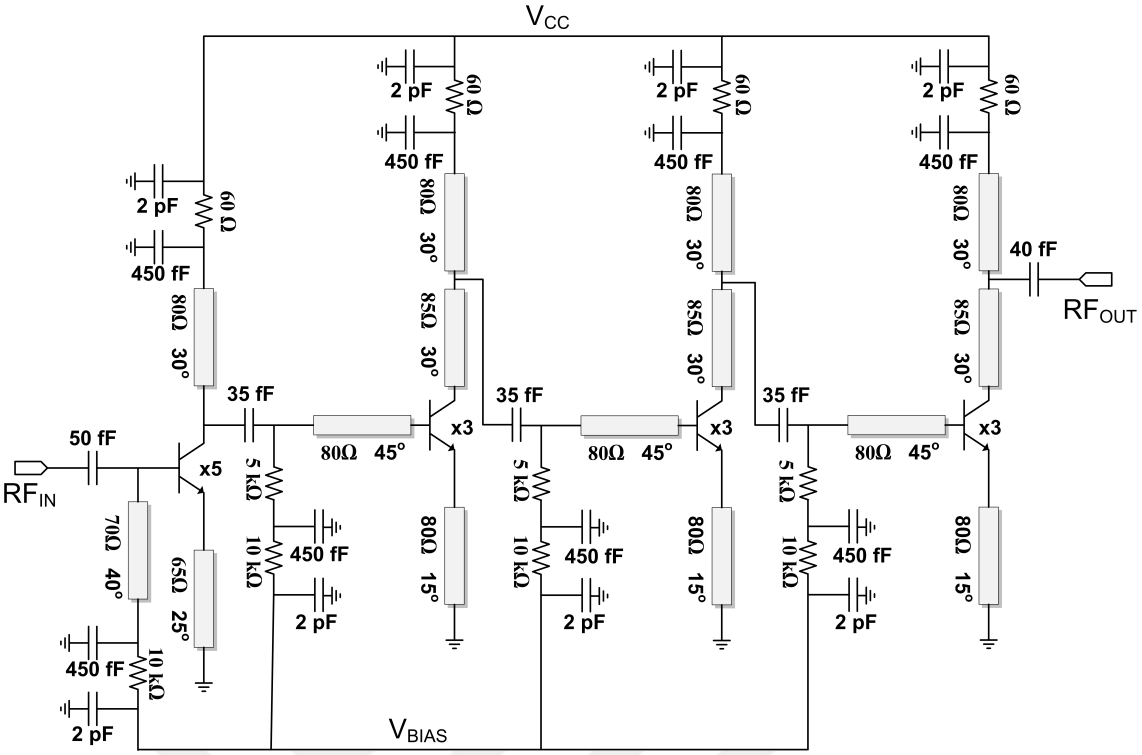

Figure 73: The schematic of the D-Band LNA

4.1.2 Low Noise Amplifier

The schematic of the 4 stage D-Band LNA is shown in Fig. 73. Similar approaches were made with the W-Band LNA in this design, however the topology is changed to keep the gain above 20 dB across the entire D-Band. Consequently, power consumption constraints are also relaxed compared to W-Band as a tradeoff since available gain per stage is much lower.

A cascode stage could provide 3-4 dB more compared to CE, as a result the two middle stages are implemented as cascode amplifiers. At the input, CE is chosen over cascode for wideband input matching as well as to avoid series TLs that would increase the overall NF. Similarly, the output is also implemented as CE for improved output matching.

Interstage matchings are designed using T-type networks utilizing high characteristic impedance MSLs along with MIM capacitors. The electrical length of the implemented TLs as shown in the schematic of the circuit (Fig. 73) are given at 140 GHz. 2.2 mA collector current is set for the first stage to optimize the noise performance and S11, 4.4 mA for the cascode stages and 3 mA for the last stage to achieve high gain. Since linearity is not a concern for radiometer systems as the

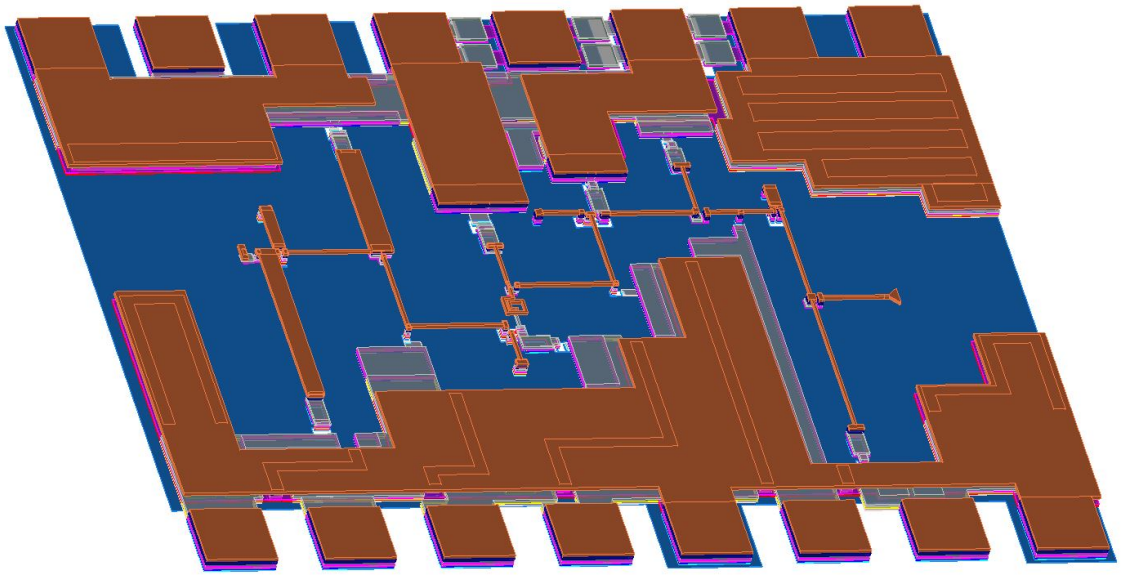

Figure 74: The EM simulation setup of the D-Band LNA

input power is usually well below -50 dBm, a relatively low 2.5 V V_{CC} for cascode and 1.5 V for CE stages are chosen.

Parasitic effects on the other hand, is a major concern at mm-wave frequencies, therefore full chip simulations are performed including all the vias, DC block capacitors and 450 fF bypass capacitors. Parasitic capacitances due to the RF pads are not included in the matching and EM simulations, since this LNA is designed to be used in a system and including the RF pads would require relatively major changes at the input and the output. Instead, a set of standard fixtures are designed for deembedding the RF pads. The EM simulation setup in ADS is presented in Fig. 74.

4.1.3 SPDT Switch

The schematic of the D-Band SPDT switch is presented in Fig. 75. Like the W-Band SPDT, this SPDT also utilizes $\lambda/4$ shunt transistors with reverse saturated HBTs. The 50 Ω matching at the antenna and reference port is achieved using shorted stub matching with 22° 50 Ω and 67° 50 Ω microstrip lines. The shorted stub also allows a DC path to ground for the HBTs. The effect of emitter-base capacitance is reduced by the 45° TL. This TL can also be made $\lambda/4$ which would improve IL at the center frequency, but in the expense of lower isolation and worse IL at the edge of frequency band. As a tradeoff 45° is chosen. The transistor size

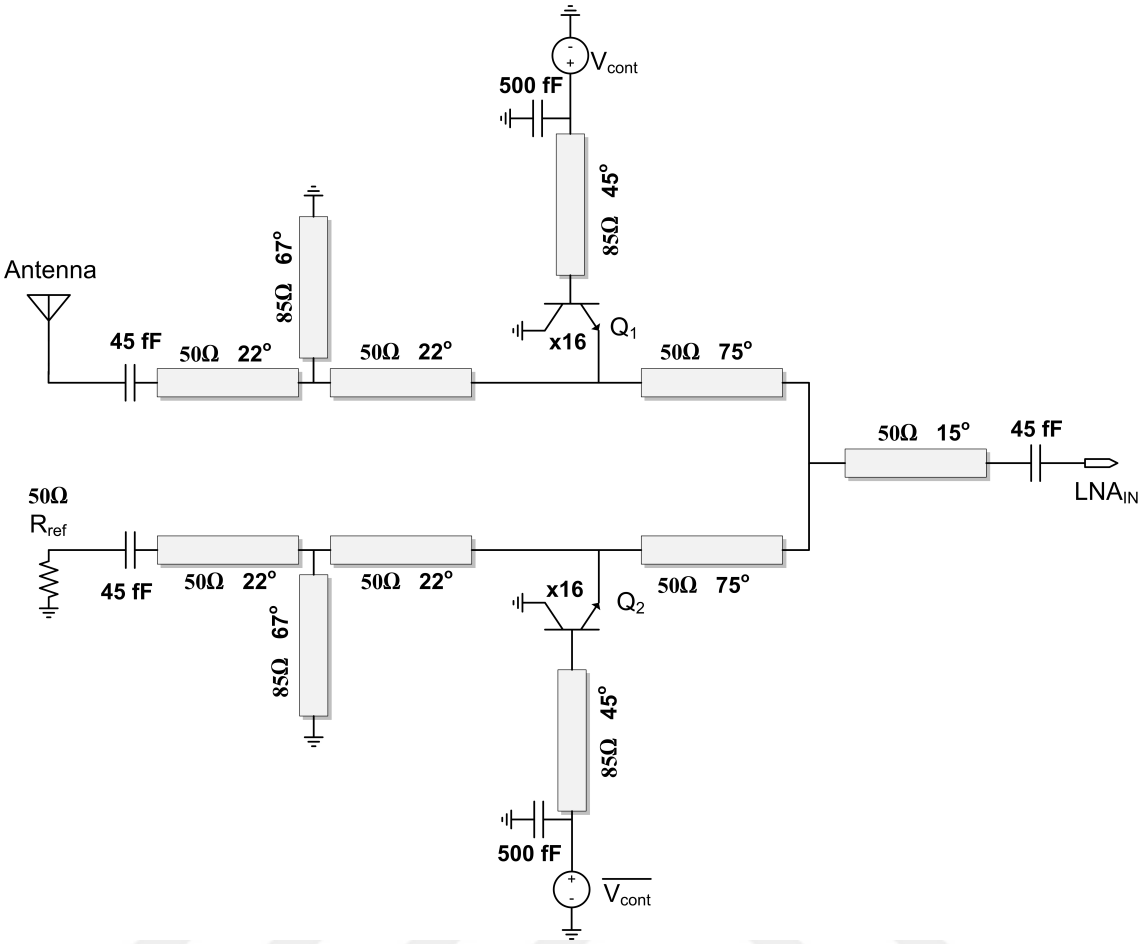

Figure 75: The schematic of the D-Band SPDT switch

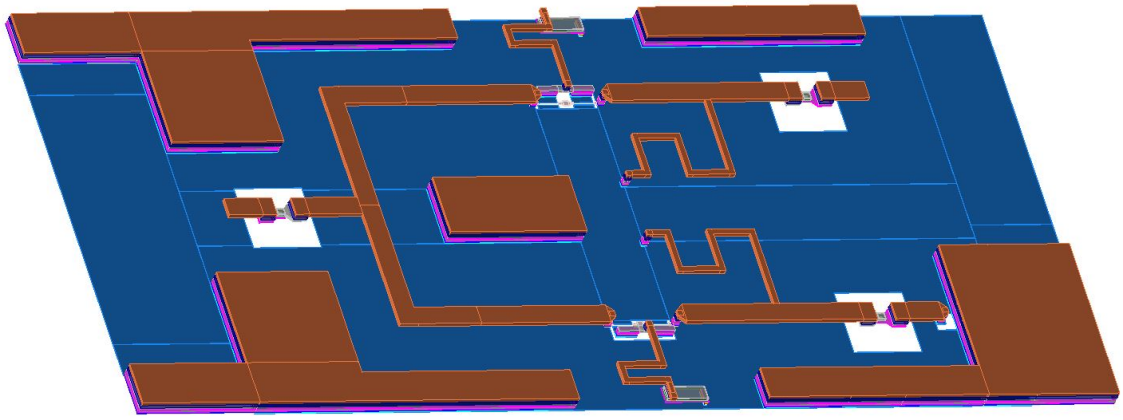

Figure 76: The EM simulation setup of the D-Band SPDT switch

is also the same with $16x$ shunt HBTs in parallel. The input matching at the LNA port is done with 75° and 15° TLs. The given electrical lengths are at 140 GHz.

45 fF MIM capacitors were not only used as DC block but also facilitates the matching of the circuit. 500 fF bypass capacitors which are self resonating are placed before the bias pads. 50 Ω reference resistor are placed using two 100 Ω

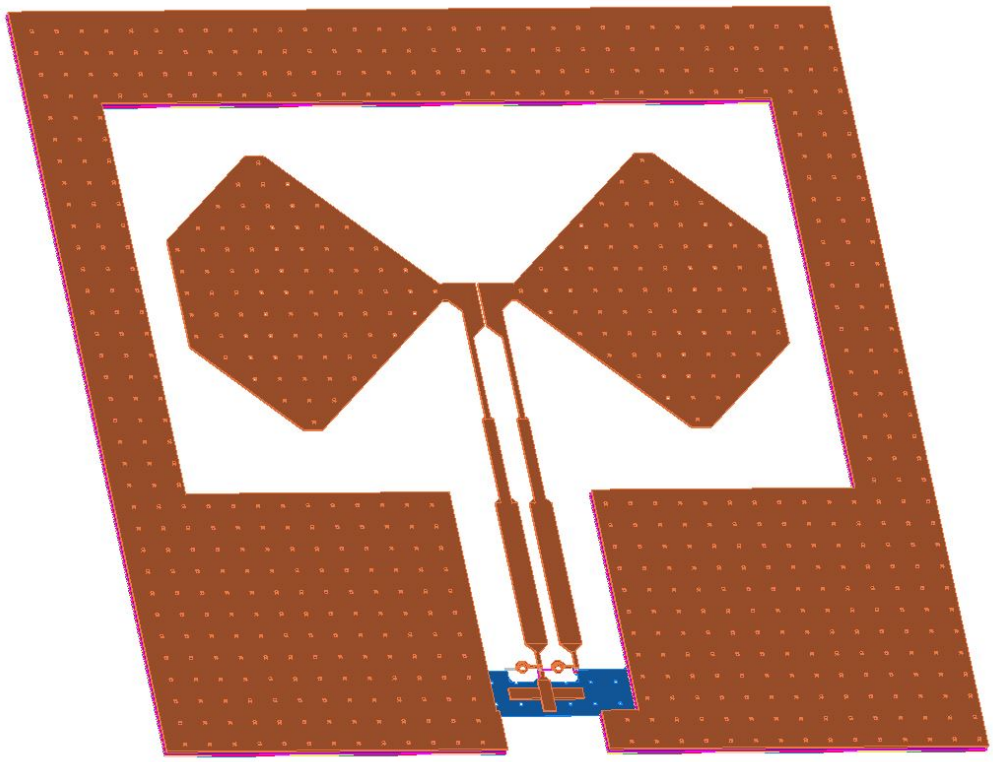

Figure 77: The EM simulation setup of the D-Band Antenna

poly resistors.Full chip EM simulations are performed using ADS as shown in Fig. 76. The RF pads are not included in the simulations and the matching. Similar to PD and LNA, the pad parasitics are left to be deembedded using the calibration fixtures.

4.1.4 Antenna

For the D-Band antenna design, the LBE process is utilized to achieve high efficiency, similar to W-Band. ADS simulation setup of the D-Band antenna is shown in Fig. 77. Due to the increased frequency, or equivalently smaller wavelength, the arms of the antenna are smaller, which are only 360 μm of length and 430 μm of maximum width. At D-Band, the fractional bandwidth is nearly %43, so achieving %40 or wider bandwidth requires additional design changes to the well-known bow-tie antenna. First, the edges are tapered at an angle of 45°. Consequently, the antenna is closer to a circular dipole antenna that has a greater bandwidth. To improve the matching bandwidth, the distance between the arms is set to 3.5 μm and the differential feedline is configured such that the characteristic impedance

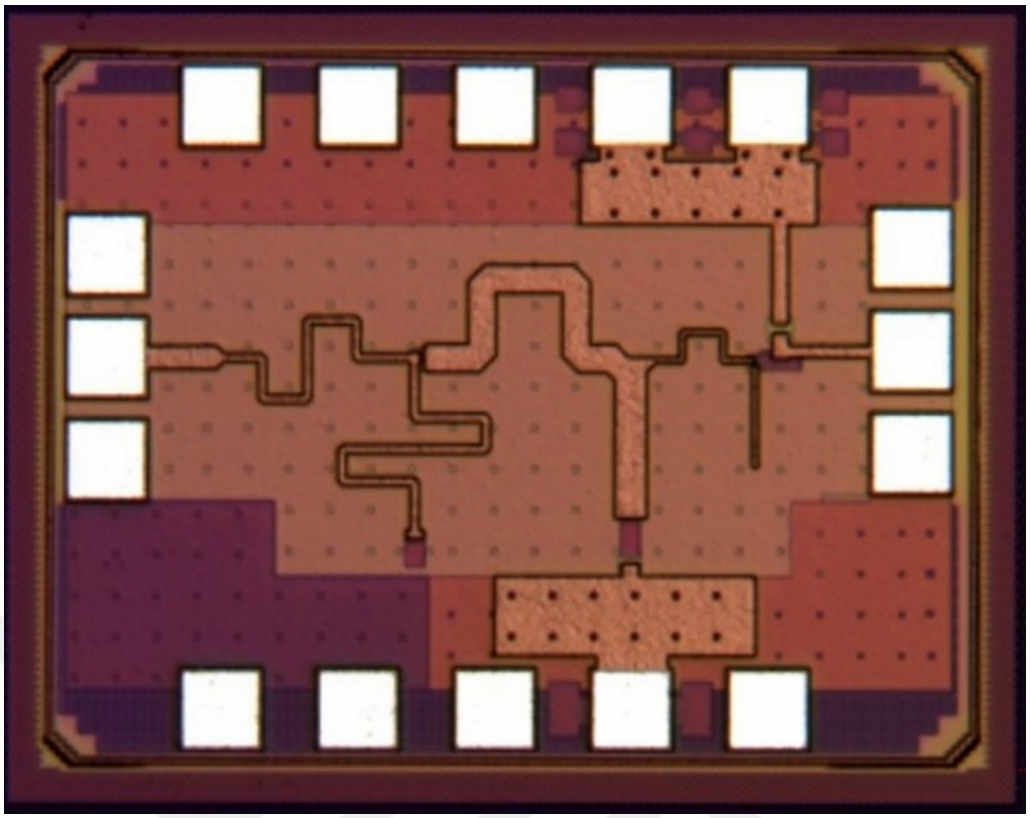

Figure 78: Micrograph of the designed D-Band power detector

gradually decreases and has a total length of 575 μm. Differential to single end conversion is done using an LC balun with 22 fF MIM capacitor and 55 pH inductork and balanced open stubs with 42 μm of length before the RF pad. The perimeter of the antenna is filled with metals from Metal1 to TopMetal2 to comply with the density rules. Active and poly fillers are also placed outside of the LBE areas for the DRC and all the metals are slotted in 4 by 4 μm squares.

4.2 Simulation and Measurement Results of the Sub-Blocks

4.2.1 Power Detector

The micrograph of the designed D-Band power detector is presented in Fig. 78. The chip occupies 0.36 mm^2 (0.69 x 0.53 mm) and draws 50 μA of current from 3 V supply when no RF power is present and 755 mV is applied to the base over a 10 $k\Omega$ resistor.

The input matching of the D-Band PD is shown in Fig. 79.In simulations, tithout the effect of the RF pads, the PD exhibits wideband input matching and input return loss is better than -10 dB from 118-165 GHz and drops down to -5 dB at the edge

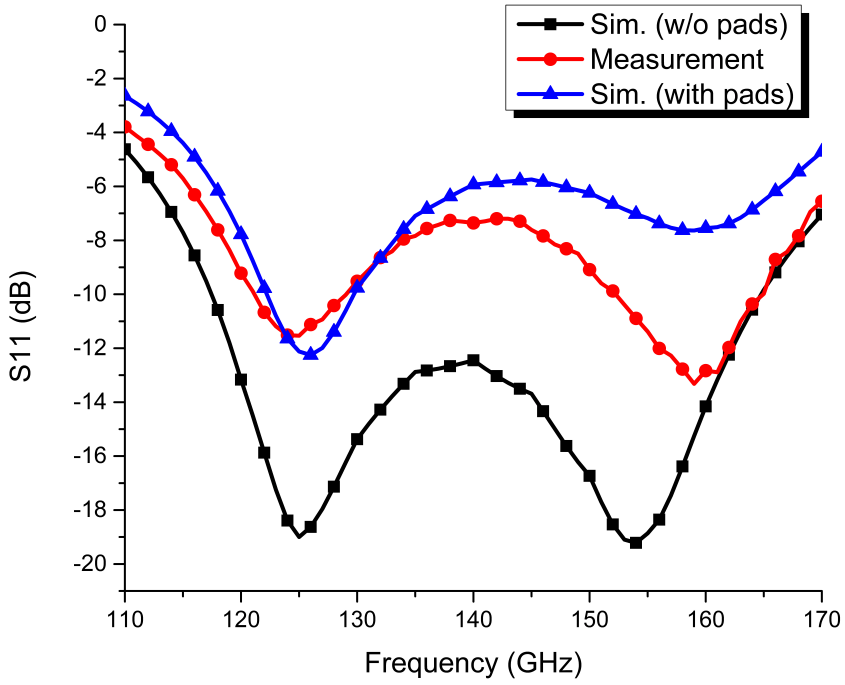

Figure 79: Simulated and measured S11 of the D-Band power detector

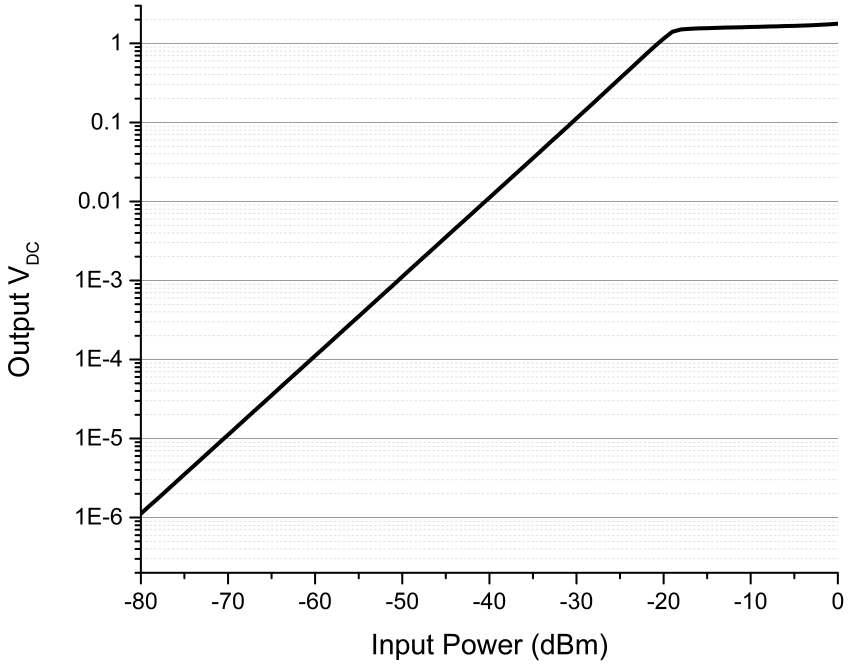

Figure 80: Simulated V_{OUT} difference vs P_{IN} of the D-Band power Detector at 140 GHz

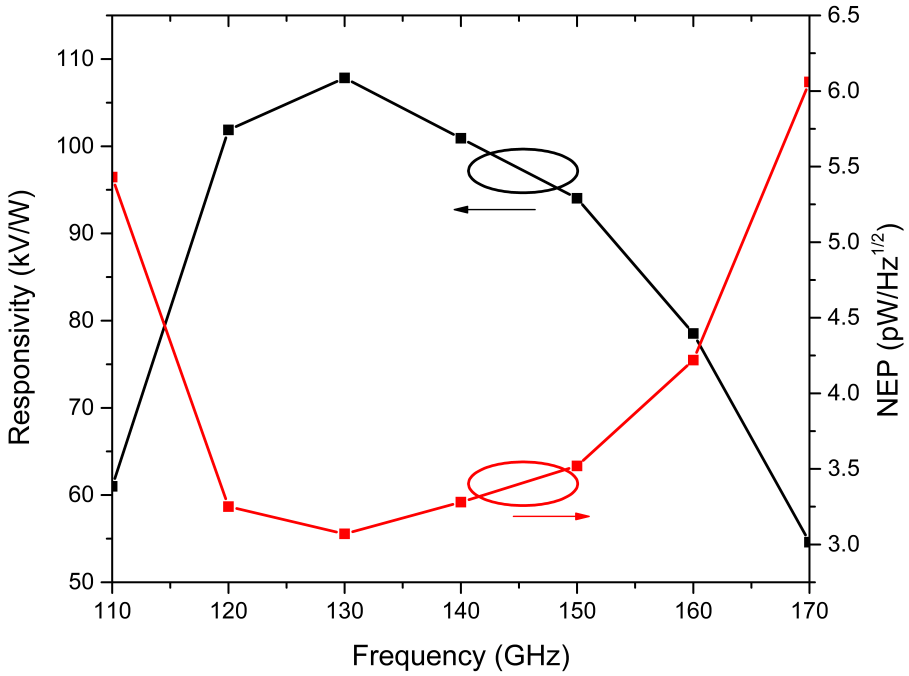

Figure 81: Simulated NEP and responsivity of the D-Band power detector

of the band which is still sufficient for responsivity to not degrade significantly. The dual stub tuning allows for 2 resonance points at 125 and 155 GHz which in return increases the matching bandwidth of the circuit. The measurements are performed at IHP's facilities with 75 μm GSG probes and 110-170 GHz frequency extenders. Measured S11 agress well with the simulation without pads except at 160 GHz, the measured S11 is better than -10 dB compared to -7 dB of simulation.

The responsivity and NEP of the circuit are illustrated in Fig. 80-81. When applied with 3.5 V V_{CC} voltage, nominally the collector voltage is around 1.5 V and it decreases as the input power decreases up until collector voltage drops down to 0.3 V which happens at -20 dBm. This value is more than enough for typical radiometer applications.The peak responsivity occurs at 130 GHz with a value of107 kV/W and the minimum value is 55 kV/W at 170 GHz thanks to the wideband matching of the circuit. Similarly, minimum NEP is 3.1 $pW/Hz^{1/2}$ at 130 GHz and it doubles at 170 GHz due to lower responsivity. The corresponding noise figure of the PD is 36 dB at 140 GHz.

Table 8 presents the performance of the PD in comparison with other SiGe power detectors at D-Band. Even though there are PDs that have lower NEPs in

Table 8: Summary of performance of the D-Band PD and comparison with the SoA SiGe PDs

	Tech.	*NEP* ($pW/Hz^{1/2}$)	Resp. kV/W	R_{LOAD} $k\Omega$	S11 <-10dB @ (GHz)	Area (mm^2)
[66]	90 nm SiGe	2.7	10.5	1	125-170	0.21
[56]	90 nm SiGe	0.7	11	0.6	145-170	0.05*
[67]	0.13 μm SiGe	10	10	1	-	N/A
This Work	**0.13 μm SiGe**	**3.1**	**107**	**20**	**118-165****	**0.37**

**Excluding pads **Simulation without pads*

the literature, this is mainly due to the technology used as well as the matching circuitry. The presented PD's NEP is still sufficiently low and it is much more suitable for wideband systems. Also the high responsivity relaxes the requirement of IF amplification after the detection stage. The designed PD is suitable to be used in the proposed D-Band radiometer systems.

4.2.2 Low Noise Amplifier

The micrograph of the designed D-Band LNA is presented in Fig. 82. The chip occupies 0.57 mm^2 (0.81 x 0.7 mm). The cascode stages draw a total of 9.6 mA of DC current from 2 V supply and CE stages draw 5.8 mA from 1.5 V supply so the total power consumption of the LNA is 28 mW.

The full chip EM simulation as well as measurement results are presented in Fig. 83-86. Without the pads, all the presented simulation results are from the reference plane which is 50 μm from the RF pads. The effect of the RF pads are left to be deembedded using the TRL fixture measurement results. The measurements are performed at IHP, using the same setup to measure the D-Band PD.

The measured input and output matching of the circuit is better than -7 dB accross the entire D-Band. The measurement also includes the effect of RF pads, therefore the matchings degrade slightly from the simulation without pads. The matchings agree well with the simulation, however the overestimated shunt capacitance of the RF pads by simulations, result in slightly closer results to simulation without pads. Both matchings are in fact, in between simulated matchings with and

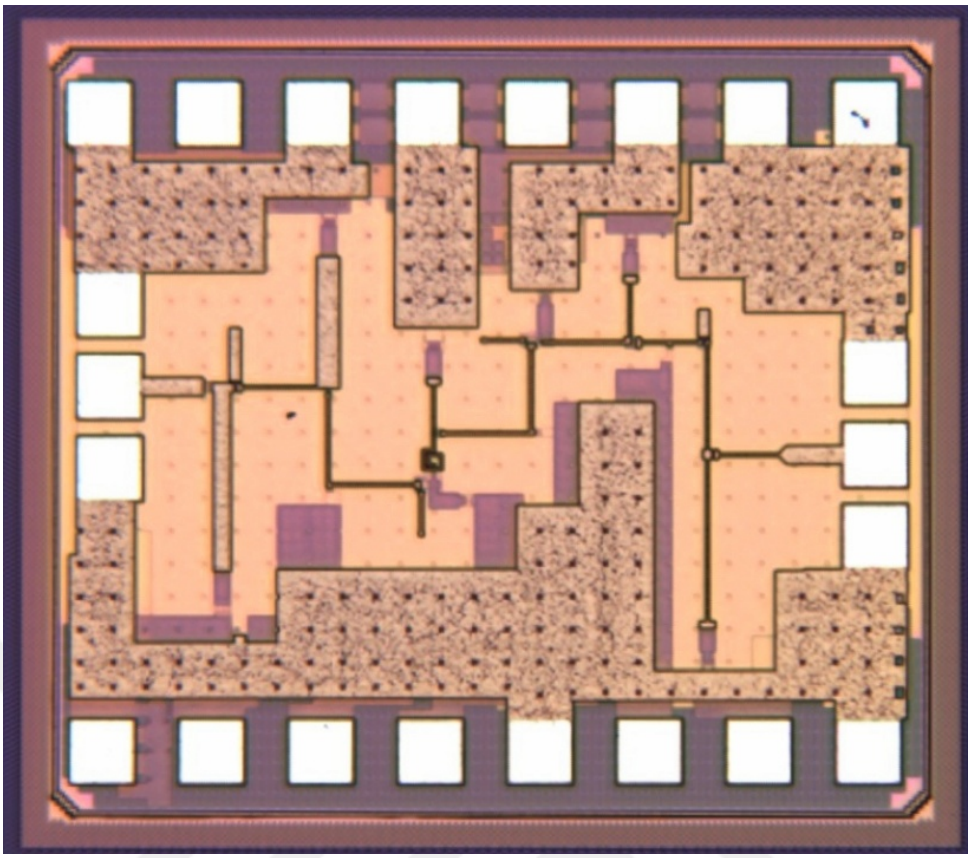

Figure 82: Layout of the designed D-Band LNA

without the pads. After deembedding, input and output matchings are expected to improve to better -10 dB as estimated by simulations.

The measured gain of the LNA is presented in Fig. 85 which also agrees relatively well with the simulations. The measured peak gain is 25 dB and the 3 dB BW of the LNA is 45 GHz (111-156 GHz). The discrepancy between the simulated and measured gain at 150 GHz is due to the cascode stages. The measurements indicate that the gain of the individual cascode stages peaked higher than expected which might be related with loads used as well as the collector currents which turned out to be higher than simulations.

The minimum NF of the chip is 6.5 dB at 130 GHz and better than 7 dB at 40 GHz bandwidth (110-150 GHz). Due to significant gain drop close to 170 GHz, NF also increases to 8.5 dB at this frequency. The effective noise bandwidth of the LNA is also calculated the same way with the W-Band and is found to be 57 GHz at D-Band.

Table 9 presents the performance of the LNA in comparison with other SiGe power detectors at D-Band. The gain of the LNA is relatively low to other SiGe

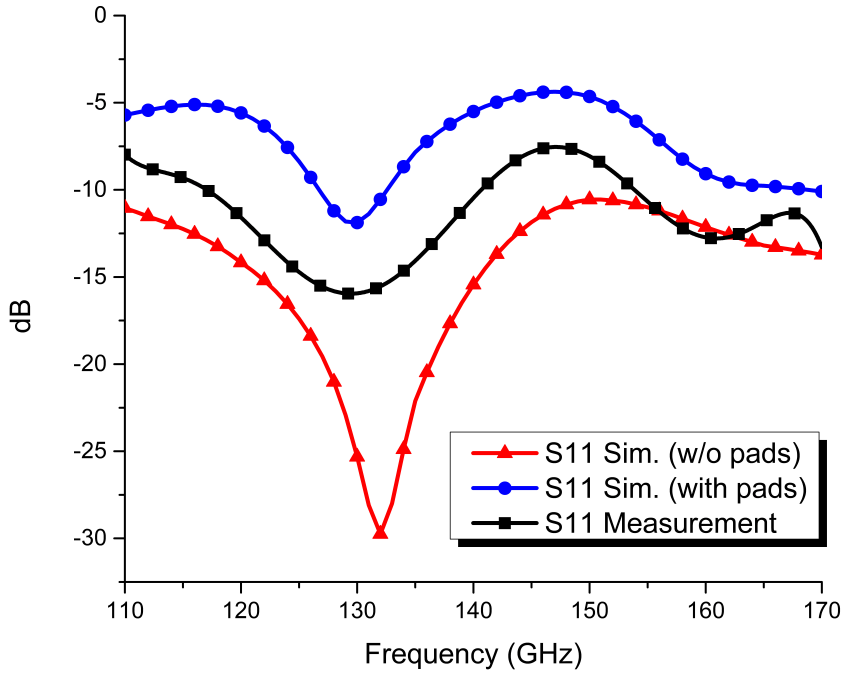

Figure 83: Simulated and measured S11 of the D-Band LNA

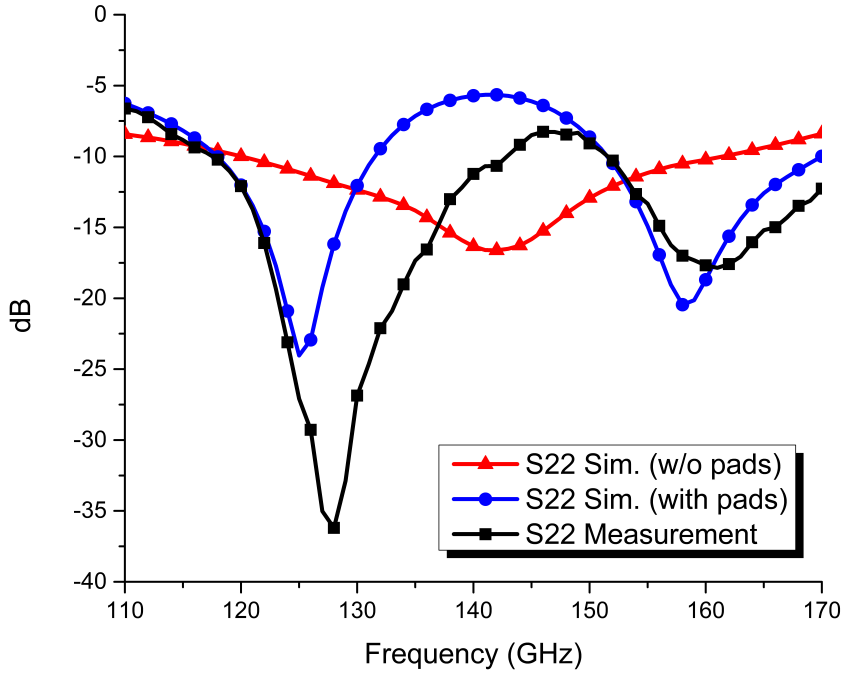

Figure 84: Simulated and measured S22 of the D-Band LNA

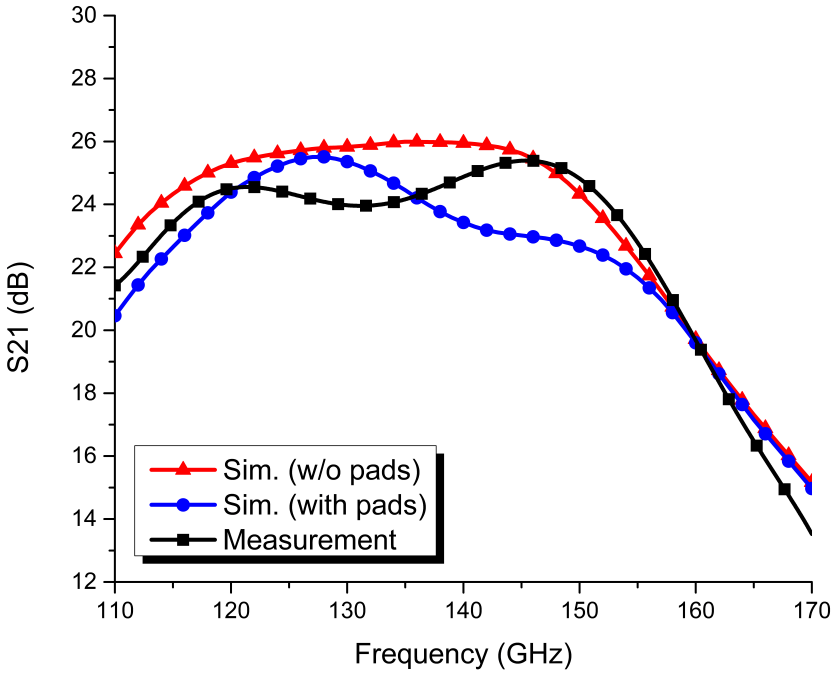

Figure 85: Simulated and measured gain of the D-Band LNA

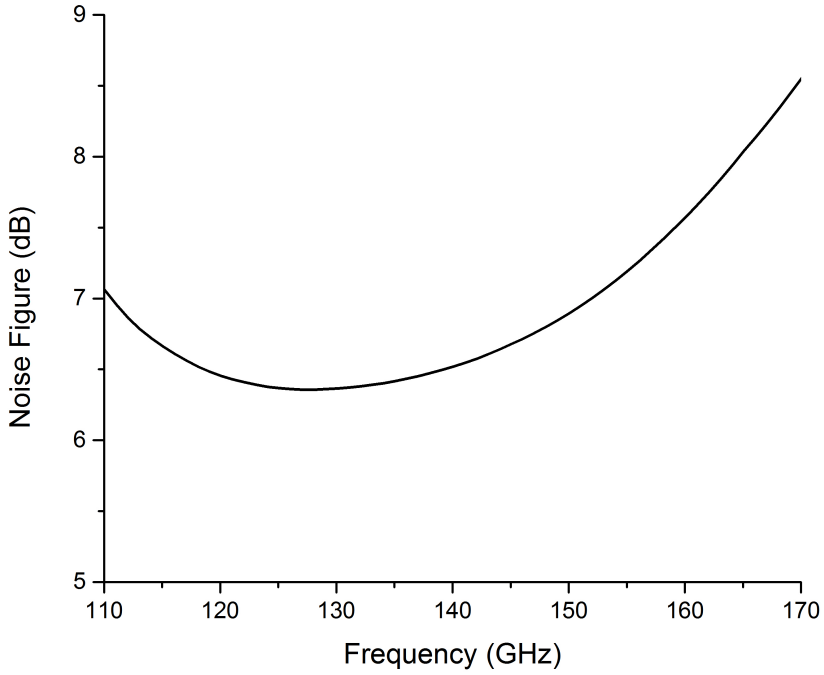

Figure 86: Simulated noise figure of the D-Band LNA

Table 9: Summary of performance of the D-Band LNA and comparison with the SoA SiGe LNAs

	Tech.	Topology	3-dB BW (GHz)	Peak Gain (dB)	NF (dB)	P_{DC} (mW)	Area mm^2
[56]	90nm SiGe	3xCC	135.5-141	36	>6.2*	45	0.36
[66]	90nm SiGe	3xCC+ 1xCE	120-145	30	6.2	45	0.41
[68]	0.13μm SiGe	2xCC	120-134	28	5.5-6.5	12	0.4
This Work	**0.13μm SiGe**	**1xCE+ 2xCC+ 1xCE**	**111-156**	**25**	**6.5**	**28**	**0.56**

**Estimated*

LNAs, nevertheless it exhibits excellent wideband performance and moderate gain especially given that the power consumption is lower than two of the LNAs presented in comparison.

4.2.3 SPDT Switch

The micrograph of the designed D-Band SPDT switch is shown in Fig. 87. The chip occupies 0.4 mm^2 (0.79 x 0.5 mm) including the pads. The S-parameters of the SPDT are measured on-wafer at IHP's facilities using a 75 μm GSG probes and frequency extenders. Since one of the ports of the SPDT switch is terminated to 50 Ω on-chip, IL and isolation states are measured by switching the bias points. Through measurements, the optimum bias voltages are found to be 1 V and 0.3 V for short and open HBTs. At this bias point, the switch draws 8 mA from 1 V supply, therefore the power consumption is 8 mW.

Fig. 88 and 89 present the measured and simulated input and output return loss of the chip at IL and isolation states. Without pads, both the S11 and S22 are simulated to be better than -14 dB, however with the effect of pads, matchings degrades to around -5 dB. The measurement results agree relatively well with the simulation results with pads and captures the overall behaviour but it is observed that the shunt capacitance estimated by simulations are higher than measurements therefore the measured S11 and S22 are better than -10 dB across the entire D-Band for the IL state. Similarly at the isolation state, the measured S11 are in between

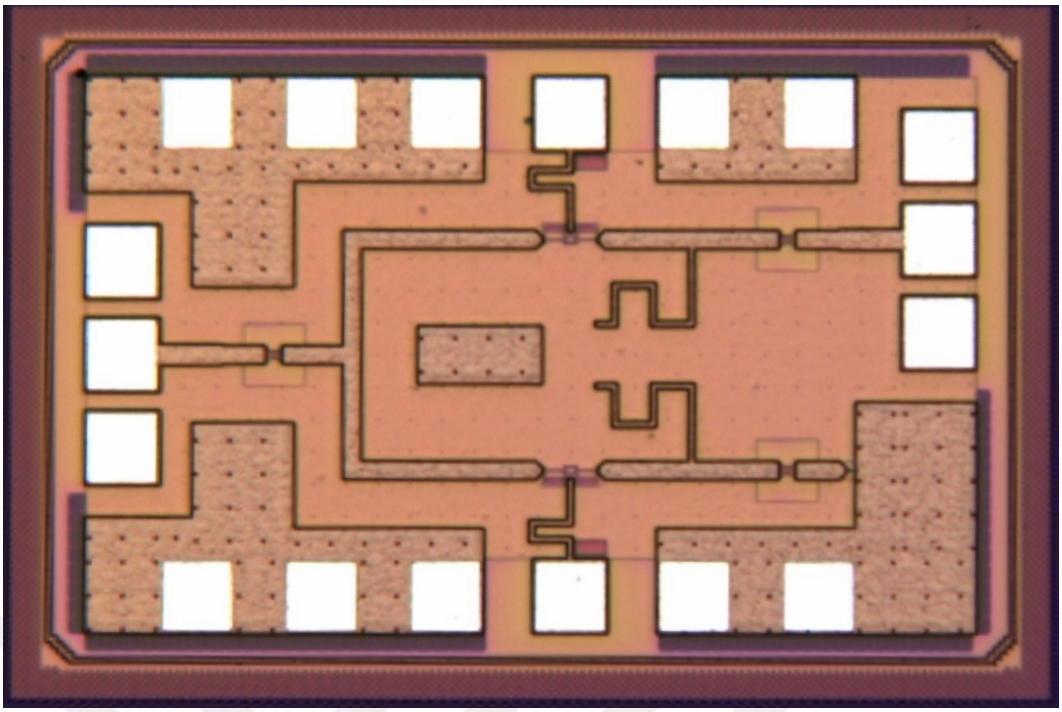

Figure 87: Micrograph of the designed D-Band SPDT switch

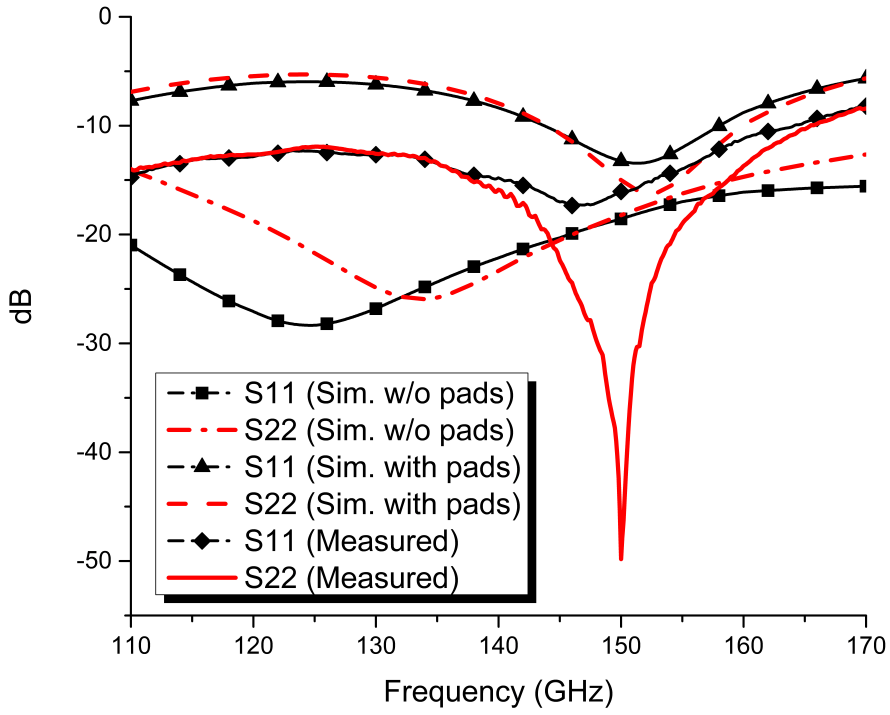

Figure 88: Simulated and measured S11 and S22 of the D-Band SPDT switch at IL state

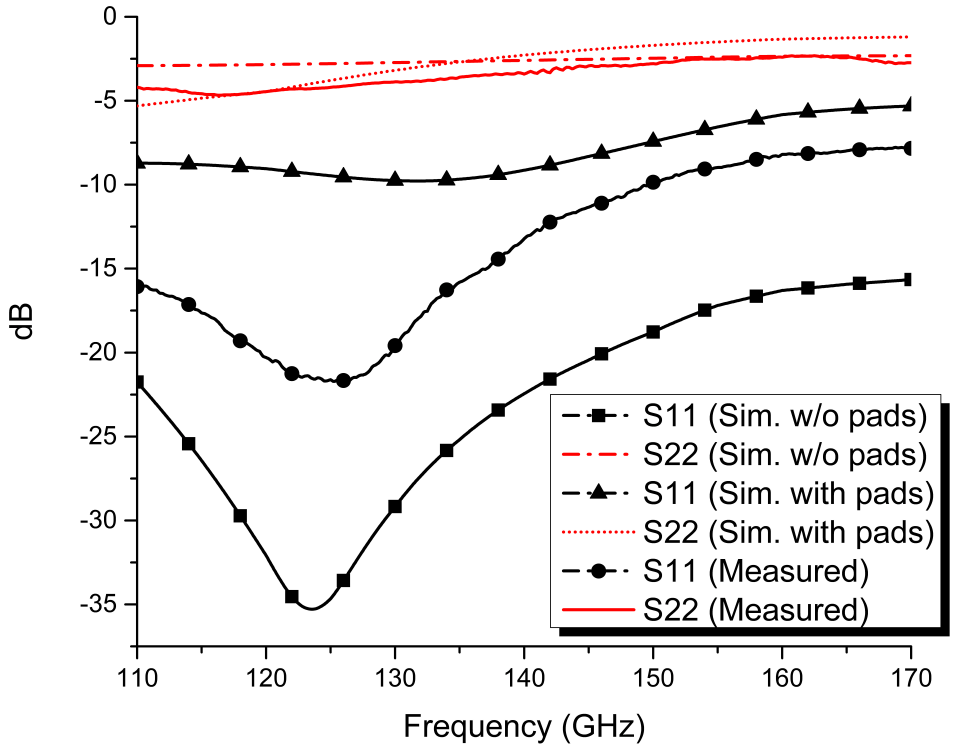

Figure 89: Simulated and measured S11 and S22 of the D-Band SPDT switch at isolation state

simulated S11 with and without pads. The behaviour is still well captured but the pad capacitances are overstimated by the simulations. Expectedly, at isolation state, the output matching is -3 to -5 dB and is better captured by simulations.

The simulated and measured IL of the SPDT switch are shown in Fig. 90. IL of the switch is again well estimated by simulations from 150 to 170 GHz. The discrepancy between the simulation and measurement at lower frequency can be attibuted to the degraded matching at these frequencies estimated by simulations. Between 120 to 130 GHz, simulated S11 is -5 to -6 dB compared to -12 to -13 dB measured. As a result the IL is overestimated by 0.5-1 dB. Without the pads, the simulated IL improves by 1-1.5 dB.

The isolation of the switch is illustrated in Fig. 91. The measured results show that isolation is better than 27 dB and is maximum at 165 GHz by 31 dB. For the isolation, the measurements do not agree well with the simulations and there is 5-7 dB difference. The reason for higher isolation is to be investigated further.

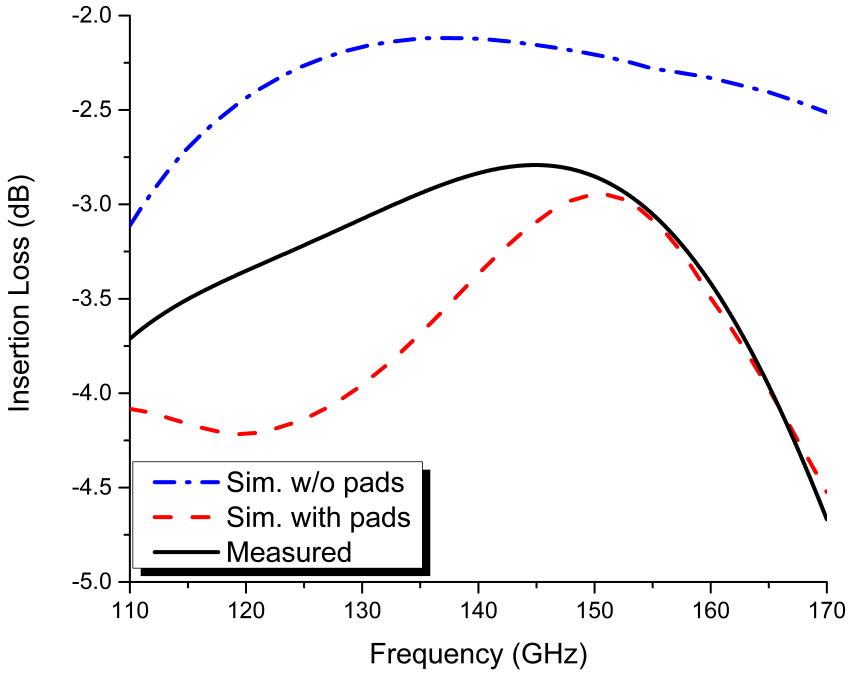

Figure 90: Simulated and measured IL of the D-Band SPDT switch

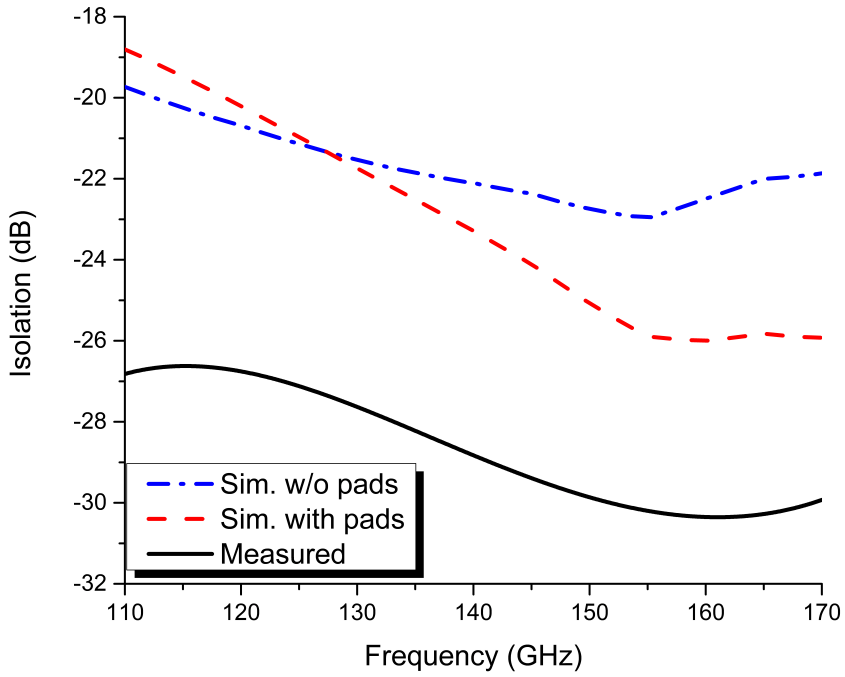

Figure 91: Simulated and measured isolation of the D-Band SPDT switch

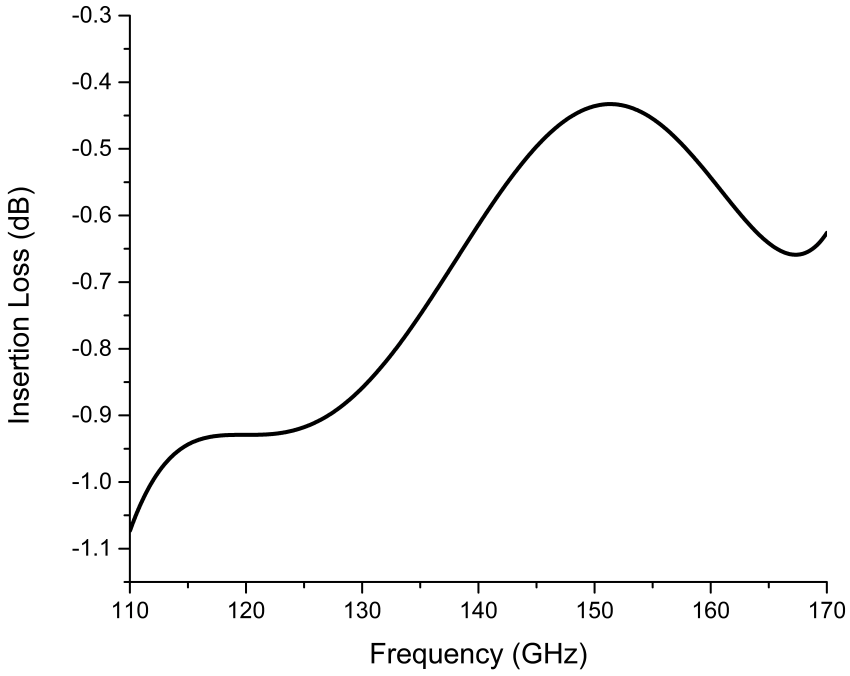

Figure 92: Measured IL of the thru fixture

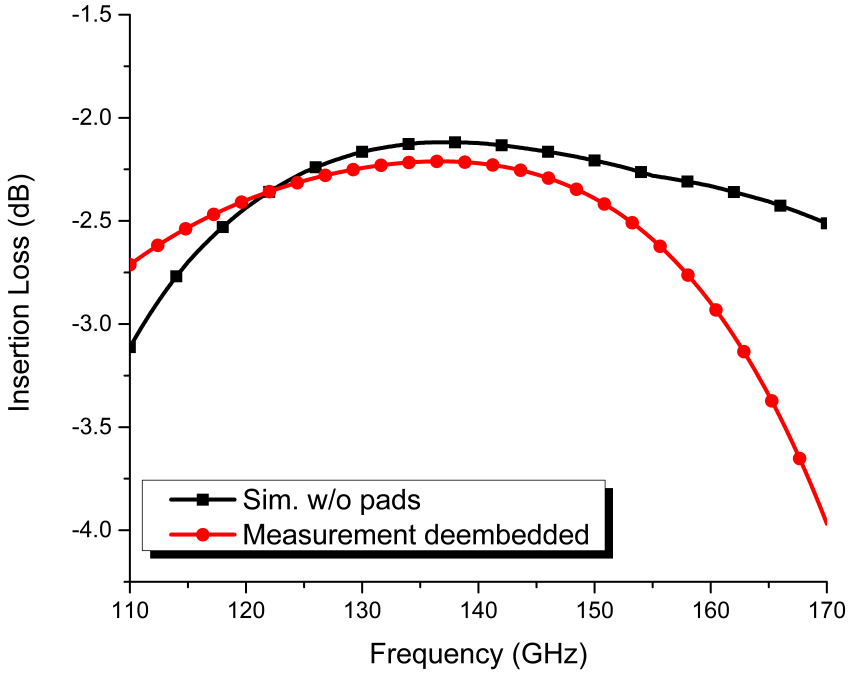

Figure 93: Simulated and deembedded measurement IL of the D-Band SPDT switch

Table 10: Summary of performance of the D-Band SPDT and comparison with the SoA SPDT switches

	Tech.	Topology	IL (dB)	Isolation (dB)	P_{DC} (mW)	Area mm^2
[69]	0.13 μm SiGe	Double-shunt HBT	2.6-3.5	23.5-29	6	0.37
[70]	32 nm CMOS SOI	Single-shunt	2.6-4	22	0	0.21
[66]	90 nm SiGe	PIN	2-2.5	15-20	N/A	0.27
[71]	0.13 μm SiGe	Rat Race Coupler	3.4-4*	33-36*	N/A	0.27
This Work	**0.13 μm SiGe**	**Single-Shunt**	**2.2-4****	**27-31**	**8**	**0.57**

**Simulated **Deembedded*

In order to deembed the effect of RF pads, the set of fixtures are also measured. The measured IL of the thru fixture which is the RF pads in addition to the 100 μm long 50 Ω TL, is shown in Fig. 92. The measurements indicate that 0.4 to 1 dB additional loss occurs due to pads and TL. Even though full deembedding of the fixture would give more reliable results, subtracting the IL of the measured thru from the measured IL of the SPDT switch would also provide roughly similar results. The deembedded measurement result in comparison with the simulated IL without pads of the SPDT switch is illustrated in Fig. 93. The results agree very well from 120 to 150 GHz and minimum IL occurs at 127 GHz by 2.2 dB. At higher frequencies, the deembedded IL drops to 4 dB, nevertheless it is better than -2.7 dB from 110 to 154 GHz.

Table 10 presents the summary of performance of the D-Band SPDT switch with other recently published D-Band SPDTs. The designed switch demonstrates state-of-the-art performance and has one of the lowest IL in the literature for D-Band. One of the drawbacks of using HBTs for switch design is the static power consumption and it is relatively high, nevertheless the SPDT switch is highly suitable for wideband radiometer applications.

4.2.4 Antenna

The D-Band antenna is simulated in ADS and the final layout work is carried out in Cadence. The layout of the antenna is shown in Fig. 94. The total area of the

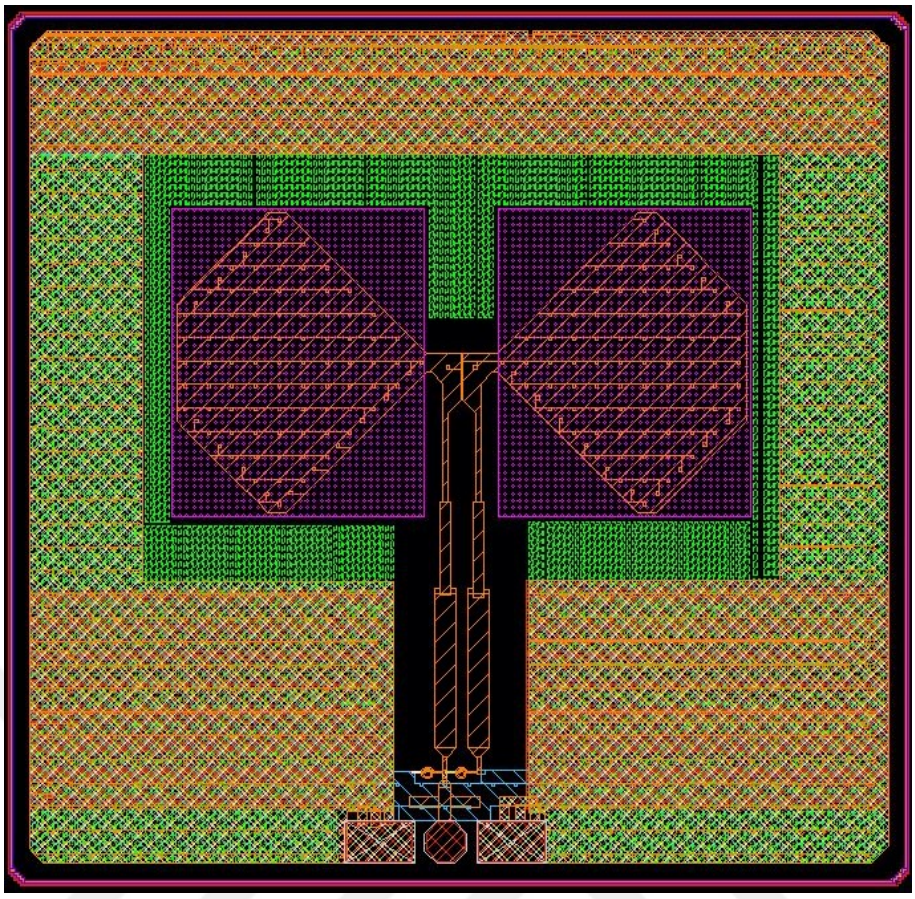

Figure 94: Layout of the designed D-Band antenna

designed antenna is 1.62 mm^2 (1.25 x 1.3 mm). Compared to W-Band antenna, the dimensions of the antenna is much smaller due to shorter wavelength. The antenna is not yet measured and the simulation results are presented in Fig. 95-96.

The antenna simulations indicate that the antenna is well matched to 50 Ω across the entire D-Band. The resonance point is at 158 GHz and S11 stays below -9.8 dB from 110 to 170 GHz. The peak efficiency occurs at lower frequency of 135-140 GHz and it is approximately %29. Accordingly, the gain also peaks at almost the same frequency and simulations show that the peak gain is 2.2 dBi. The efficiency drops to %18 at the edges of the band the gain tracks the same curve and stays above 0.7 dBi. The ADS simulations are performed assuming 370 μm silicon subtrate thickness.

Due to relatively poor agreement of measurement results and ADS simulations of the W-Band antenna, the D-Band antenna will be simulated using HFSS to verify the results.

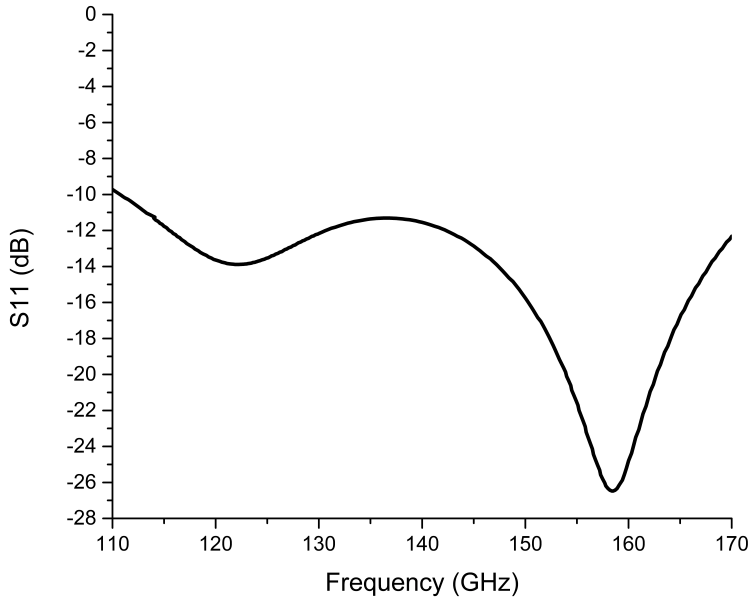

Figure 95: Simulated S11 of the D-Band antenna

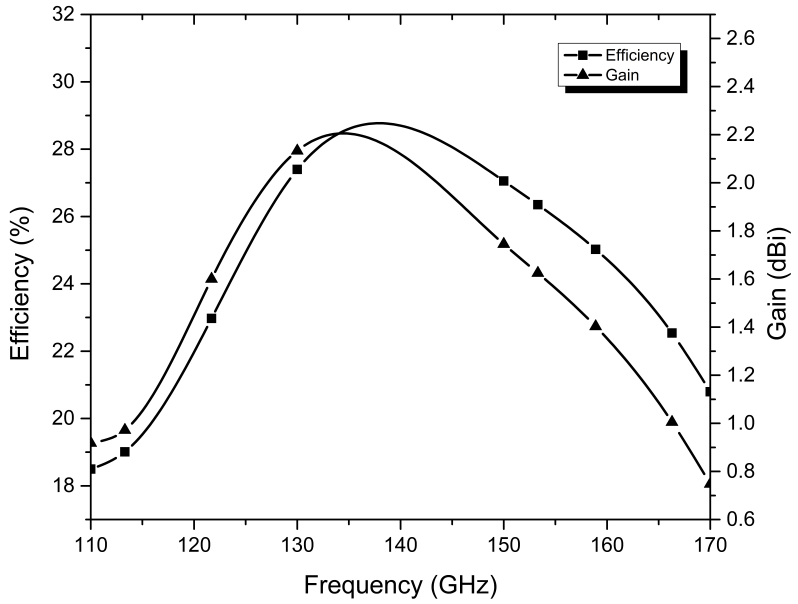

Figure 96: Simulated gain and efficiency of the D-Band antenna

4.3 Radiometer System Implementations

The designed D-Band sub-blocks of SPDT switch, LNA and PD are found to be suitable for the D-Band radiometer systems. Similar to W-Band; two radiometers, one TPR and one Dicke radiometer is implemented. Due to the problems associ-

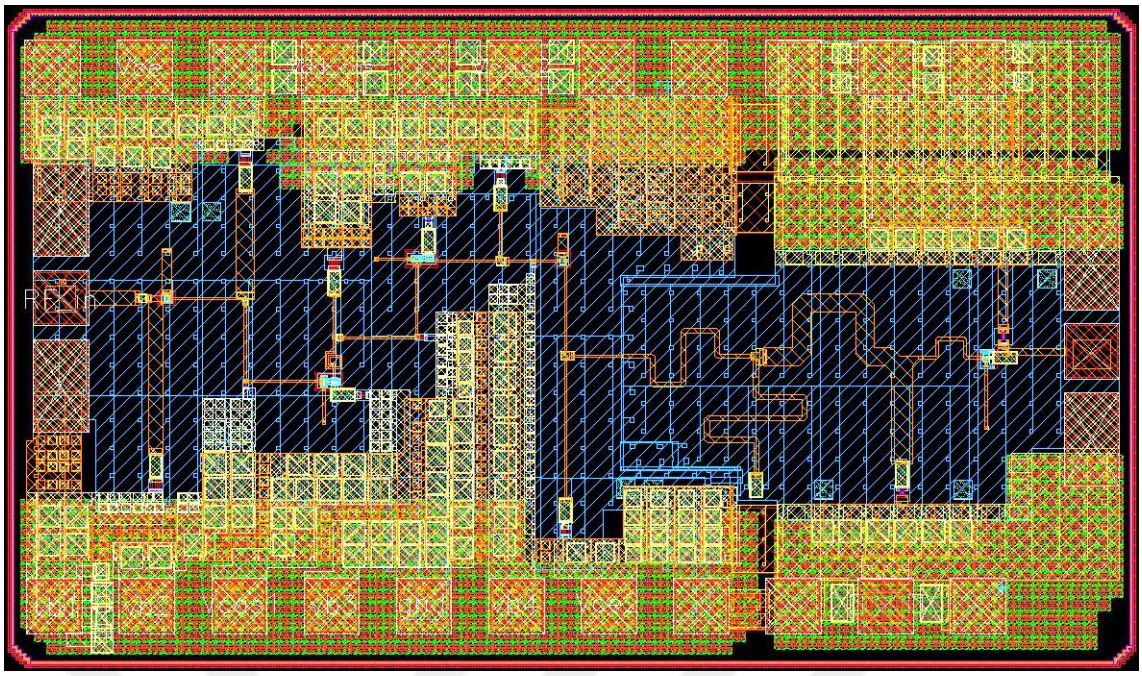

Figure 97: Layout of the implemented D-Band TPR

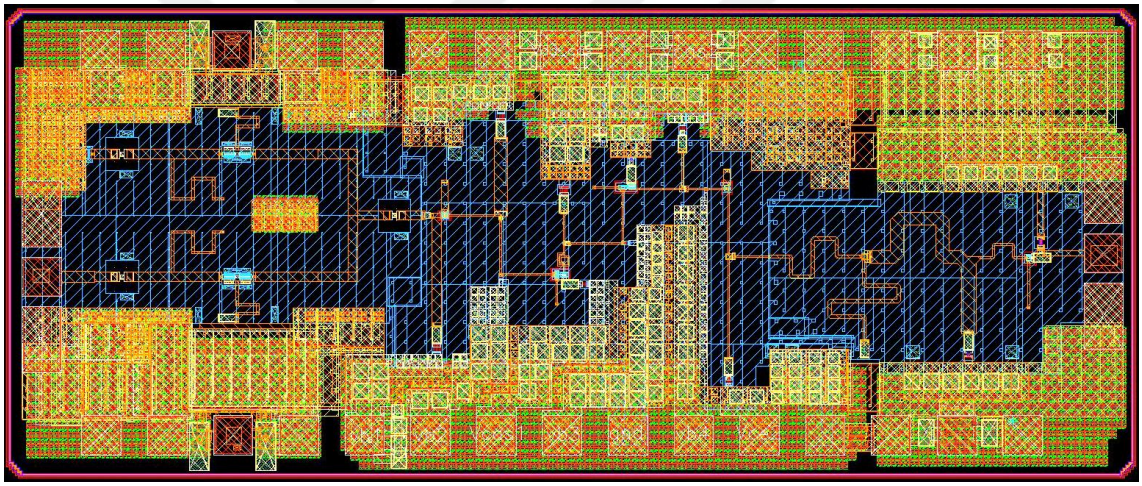

Figure 98: Layout of the implemented D-Band Dicke radiometer

ated with antenna simulations seen in W-Band, the antenna is not included in the systems. The standalone receivers are designed without any additional measures taken on the block designs. Thanks to the wideband input and output matching of the blocks, the loading effect is minimal and the performance of the blocks remains the same. The layouts of the D-Band TPR and Dicke radiometer are shown in Fig. 97-98. The TPR system occupies 0.84 mm^2 (1.2 x 0.7 mm) and consumes 28 mW of power. The Dicke radiometer occupies slightly larger area of 1.2 mm^2 (1.7 x 0.7 mm) and consumes 36 mW of power due to the addition SPDT switch.

The NETD of the radiometers are calculated based on simulation and mea-

Table 11: Summary of performance of the implemented radiometer systems and comparison with SoA D-Band radiometers

	Tech.	Topology	System Integration	P_{DC} (mW)	Area (mm^2)	NETD
[56]	90 nm SiGe	TPR**	Front-end	47	0.52	0.25*
[67]	0.13 μm SiGe	TPR**	Front-end	95	0.37	0.35*
[72]	6 5nm CMOS	Dicke	Front-end	152	0.5	1.5
This Work	**0.13 μm SiGe**	**TPR****	**Front-end**	**28**	**0.84**	0.24
This Work	**0.1 3μm SiGe**	**Dicke**	**Front-end**	**36**	**1.2**	0.42

**3.125 ms integration time, rest are 30 ms **Assumed external calibration*

surement results of the blocks. Assuming external calibration and factoring in the penalty of 2 due to calibration, the TPR achieves 0.24 K. The Dicke radiometer on the other hand, is calculated to have an NETD of 0.42 K due to the relatively significant IL of the SPDT switch.

Table 11 presents the performance of summary of the implemented D-Band TPR and Dicke radiometers. In comparison with the state-of-the-art D-Band radiometers designed in silicon based technologies, the systems achieve competitive performance in relatively low power consumption. The receivers are suitable to be used in highly integrated and sensitive radiometer systems.

5 Conclusion & Future Work

5.1 Summary of Work

Mm-wave ICs are rapidly evolving to meet the demanding requirements of arising applications ranging from communication systems to imaging arrays. One the most active research areas in mm-wave IC design is passive imaging systems operating at W&D-Band due to the unique properties of mm-wave propagation as well as the incredible advancements in IC technologies. Consequently, critical applications such as concealed weapon detection and low visibility navigation and various others can be enabled through high performance mm-wave ICs. High level of integration, low manufacturing cost, high sensitivity, small area and low power consumption are all required to realize next generation mm-wave IC systems. Therefore system-on-chip (SoC) solutions are becoming highly desired. SiGe BiCMOS technology has advanced tremendously over the couple of years and is a great candidate to implement high performance ICs. The f_t and f_{max} of the SiGe HBTs are catching up in performance to III-IV technologies which were the undisputed choice for mm-wave ICs until recently. The high level of integration offered of the SiGe BiCMOS technology along with the cost advantage and similar performance compared to III-IV technologies are advantages that highlight it as a suitable choice to realize mm-wave radiometers.

The aim of this thesis is to realize W&D-Band radiometers using IHPs 0.13 μm SiGe BiCMOS technology featuring HBTs with f_t/f_{max} of 300/450 GHz. Several radiometers architectures are investigated in Chapter 2 and sub-block designs of each radiometer are presented in Chapter 3 and 4. Total power radiometers and Dicke radiometers are designed at W-Band and D-Band. All of the systems are integrated with on-chip antennas that utilize local backside etching process. Sub-blocks of these radiometers; SPDTs, LNAs and power detectors are designed, fabricated and measured. Also, a novel dual receiver architecture is proposed which theoretically improves radiometer sensitivity by $\sqrt{2}$. A unique SPDT tree is designed to realize dual channel radiometer.

In Chapter 3, W-Band radiometer design is presented. The W-Band 4 stage common-emitter LNA has a measured peak gain of 22.5 dB, 75-110 GHz matching

bandwidth and an effective noise bandwidth of 37 GHz while only consuming 8 mW. The simulated NF of the LNA is 4.5 dB. The fabricated W-Band microstrip $\lambda/4$ shunt switching SPDT, utilizing reverse satured HBTs has a measured insertion loss of 3.5-4 dB. Therefore a new version of the W-Band SPDT is designed. This version has a simulated minimum IL of 1.6 dB without the RF pads and maximum of 2 dB between 70-110 GHz thanks to the wideband matching of the circuit. The simulated isolation of the SPDT is also better than 19 dB across the band. A W-Band power detector is designed using an HBT which is biased at the edge of active region and a buffer transistor. 100 $k\Omega$ load resistor is used to improve the NEP and the responsivity of the detector. Input matching is measured and it is better than -10 dB between 80-108 GHz. The simulated peak responsivity is 960 kV/W and minimum NEP of 0.28 $pW/Hz^{1/2}$. The W-Band bow-tie antenna with LC balun is fabricated in the BEOL run and measured on-wafer. The antenna is well matched to 50 Ω between 81-96 GHz which is verified by the measurements. The HFSS simulations indicate that -4 to -1 dBi gain is achieved by the antenna.

Using the designed W-Band blocks a total power radiometer and a Dicke radiometer is implemented. The NETD of the radiometers are calculated using the simulated and measured results of the W-Band sub-blocks. Assuming external calibration, the TPR achieves 0.21 K of NETD, however it is increased to 1.6 K without any calibration. The power consumption of the TPR is only 8 mW and occupies 3.23 mm^2 of area. The Dicke radiometer on the other hand, has 0.33 K of NETD with 12.8 mW power consumption and occupies 4.17 mm^2.

The proposed dual receiver architecture is implemented using the W-Band blocks. This architecture features two identical receivers that alternates between the reference load and the antenna at the opposite calibration cycles. As a result, the output SNR improves by $\sqrt{2}$. The area of the system does not increase significantly due to the presence of the on-chip antenna. The required switch tree implementation is realized with a unique shunt HBT sharing method which results in only 0.7 dB of increase in the IL and no significant degradation in terms of isolation. The area of the chip is 4.2 mm^2 and consumes a total of 20 mW. The calculated NETD of the system is 0.27 K. The improvement is %10-%20 compared to the Dicke radiometer, depending on the IL of the SPDT switch.

In Chapter 4, D-Band radiometer design is presented. The D-Band LNA is designed using a CE-cascode-cascode-CE topology to improve the gain to compensate for the increased noise of the detector. The LNA has a measured peak gain of 25 dB and simulated 6.5 dB NF while consuming 28 mW. The 3 dB bandwidth of the LNA is 45 GHz and noise bandwidth is calculated to be 57 GHz. The input and output return loss of the LNA is better than -7 dB across the entire D-Band including the RF pads. The power detector is designed using an HBT with collector RF shorted similar to W-Band PD. 20 $k\Omega$ load is chosen for this design. The simulated peak responsivity is 107 kV/W and NEP is minimum at 130 GHz with a value of 3.1 $pW/Hz^{1/2}$. The matching bandwidth of the circuit is improved through the use of double stub matching and it is simulated to be better than -10 dB between 118 and 165 GHz. With the pads, matchings degrade to -7 dB, however after deembedding, matchings are expected to improve above -10 dB. The D-Band SPDT uses the same topology as the W-Band. The measured minimum IL of the SPDT is 2.8 dB and isolation is 27-31 dB across the entire D-Band including the effect of the RF pads. After deembedding of the RF pads, the minimum IL improves by 0.4-1 dB so the minimum IL of the SPDT switch becomes 2.2 dB. The D-Band antenna also utilizes LBE process and is implemented as a bow-tie antenna with tapered edges to improve the bandwidth. Differential to single ended conversion is done with an LC balun. ADS simulation results show that S11 of the antenna is better than -10 dB between 110-170 GHz and the gain is 1-2 dBi.

The designed D-Band blocks are used to implement D-Band TPR and Dicke radiometer. The on-chip antenna is not included in the receivers. The TPR system occupies 0.84 mm^2 and consumes 28 mW of power whereas the Dicke radiometer occupies 1.2 mm^2 and consumes 36 mW of power. The NETD of the Dicke radiometer is calculated to be 0.42 K and 0.24 K for TPR assuming external calibration.

The designed W&D-Band radiometers demonstrate state-of-the-art performance with minimal power consumption and wide bandwidth. Compared to recent literature on mm-wave radiometers in silicon based technologies, the designed radiometers achieve better than 0.5 K, while consuming much lower power and offering higher level of integration.

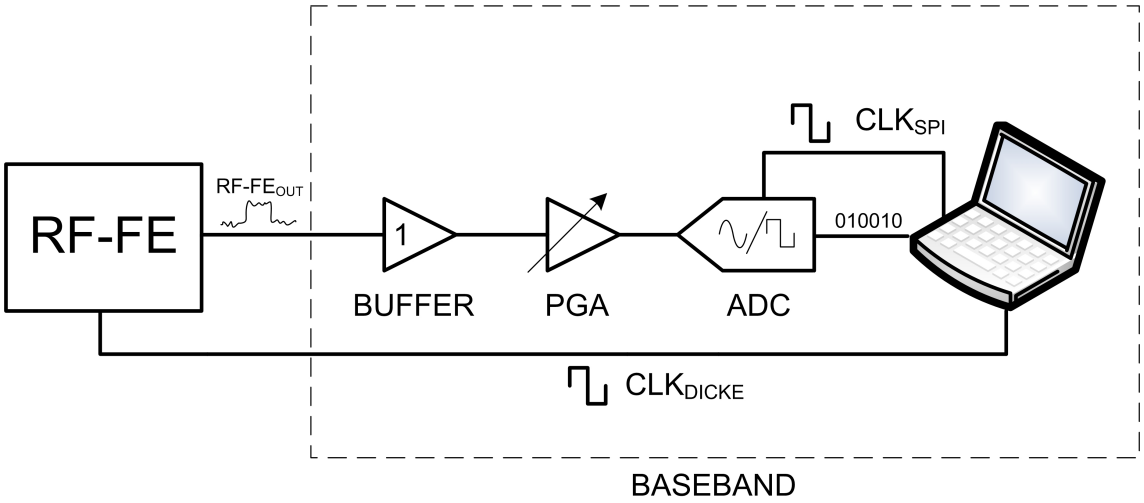

Figure 99: The block diagram of a possible digital baseband implementation

5.2 Future Work

In terms of sub-blocks of the radiometers, minor redesigns have the potential to enhance the NETD even further. Even though all the designed sub-blocks are operational and achieve decent performance, the room for improvement is present in all the blocks. Especially the gain of the W-Band LNA could be increased to 25-30 dB which in return would decrease the NETD to 0.15-0.2 K range. The input matching of the D-Band PD is relatively lossy which degrades the NEP. Instead of matching the output of the D-Band LNA to 50 Ω, conjugate matching would mitigate the additional losses of the matching network. Similarly, the gain of the D-Band LNA could also be improved to 30 dB or more to compensate for the high NEP of the PD. One of the major problems in the system implementations is the antenna design. The performance of the antennas are significantly over estimated by ADS and HFSS is found to agree better with the measurements. The efficiency of both of the antennas are quite low for a backside etched antenna, therefore the gains are quite low as well. Redesign of the antennas are required to achieve better system response.

The remaining work include the baseband and array designs. For the baseband, two different approach is possible. First approach is buffering and amplifying the output signal of the PD and converting it to digital signal through an ADC as shown in Fig. 99. The digital signal is transferred to a computer so the demodulation and the integration of the signal can be done in digital domain using the synchronized

Dicke switching signal. This approach is better suited to characterizing the system due to its ease of implementation. The buffering and amplification as well as the digital conversion can all be done externally and the rest is done through a computer. Ultimately though, the baseband can all be included in the chip for extreme integration. In that case, on-chip op-amps to buffer and amplify the output signal is required. Also, analog demodulation and integration can be a better option which would relax the performance requirements of the ADC.

Next, is the characterization of the single pixels. Before taking an using the designed systems, it is neccessary to obtain single pixel NETD measurements. Such measurements can be done using either an external noise source for the systems without an antenna or calibrated temperature scenes (such as liquid nitrogen) for the systems with an antenna. In both cases the required measurements are Y-factor and total responsivity measurements. Y-factor measurements can be done using an hot and cold sources (turning on/off noise source or switching between different temperature scenes) which would give information on the system temperature. Using the total responsivity for estimating the RF bandwidth, and assuming integration time the NETD can be driven for the systems. Such measurement do not require baseband operation and can be completed in a relatively easy manner. Constructing an image using a single pixel is much more demanding using a single pixel. An example imaging setup using a single pixel receiver is illustrated in Fig. 100. In this example, since there is no integrated antenna, an external W-Band horn antenna is used, however this is not required since our systems have already on-chip antenna, althouth it might still be usefull to take images with an external antenna to observe the effect of the antenna on the image quality. Additional optics are required to focus the antenna to adjust the spatial resolution of the system and the distance of the scene. Since single pixel is used, a mechanical scanning is required. Either the receiver can be moved through double axes if the whole system is constructed on a circuit board, or the scene/object can be moved without moving the receiver. In both cases, the output data of the receiver (after baseband and usually with an ADC) can be picked up by a PC and mapped into an image using the measurement output and data coordinates. Using multiple pixels is the same, but only requires less mechanical adjusting. In the illustrated system, the object is "illuminated"

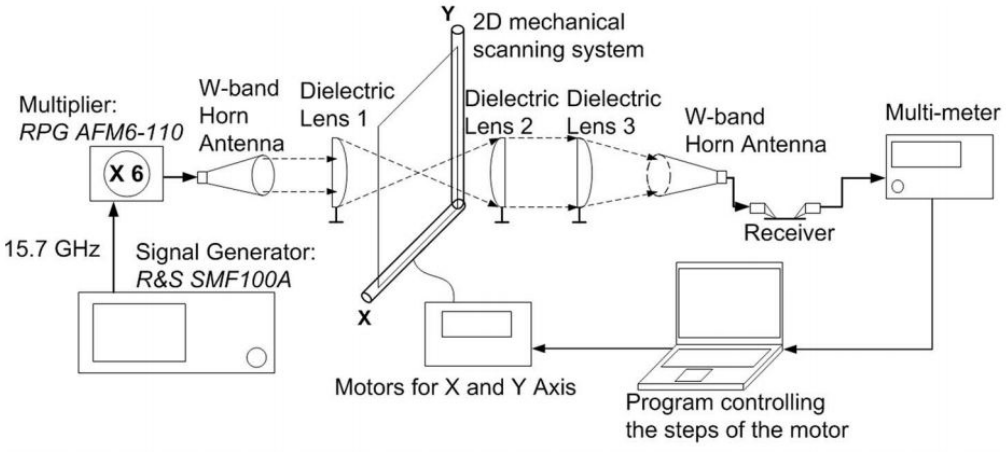

Figure 100: An example block diagram of the setup to obtain 2D image using a single receiver and antenna [13]

thorugh an external signal source and an antenna to enhance the quality of the image, however, depending on the system sensitivity, it is not required to illuminate the target other than the surrounding objects or the background temperature.

Final step of the system implementation is the FPA design. Using the single pixel receivers, $2x2$ or $4x4$ pixel arrays would be necessary to demonstrate the complete performance of the designed radiometer receivers.

Appendix

A Appendix

In this section MATLAB code for calculating NETD for given parameters is presented. g_1 is S21 of the SPDT switch in dB, g_2 is the LNA gain in dB, f_2 is the NF of the LNA in dB, and f_3 is NF of the PD in dB. tau specifies the integration time in seconds and B is the effective noise bandwidth of the system. The NETD is calculated at 290 K temperature and assuming the antenna noise temperature to be the same. Finally a factor of 2 is placed for NETD to take calibration into account.

```
T0=290;
g_1=-2.2; %db
% g_2=10:1:30; %db
g_2=26;
G1=10.^(g_1/10);
G2=10.^(g_2/10);
f_1=-g_1;
f_2=6.5; %db
f_3=37;%db
F1=10^(f_1/10);
F2=10^(f_2/10);
F3=10^(f_3/10);
Te1=T0*(F1-1);
Te2=T0*(F2-1);
Te3=T0*(F3-1);
Te=Te1+Te2/G1+Te3./(G1.*G2);
tau=30e-3;
B=57e9;
Ts=T0;
NEDT=2*(Ts+Te)/sqrt(B*tau);
```

References

[1] EUMETSAT, "Sea surface temperature." http://www.eumetsat.int/website/home/Sentinel3/SeaSurfaceTemp/index.html, January 2016.

[2] P. W. Gaiser, K. M. S. Germain, E. M. Twarog, G. A. Poe, W. Purdy, D. Richardson, W. Grossman, W. L. Jones, D. Spencer, G. Golba, J. Cleveland, L. Choy, R. M. Bevilacqua, and P. S. Chang, "The WindSat spaceborne polarimetric microwave radiometer: sensor description and early orbit performance," *IEEE Transactions on Geoscience and Remote Sensing*, vol. 42, pp. 2347–2361, Nov 2004.

[3] LockheedMartin, "AN/TPS-59(V)3 Tactical Missile Defense Radar." http://www.lockheedmartin.com/content/dam/lockheed/data/ms2/documents/ground-based-air-surveillance/TPS59_brochure.pdf.

[4] R. Martin, C. Schuetz, T. Dillon, D. Mackrides, P. Yao, K. Shreve, C. Harrity, A. Zablocki, B. Overmiller, P. Curt, J. Bonnett, A. Wright, J. Wilson, S. Shi, and D. Prather, "Optical up-conversion enables capture of millimeter-wave video with an IR camera," *SPIENewsroom*, 2012.

[5] L. Yujiri, M. Shoucri, and P. Moffa, "Passive millimeter wave imaging," *IEEE Microwave Magazine*, vol. 4, pp. 39–50, Sept 2003.

[6] M. Sholley, G. Barber, R. Raja, and C. Jackson, "Advanced MMIC radiometers," in *Microwave Conference, 2000 Asia-Pacific*, pp. 94–98, 2000.

[7] Z. Chen, C. C. Wang, H. C. Yao, and P. Heydari, "A BiCMOS W-Band 2x2 Focal-Plane Array With On-Chip Antenna," *IEEE Journal of Solid-State Circuits*, vol. 47, pp. 2355–2371, Oct 2012.

[8] J. D. Cressler, *Silicon Heterostructure Devices*. Florida: CRC Pres, Taylor & Francis Group, 2005.

[9] Sun.org, "Electromagnetic spectrum." http://www.sun.org/encyclopedia/electromagnetic-spectrum, August 2014.

[10] R. Nave, "Rayleigh-Jeans vs Planck." http://hyperphysics.phy-astr.gsu.edu/hbase/mod6.html.

[11] J. Nanzer, *Microwave and Millimeter-wave Remote Sensing for Security Applications*. Artech House Remote Sensing Library, Artech House, 2012.

[12] M. Peichl, S. Dill, M. Jirousek, and H. Süss, "Microwave Radiometry - Imaging Technologies and Applications," in *Wave Propagation in Communication, Microwaves Systems and Navigation (WFMN)*, pp. 75–83, 2007.

[13] X. Bi, M. A. Arasu, Y. Zhu, and M. Je, "A Low Switching-Loss W-Band Radiometer Utilizing a Single-Pole-Double-Throw Distributed Amplifier in 0.13-μm SiGe BiCMOS," *IEEE Transactions on Microwave Theory and Techniques*, vol. 64, pp. 226–238, Jan 2016.

[14] J. D. Cressler and N. Guofu, *Silicon-Germanium Heterojunction Bipolar Transistors*. Boston, London: Artech House, 2005.

[15] H. Meikle, *Modern Radar Systems*. Artech House radar library, Artech House, 2001.

[16] R. Loudon, *The Quantum Theory of Light*. Oxford science publications, OUP Oxford, 2000.

[17] J. Palmer and B. Grant, *The Art of Radiometry*. SPIE Press monograph, SPIE Press, 2010.

[18] F. Ulaby, D. Long, W. Blackwell, C. Elachi, and K. Sarabandi, *Microwave Radar and Radiometric Remote Sensing*. University of Michigan Press, 2014.

[19] C. on Assessment of Security Technologies for Transportation National Research Council Division on Engineering and P. Sciences, *Assessment of Millimeter Wave and Terahertz Technology for Detection and Identification of Concealed Explosives and Weapons*. Washington, US: National Academies Press, 2007.

[20] K. Narayanan and R. V. Bhonsle, "Microwave solar radiometer at 2800 MHz," *Proceedings of the Indian Academy of Sciences - Section A*, vol. 74, no. 3, pp. 142–151, 1971.

[21] R. Zimmermann, T. Rose, and T. Crowe, "An All Solid-State 1 THz Radiometer For Space Applications," in *Sixth International Symposium on Space Terahertz Technology*, p. 13, Mar. 1995.

[22] S. J. Dudzinsky, "Atmospheric Effects on Terrestrial Millimeter-Wave Communications," in *Microwave Conference, 1974. 4th European*, pp. 197–201, Sept 1974.

[23] R. W. Haas, "MMIC based MMW radiometers for remote sensing," in *Microwave Symposium Digest, 1999 IEEE MTT-S International*, vol. 1, pp. 399–402 vol.1, June 1999.

[24] J. Tuovinen, N. Hughes, P. Jukkala, P. Kangaslahti, T. Karttaavi, P. Sjoman, and J. Varis, "Technology for millimetre wave radiometers," in *Microwave Conference, 2003. 33rd European*, vol. 2, pp. 883–886 vol.2, Oct 2003.

[25] C. T. Coen, J. R. Piepmeier, and J. D. Cressler, "Integrated silicon-germanium electronics for CubeSat-based radiometers," in *2013 IEEE International Geoscience and Remote Sensing Symposium - IGARSS*, pp. 1286–1289, July 2013.

[26] Q. J. Gu, Z. Xu, H. Y. Jian, and M. C. F. Chang, "A CMOS fully differential W-band passive imager with < 2 K NETD," in *2011 IEEE Radio Frequency Integrated Circuits Symposium*, pp. 1–4, June 2011.

[27] C. T. Coen, A. Çağrı Ulusoy, R. L. Schmid, and J. D. Cressler, "Development of silicon-germanium circuits for high-frequency small satellite-based integrated radiometers," in *Radio Science Meeting (USNC-URSI NRSM), 2014 United States National Committee of URSI National*, pp. 1–1, Jan 2014.

[28] J. D. Cressler, "Device-to-circuit interactions in SiGe technology: Challenges and opportunities," in *2014 IEEE Bipolar/BiCMOS Circuits and Technology Meeting (BCTM)*, pp. 45–55, Sept 2014.

[29] J. S. Rieh, B. Jagannathan, H. Chen, K. T. Schonenberg, D. Angell, A. Chinthakindi, J. Florkey, F. Golan, D. Greenberg, S. J. Jeng, M. Khater, F. Pagette, C. Schnabel, P. Smith, A. Stricker, K. Vaed, R. Volant, D. Ahlgren, G. Freeman, K. Stein, and S. Subbanna, "SiGe HBTs with cut-off frequency of 350 GHz," in *Electron Devices Meeting, 2002. IEDM '02. International*, pp. 771–774, Dec 2002.

[30] I. Kalyoncu, "SiGe BiCMOS 4-bit Phase Shifter and T/R Module for X-band Phased Arrays," *(Master Dissertation), Sabanci University*, Summer, 2013.

[31] G. Kramm and N. Mölders, "Planck's blackbody radiation law: Presentation in different domains and determination of the related dimensional constants," *ArXiv e-prints*, Jan. 2009.

[32] M. Kutner, *Astronomy: A Physical Perspective*. Cambridge University Press, 2003.

[33] C. Smithells, *Metals Reference Book*. Elsevier Science, 2013.

[34] G. Joseph, *Fundamentals of Remote Sensing*. Universities Press, 2005.

[35] D. Staelin, "Chapter 2: Detection." `http://ocw.mit.edu/courses/electrical-engineering-and-computer-science/6-661-receivers-antennas-and-signals-spring-2003/readings/ch2new.pdf`, 2003.

[36] H. Kazemi, G. Nagy, L. Tran, E. Grossman, E. R. Brown, A. C. Gossard, G. D. Boreman, B. Lail, A. C. Young, and J. D. Zimmerman, "Ultra sensitive ErAs/InAlGaAs direct detectors for millimeter wave and THz imaging applications," in *2007 IEEE/MTT-S International Microwave Symposium*, pp. 1367–1370, June 2007.

[37] H. Kazemi, C. Nguyen, B. Brar, G. Rebeiz, G. Nagy, L. Tran, A. Young, and E. R. Brown, "Low cost modular integrated horn antenna array using heterojunction barrier diode detectors," in *Microwave Symposium Digest, 2008 IEEE MTT-S International*, pp. 297–300, June 2008.

[38] J. Richter, D. Notel, F. Kloppel, J. Huck, H. Essen, and L. p. Schmidt, "A Multi-Channel Radiometer with Focal Plane Array Antenna for W-Band Passive Millimeterwave Imaging," in *2006 IEEE MTT-S International Microwave Symposium Digest*, pp. 1592–1595, June 2006.

[39] P. J. Rice, M. Black, D. Li, J. Yip, and J. McNicol, "Development of a low cost 94ghz imaging receiver using multilayer Liquid Crystal Polymer technology," in *Physics and Engineering of Microwaves, Millimeter and Submillimeter Waves (MSMW), 2010 International Kharkov Symposium on*, pp. 1–1, June 2010.

[40] M. S. Hersman and G. A. Poe, "Sensitivity of the Total Power Radiometer with Periodic Absolute Calibration," *IEEE Transactions on Microwave Theory and Techniques*, vol. 29, pp. 32–40, Jan 1981.

[41] H. P. Moyer, J. J. Lynch, J. N. Schulman, R. L. Bowen, J. H. Schaffner, A. K. Kurdoghlian, and T. Y. Hsu, "A Low Noise Chipset for Passive Millimeter Wave Imaging," in *2007 IEEE/MTT-S International Microwave Symposium*, pp. 1363–1366, June 2007.

[42] J. J. Lynch, H. P. Moyer, J. H. Schaffner, Y. Royter, M. Sokolich, B. Hughes, Y. J. Yoon, and J. N. Schulman, "Passive Millimeter-Wave Imaging Module With Preamplified Zero-Bias Detection," *IEEE Transactions on Microwave Theory and Techniques*, vol. 56, pp. 1592–1600, July 2008.

[43] E. R. Brown, "Fundamentals of Terrestrial Millimeter-Wave and THz Remote Sensing," *International Journal of High Speed Electronics and Systems*, vol. 13, no. 04, pp. 995–1097, 2003.

[44] R. H. Dicke, "The measurement of thermal radiation frequencies," *Revieww of Scientific Instruments*, vol. 17, pp. 268–275, 1946.

[45] F. Thomsen, "On the Resolution of Dicke-Type Radiometers," *IEEE Transactions on Microwave Theory and Techniques*, vol. 32, pp. 145–150, Feb 1984.

[46] N. Skou and D. Vine, *Microwave Radiometer Systems: Design and Analysis*. Artech House remote sensing library, Artech House, 2006.

[47] K. Fujimoto, "On the Correlation Radiometer Technique," *IEEE Transactions on Microwave Theory and Techniques*, vol. 12, pp. 203–212, Mar 1964.

[48] C. M. Grens, J. D. Cressler, J. M. Andrews, Q. Liang, and A. J. Joseph, "Reliability issues associated with operating voltage constraints in advanced SiGe HBTs," in *2005 IEEE International Reliability Physics Symposium, 2005. Proceedings. 43rd Annual.*, pp. 409–414, April 2005.

[49] L. Zheng, L. Gilreath, V. Jain, and P. Heydari, "Design and analysis of a W-Band detector in 0.18- μm SiGe BiCMOS," in *Silicon Monolithic Integrated Circuits in RF Systems (SiRF), 2010 Topical Meeting on*, pp. 196–199, Jan 2010.

[50] J. W. May and G. M. Rebeiz, "High-performance W-band SiGe RFICs for passive millimeter-wave imaging," in *2009 IEEE Radio Frequency Integrated Circuits Symposium*, pp. 437–440, June 2009.

[51] R. L. Schmid, P. Song, C. T. Coen, A. . Ulusoy, and J. D. Cressler, "On the Analysis and Design of Low-Loss Single-Pole Double-Throw W-Band Switches Utilizing Saturated SiGe HBTs," *IEEE Transactions on Microwave Theory and Techniques*, vol. 62, pp. 2755–2767, Nov 2014.

[52] T. S. D. Cheung and J. R. Long, "Shielded passive devices for silicon-based monolithic microwave and millimeter-wave integrated circuits," *IEEE Journal of Solid-State Circuits*, vol. 41, pp. 1183–1200, May 2006.

[53] R. Jonsson, R. Malmqvist, S. Reyaz, A. Rydberg, and M. Kaynak, "Design and results of W-band power detectors in a 130 nm SiGe BiCMOS process technology," in *European Microwave Integrated Circuit Conference (EuMIC), 2014 9th*, pp. 289–292, Oct 2014.

[54] J. W. May and G. M. Rebeiz, "Design and Characterization of W -Band SiGe RFICs for Passive Millimeter-Wave Imaging," *IEEE Transactions on Microwave Theory and Techniques*, vol. 58, pp. 1420–1430, May 2010.

[55] M. E. Tiuri, "Radio Astronomy Receivers," *IEEE Transactions on Military Electronics*, vol. 8, pp. 264–272, July 1964.

[56] T. Kanar and G. M. Rebeiz, "A Low-Power 136-GHz SiGe Total Power Radiometer With NETD of 0.25 K," *IEEE Transactions on Microwave Theory and Techniques*, vol. 64, pp. 906–914, March 2016.

[57] P. Song, A. . Ulusoy, R. L. Schmid, and J. D. Cressler, "A high gain, W-band SiGe LNA with sub-4.0 dB noise figure," in *2014 IEEE MTT-S International Microwave Symposium (IMS2014)*, pp. 1–3, June 2014.

[58] L. Gilreath, V. Jam, and P. Heydari, "A W-band LNA in 0.18- μm SiGe BiCMOS," in *Proceedings of 2010 IEEE International Symposium on Circuits and Systems*, pp. 753–756, May 2010.

[59] A. Çağrı Ulusoy, R. L. Schmid, M. Kaynak, B. Tillack, and J. D. Cressler, "High-performance W-band LNA and SPDT switch in 0.13 μ;m SiGe HBT technology," in *2015 IEEE Radio and Wireless Symposium (RWS)*, pp. 162–164, Jan 2015.

[60] I. Kallfass, S. Diebold, H. Massler, S. Koch, M. Seelmann-Eggebert, and A. Leuther, "Multiple-Throw Millimeter-Wave FET Switches for Frequencies from 60 up to 120 GHz," in *Microwave Conference, 2008. EuMC 2008. 38th European*, pp. 1453–1456, Oct 2008.

[61] W. T. Khan, A. Çağrı Ulusoy, G. Dufour, M. Kaynak, B. Tillack, J. D. Cressler, and J. Papapolymerou, "A D-Band Micromachined End-Fire Antenna in 130-nm SiGe BiCMOS Technology," *IEEE Transactions on Antennas and Propagation*, vol. 63, pp. 2449–2459, June 2015.

[62] R. Malmqvist, C. Samuelsson, D. Dancila, S. Reyaz, M. Kaynak, and A. Rydberg, "Design and test results of a wideband sige detector and on-chip slot antenna for W-band sensing applications," in *CAS 2012 (International Semiconductor Conference)*, vol. 1, pp. 205–208, Oct 2012.

[63] A. J. Tang, Y. Kim, and Q. J. Gu, "25.4 A 0.43K-noise-equivalent-ΔT 100GHz dicke-free radiometer with 100% time efficiency in 65nm CMOS," in *2016 IEEE International Solid-State Circuits Conference (ISSCC)*, pp. 430–431, Jan 2016.

[64] L. Gilreath, V. Jain, and P. Heydari, "Design and Analysis of a W-Band SiGe Direct-Detection-Based Passive Imaging Receiver," *IEEE Journal of Solid-State Circuits*, vol. 46, pp. 2240–2252, Oct 2011.

[65] A. Tomkins, P. Garcia, and S. P. Voinigescu, "A Passive W-Band Imaging Receiver in 65-nm Bulk CMOS," *IEEE Journal of Solid-State Circuits*, vol. 45, pp. 1981–1991, Oct 2010.

[66] R. B. Yishay, E. Shumaker, and D. Elad, "Key components of a D-band Dicke-radiometer in 90 nm SiGe BiCMOS technology," in *Microwave Integrated Circuits Conference (EuMIC), 2015 10th European*, pp. 176–179, Sept 2015.

[67] E. Dacquay, A. Tomkins, K. H. K. Yau, E. Laskin, P. Chevalier, A. Chantre, B. Sautreuil, and S. P. Voinigescu, " D -Band Total Power Radiometer Performance Optimization in an SiGe HBT Technology," *IEEE Transactions on Microwave Theory and Techniques*, vol. 60, pp. 813–826, March 2012.

[68] A. . Ulusoy, P. Song, W. T. Khan, M. Kaynak, B. Tillack, J. Papapolymerou, and J. D. Cressler, "A SiGe D-Band Low-Noise Amplifier Utilizing Gain-Boosting Technique," *IEEE Microwave and Wireless Components Letters*, vol. 25, pp. 61–63, Jan 2015.

[69] A. . Ulusoy, P. Song, R. L. Schmid, W. T. Khan, M. Kaynak, B. Tillack, J. Papapolymerou, and J. D. Cressler, "A Low-Loss and High Isolation D-Band SPDT Switch Utilizing Deep-Saturated SiGe HBTs," *IEEE Microwave and Wireless Components Letters*, vol. 24, pp. 400–402, June 2014.

[70] W. T. Khan, A. C. Ulusoy, R. Schmid, T. Chi, J. D. Cressler, H. Wang, and J. Papapolymerou, "A D-band (110 to 170 GHz) SPDT switch in 32 nm CMOS SOI," in *2015 IEEE MTT-S International Microwave Symposium*, pp. 1–3, May 2015.

[71] P. W. Cheng, J. He, J. Luo, H. Wang, S. Chang, Q. Huang, D. Hou, Y. Z. Xiong, and Y. P. Zhang, "150-GHz SPDT switch with rat-race coupler topology in 0.13- μm SiGe BiCMOS," in *2015 Asia-Pacific Microwave Conference (APMC)*, vol. 2, pp. 1–3, Dec 2015.

[72] Q. J. Gu, Z. Xu, A. Tang, and M. C. F. Chang, "A D-Band Passive Imager in 65 nm CMOS," *IEEE Microwave and Wireless Components Letters*, vol. 22, pp. 263–265, May 2012.